

Thermal Modeling and Inversion of Borehole Temperature Data

Zur Erlangung des akademischen Grades eines

DOKTORS DER NATURWISSENSCHAFTEN (Dr. rer. nat.)

von der KIT-Fakultät für

Bauingenieur-, Geo- und Umweltwissenschaften
des Karlsruher Instituts für Technologie (KIT) genehmigte

DISSERTATION

von

Jia Wang, M.Sc.

aus China

Tag der mündlichen Prüfung: 14. Dezember, 2021

Referent: Prof. Dr.-Ing. Thomas Kohl

Korreferent: Prof. Dr.-Ing. Ingo Sass

Kalsruhe 2021

Abstract

Among renewable resources, geothermal energy occupies a unique position due to its base-load capability. When mining geothermal energy resources, one of the crucial parameters is the formation temperature, which determines the thermal potential of the geothermal system and the installed capacity of the generated power. To reach high-temperature zones, deep boreholes are drilled using advanced technologies such as the Enhanced Geothermal System. In particular, the high productivity and efficiency of power generation from supercritical geothermal resources have motivated initiatives to drill into ultra-hot magma roof zones in recent years. Since the formation temperature is usually highly disturbed during drilling, it is necessary to interpret the temperature data from boreholes to determine the actual formation temperature at thermal equilibrium, also known as the static formation temperature (SFT). The conventional approach to determining the SFT is to apply corrections to temperature data measured during a sufficient period after drilling is stopped (also called the shut-in phase). However, using such a method can face several challenges in high-enthalpy boreholes, including economic and technical constraints on conducting high-temperature measurements during long thermal recovery periods and safety issues when casings and instruments are exposed to high temperatures. In such a context, it can be necessary to employ other techniques to interpret temperature data measured under a different flow condition, such as injection, to overcome these limitations in data acquisition.

This work addresses the determination of the SFT from high-temperature boreholes by applying numerical modeling and inversion techniques to temperature data obtained under cooling (or sub-critical) conditions. It is motivated by the Iceland Deep Drilling Project, which involves deepening an old production well, RN-15, into a new exploration well called RN-15/IDDP-2. During the drilling, a severe problem that occurred is the high circulation loss at several loss zones. Measured temperature data show that the fluid at the well bottom has reached a super-critical state even when the thermal field is non-equilibrium. Since these data are obtained while cold water is still being injected into the well, the question arises as to whether it is possible to determine the SFT and unknown flow losses from the injection temperature logs. With

this in mind, I first performed simulation studies in this dissertation to improve our understanding of the thermal processes during drilling and logging. I then developed inversion workflows that allow both rigorous quantification of the uncertainties in the estimates and calculation of the posterior probability density function for the SFT estimates.

The first study examines the factors and processes that influence the temperature evolution in the borehole during fluid injection and shut-in periods. Thermal modeling of temperature logs considers various drilling scenarios for high-enthalpy boreholes, such as injection and shut-in conditions in multiple casing strings and the presence of circulation losses. In the early transient stage of the shut-in, the borehole temperature exhibits high sensitivity to the heat transfer rate between the borehole fluid and the solid wall. On the other hand, during fluid injection, the borehole temperature is highly dependent on the flow rate. Such a dependence enables the analysis of temperature log to identify and quantify the downhole flow losses. Finally, the SFT is derived from temperature logs by applying the Horner plot method. The results highlight two aspects: interpretation of temperature logs recorded during shut-in would require data measured after a long shut-in period; downhole cooling can lead to large errors in the SFT estimation. These aspects make it clear that the application of the Horner-plot type of method to high-enthalpy boreholes can be very challenging.

Subsequently, temperature data measured during standard injections are inverted to determine the SFT. An inverse modeling study incorporating machine learning techniques is conducted to quantify the uncertainty in the interpretation of these logs. The advantage of the applied approach is that it iteratively proposes new sample points located in the most informative model space based on results from the previous simulation runs. Solutions are searched for the model parameters that lead to temperature predictions with the same quality of fit as the actual temperature values. A contour map is then created for straightforward uncertainty quantification. Several aspects are examined for their impact on the accuracy of the SFT prediction, such as injection conditions (i.e., injection rate and duration) prior to the acquisition of temperature measurements, the presence of flow loss zones, the quality of the temperature data, and the constraints applied in the inversion (e.g., misfit function and prior information). The study shows that temperature data measured under higher flow rates or after longer injection times could lead to less reliable results for the SFT prediction. Moreover, efforts should be made to collect high-quality temperature data and, if possible, integrate more information such as the magnitude of flow losses and the variation of the thermal gradient with depth.

In the third study, the SFT is estimated following the Bayesian framework, where the

posterior probability density function can be calculated. To overcome the problem of high computational cost due to a large number of forward evaluations, surrogate models are constructed using artificial neural networks to increase the computational speed at each forward run. The inversion workflow is first tested on synthetic scenarios to verify its validity and examine the effects of measurement noise and the presence of drilling losses on the quality of the estimates. The SFT can be predicted with high accuracy if accurate measurements are used. However, in the presence of flow losses, the uncertainty in SFT estimates would increase, especially at depths below the loss zones. In addition, noise in the data is a strong source of error for SFT determination. For the real example of the high-temperature well in the Reykjanes geothermal field - RN-15/IDDP-2, an injection temperature log is inverted to determine the drilling losses in three loss zones and the SFT. It is found that drilling losses can be well quantified from temperature log for this well. But the SFT estimates at different depths are subjected to great uncertainties due to the lack of prior information on the change in geothermal gradient with depth. Nevertheless, the probable values for the SFT at 4500 m predicted by this study are comparable with the published results of other relevant work.

Kurzfassung

Unter den erneuerbaren Ressourcen nimmt die Geothermie aufgrund ihrer Grundlastfähigkeit eine einzigartige Stellung ein. Bei der Gewinnung von geothermischen Energiequellen ist einer der entscheidenden Parameter die Formationstemperatur, die das thermische Potenzial des geothermischen Systems und die installierte Leistung der erzeugten Energie bestimmt. Um Hochtemperaturzonen zu erreichen, werden Tiefbohrungen mit fortschrittlichen Technologien wie dem Enhanced Geothermal System durchgeführt. Insbesondere die hohe Produktivität und Effizienz der Stromerzeugung aus superkritischen geothermischen Ressourcen haben in den letzten Jahren Initiativen motiviert, in ultraheiße Magmakammern zu bohren. Da die Formationstemperatur während der Bohrung jedoch in der Regel stark gestört wird, müssen die Temperaturdaten aus Bohrlöchern interpretiert werden, um die wahre Formationstemperatur im thermischen Gleichgewicht zu bestimmen, die auch als statische Formationstemperatur (SFT) bezeichnet wird. Der herkömmliche Ansatz zur Bestimmung der SFT besteht darin, Korrekturen an den Temperaturdaten vorzunehmen, die während eines ausreichenden Zeitraums nach Beendigung der Bohrung (auch Shut-in genannt) gemessen wurden. Die Anwendung einer solchen Methode kann jedoch in Hochenthalpie-Bohrlöchern auf mehrere Herausforderungen stoßen, einschließlich wirtschaftlicher und technischer Beschränkungen bei der Durchführung von Hochtemperaturmessungen während langer thermischer Erholungsphasen und Sicherheitsfragen, wenn Verrohrung und Instrumente hohen Temperaturen ausgesetzt sind. In einem solchen Zusammenhang kann es notwendig sein, andere Techniken zur Interpretation von Temperaturdaten zu verwenden, die unter einer anderen Strömungsbedingung, wie z.B. der Injektion, gemessen wurden, um diese Einschränkungen bei der Datenerfassung zu überwinden.

Diese Arbeit befasst sich mit der Bestimmung der SFT von Hochtemperaturbohrungen durch Anwendung numerischer Modellierungs- und Inversionstechniken auf Temperaturdaten, die unter Kühlbedingungen (oder unterkritischen Bedingungen) gewonnen wurden. Hintergrund ist das Island Deep Drilling Project, bei dem eine alte Produktionsbohrung (RN-15) zu einer neuen Explorationsbohrung (RN-15/IDDP-2)

vertieft wird. Während der Bohrung trat ein ernstes Problem auf: der hohe Zirkulationsverlust in mehreren Verlustzonen. Die Messdaten zeigen, dass die Flüssigkeit am Boden des Bohrlochs einen überkritischen Zustand erreicht hat, auch wenn sich das thermische Feld nicht im Gleichgewicht befindet. Da diese Daten gemessen werden, während noch kaltes Wasser in das Bohrloch injiziert wird, stellt sich die Frage, ob es möglich ist, die SFT und unbekannte Strömungsverluste aus den Temperaturlogs der Injektion zu bestimmen. Vor diesem Hintergrund habe ich in dieser Dissertation zunächst Simulationsstudien durchgeführt, um unser Verständnis der thermischen Prozesse beim Bohren und Loggen zu verbessern. Anschließend habe ich Inversionsarbeitsabläufe entwickelt, die sowohl eine strenge Quantifizierung der Unsicherheiten in den Schätzungen als auch die Berechnung der posterioren Wahrscheinlichkeitsdichtefunktion für die SFT-Schätzungen ermöglichen.

In der ersten Studie werden zunächst die Faktoren und Prozesse untersucht, die die Temperaturentwicklung im Bohrloch während der Injektions- und Shut-in-Perioden beeinflussen. Bei der thermischen Modellierung von Temperaturlogs werden verschiedene Bohrszenarien für Bohrungen mit hoher Enthalpie berücksichtigt, z.B. Injektions- und Shut-in-Bedingungen in mehreren Verrohrungssträngen und das Vorhandensein von Strömungsverlusten. In der frühen Übergangsphase des Shut-in ist die Bohrlochtemperatur sehr empfindlich gegenüber der Wärmeübertragungsrate zwischen der Bohrlochflüssigkeit und der festen Wand. Insbesondere wird die Rolle der freien Konvektion hervorgehoben, indem gezeigt wird, dass die richtige Parametrisierung der Wärmeübertragungsrate durch freie Konvektion den Wert der vorhergesagten Bohrlochtemperatur erheblich beeinflusst. Andererseits ist die Bohrlochtemperatur bei der Flüssigkeitsinjektion stark von der Durchflussrate abhängig. Diese Abhängigkeit ermöglicht die Verwendung eines Injektions-Temperaturprotokolls zur Identifizierung und Quantifizierung von Strömungsverlusten im Bohrloch. Schließlich wird die SFT aus den Temperaturlogs mit Hilfe der Horner-Plot-Methode abgeleitet. Die Ergebnisse weisen auf zwei Probleme hin: die Interpretation von Temperaturlogs, die während des Shut-in aufgezeichnet wurden, würde Daten erfordern, die nach einer langen Shut-in-Periode gemessen wurden; die Kühlung des Bohrlochs kann große Fehler bei der Schätzung der SFT verursachen. Diese Aspekte machen deutlich, dass die Anwendung der Horner-Plot-Methode in Hochtemperaturbohrlöchern sehr schwierig sein kann.

Anschließend werden die während der Standardinjektionen gemessenen Temperaturdaten invertiert, um die SFT zu bestimmen. Eine Studie zur inversen Modellierung mit Techniken des maschinellen Lernens wird durchgeführt, um die Unsicherheit bei der Interpretation dieser Temperaturlogs zu quantifizieren. Der Vorteil des angewandten

Ansatzes besteht darin, dass er auf der Grundlage der Ergebnisse der vorangegangenen Simulationsläufe iterativ neue Stichprobenpunkte vorschlägt, die sich im informativsten Modellraum befinden. Es werden Lösungen für die Modellparameter gesucht, die zu Temperaturvorhersagen mit der gleichen Anpassungsqualität führen wie die tatsächlichen Temperaturwerte. Auf diese Weise wird eine Konturenkarte zur einfachen Quantifizierung der Unsicherheit erstellt. Es werden mehrere Aspekte auf ihre Auswirkungen auf die Genauigkeit der SFT-Vorhersage untersucht, wie z.B. die Injektionsbedingungen (d.h. Injektionsrate und -dauer) vor der Erfassung der Temperaturmessungen, das Vorhandensein von Strömungsverlustzonen, die Qualität der Temperaturdaten und die bei der Inversion angewandten Einschränkungen (z.B. Misfit-Funktion und vorherige Informationen). Die Studie zeigt, dass Temperaturdaten, die bei höheren Flussraten oder nach längeren Injektionszeiten gemessen werden, zu weniger zuverlässigen Ergebnissen für die SFT-Vorhersage führen könnten. Darüber hinaus sollten Anstrengungen unternommen werden, um qualitativ hochwertige Temperaturdaten zu sammeln und, wenn möglich, andere Informationen wie die Größe der Strömungsverluste und die Variation des thermischen Gradienten mit der Tiefe zu integrieren.

In der dritten Studie wird die SFT mit Hilfe des Bayes'schen Ansatzes geschätzt, wobei die posteriore Wahrscheinlichkeitsdichtefunktion berechnet werden kann. Um das Problem der hohen Rechenkosten aufgrund der großen Anzahl von Vorwärtsauswertungen zu überwinden, werden Ersatzmodelle unter Verwendung künstlicher neuronaler Netze erstellt, um die Rechengeschwindigkeit bei jedem Vorwärtslauf zu erhöhen. Der Arbeitsablauf der Inversion wird zunächst an synthetischen Szenarien getestet, um seine Gültigkeit zu überprüfen und die Auswirkungen von Messrauschen und Strömungsverlusten auf die Qualität der Schätzungen zu untersuchen. Die SFT kann mit hoher Genauigkeit vorhergesagt werden, wenn genaue Messungen vorgenommen werden. Bei Vorhandensein von Strömungsverlusten würde die Unsicherheit der SFT-Schätzungen jedoch zunehmen, insbesondere in Tiefen unterhalb der Verlustzone. Darüber hinaus ist das Rauschen in den Daten eine starke Fehlerquelle bei der Bestimmung der SFT. Für das reale Beispiel der Hochtemperaturbohrung im geothermischen Feld von Reykjanes - RN-15/IDDP-2 - wird ein Injektionstemperaturlog invertiert, um die Strömungsverluste in drei Verlustzonen und die SFT zu bestimmen. Es zeigt sich, dass die Bohrverluste mit Hilfe von Temperaturmessungen für dieses Bohrloch gut quantifiziert werden können. Allerdings sind die SFT-Schätzungen in der Tiefe mit großen Unsicherheiten behaftet, da es keine vorherigen Informationen über die Veränderung des geothermischen Gradienten in der Tiefe gibt. Dennoch sind die in dieser Studie vorhergesagten wahrscheinlichen Werte der SFT auf 4500 m mit den veröffentlichten Ergebnissen anderer einschlägiger Studien vergleichbar.

Acknowledgements

First, I would like to express my great gratitude to my supervisor Prof. Thomas Kohl for providing me the opportunity to conduct this research in his group. Thanks for your support and constructive suggestions during the planning and development of this research work.

Thanks you also Prof. Ingo Sass for agreeing to be the co-supervisor of my thesis.

My gratitude goes out to all my coworkers! Special thanks to Fabian Nitschke for always backing me up throughout my PhD time! You has been a great help to me with all your advise, generous patience and encouragement! I thank Emmanuel Gaucher for all the spirit-lifting conversations and suggestions! I will always remember your optimistic and energetic nature . I am very grateful for the time you have spent with me for the scientific discussions, for hanging in there joining the weekly meeting with me and Fabian. I also thank Maziar Gholami Korzani for setting up and introducing me to the Moose-based simulation platform. Many thanks to Silke Schlichting for helping me with all the administrative processes at KIT during my stay. Thanks to all my colleagues for letting me show up at their doors anytime when I need help!

I would also like to thank Prof. Rainer Helmig, Prof. Holger Class, Timo Koch and Beatrix Becker from the University of Stuttgart for first introducing me into the world of numerical simulation back in my master's study.

At last but not the least, I thank my parents and my sister for their love and support throughout my life's journey. I thank my husband, Ran, for his accompany, for cheering me up and supporting me solving the daily hassles.

This project has received funding from the European Union's HORIZON 2020 research and innovation program under Grant Agreement No. 690771. The last four months of my study was funded by KHYS, Karlsruhe Institute of Technology.

Contents

1	Introduction	1
1.1	Deep and high-enthalpy geothermal energy	1
1.2	Motivation: the drilling of the RN-15/IDDP-2 well aimed for super-critical geothermal resources	5
1.3	Access and evaluation of formation temperature using temperature data	7
1.3.1	Data acquisition	8
1.3.2	Uncertainties in the data	9
1.3.3	Data interpretation	10
1.4	Thesis overview	11
2	Fundamentals of heat transfer in the borehole and formation	14
2.1	Heat transfer in the formation	14
2.1.1	Physical processes	15
2.1.2	Conservation governing equations	19
2.1.3	Analytical solutions for classical thermal problems	19
2.1.4	Impact factors on the temperature distribution in the subsurface	22
2.2	Heat transfer in the wellbore	26
2.2.1	Physical processes	26
2.2.2	Analytical solutions for borehole temperature distribution .	29
2.3	Static formation temperature estimation using borehole temperature data	35
2.3.1	The line-source model	36
2.3.2	The spherical-radial heat-flow model	37
2.3.3	The cylindrical heat-source method	38
3	Temperature log simulations in high-enthalpy boreholes	40
3.1	Introduction	41
3.2	Methodology	43
3.2.1	Analytical approach	43
3.2.2	Numerical Approach	44
3.2.3	Heat transfer coefficients	48

3.3	Simulation Scenarios	50
3.3.1	Shut-in temperature logs simulation	50
3.3.2	High-temperature environment simulation	52
3.4	Results and Discussion	54
3.4.1	Estimating SFT using shut-in temperature logs	54
3.4.2	Estimating the SFT using temperature logs obtained under borehole cooling	56
3.4.3	Characterization of the fluid loss in the well	58
3.5	Conclusion	61
4	Uncertainty analysis of numerical inversions of temperature logs from boreholes under injection conditions	64
4.1	Introduction	65
4.2	Methodology	67
4.2.1	Forward thermal modeling	68
4.2.2	Adaptive sampling based on the reduced order model	69
4.3	Synthetic case studies	71
4.3.1	Uniform geothermal gradient	71
4.3.1.1	Estimation of SFT alone	72
4.3.1.2	Estimation of SFT and flow loss	75
4.3.2	Two-layer geothermal gradient	77
4.4	Discussion	80
4.4.1	Impact of the injection and logging conditions	80
4.4.2	Impact of a flow loss zone	81
4.4.3	Impact of inversion constraints	83
4.4.3.1	The misfit function	83
4.4.3.2	Prior information for the model space	83
4.5	Conclusion	86
5	Surrogate-based inversion of borehole logs for formation temperature determination	89
5.1	Introduction	90
5.2	Method	93
5.2.1	The artificial neural network	93
5.2.2	MCMC method	95
5.3	Analysis of synthetic scenarios	97
5.3.1	Surrogate models	99
5.3.2	Inversions of temperature logs	100
5.4	Application to the temperature log from the RN-15/IDDP-2 well	103

5.4.1	The RN-15/IDDP-2 well	103
5.4.2	Estimation of the SFT below 2.5 km and fluid losses	105
5.4.2.1	Surrogate models	106
5.4.2.2	Results of the SFT and flow loss estimates	108
5.5	Discussion and Conclusion	112
5.6	Acknowledgments	114
5.7	Author contributions statement	114
6	Conclusions and future work	116
6.1	Major findings of the research	117
6.2	Future work	120
Appendix A Marginal PPDFs of the SFT and flow losses for the RN-15/IDDP-2 well		122
Appendix B Simulation of temperature log for the RN-15/IDDP-2 well		125
B.1	Introduction	126
B.2	Drilling and temperature logging data of the RN-15/IDDP-2 well	127
B.3	Sensitivity analysis of the key factors	127
B.3.1	Impact of the flow averaging scheme	127
B.3.2	Impact of the deepening of the well	129
B.3.3	Impact of the movement of the logging tool	131
B.4	Calibration of the effective thermal conductivity of the formation	133
B.5	Summary	134

List of Figures

1.1	Principle of hydrothermal and enhanced geothermal system (EGS). For the EGS (left), cold water is injected through injection well into an artificially created fracture network. The heated water is extracted by a production well and fed to the binary power plant system on the surface to produce electrical power. Later, the cooled water is re-injected into the reservoir and the loop begins. In the hydrothermal system (right), thermal water is produced from a natural aquifer and injected back into the aquifer.	3
2.1	Formation temperature profile for four different cases: (1) heat conduction (black line), (2) heat conduction with radiogenic heat production (green line), (3) heat conduction in formation with varying thermal conductivity (blue line), and (4) heat convection (red line). .	22
2.2	Schematic illustration of forced convective flow due to a hydraulic gradient (left) and free convective flow due to a temperature gradient (right) in boreholes (p: pressure, T: Temperature). After Berthold (2010).	27
2.3	Comparison of analytical and simulated solution of Ramey's heat transmission model: case (1) and case (2) are the injection scenarios, where injection temperatures at well-head are 20 °C and 90 °C, respectively; case (3) is the production scenario: fluid is produced from bottom-hole at 245 °C reservoir temperature. The analytical solution was plotted in lines: solid lines (one day), dash-dot lines (5 days), and dot lines (20 days). The simulated solution was marked in symbols: green crosses (one day), red circle (5 days), diamonds with lower half black (20 days). Wang et al. (2019).	31

- 2.4 Comparison of analytical solution and simulated solution for the counterflow heat exchange model. The black color represents the temperature of the fluid inside the drill pipe, and the red color represents the temperature of the annulus fluid. Solutions were calculated and compared at three different circulation times: 5 days, 10 days, 20 days. The analytical solution was plotted in lines: solid lines (5 days), dash-dot lines (10 days), and dot lines (20 days). The simulated solution was marked in symbols: circles (5 days), squares (10 days), crosses (20 days) Wang et al. (2019). 35
- 3.1 Schematic of the heat exchange model between the wellbore and the formation. Governing equations are solved in four regions: the fluid inside the drill pipe (Region 1), the drill pipe wall (Region 2), the annulus (Region 3), casing-cement-formation (Region 4). The solid arrow pointing downwards and the dashed arrow pointing upwards in the annulus refer to coflow and counterflow scenarios in the wellbore, respectively. 45
- 3.2 Two different SFT profiles assumed in the high-temperature environment simulations: linear SFT describes a pure heat conduction geothermal system, S-shaped SFT reflects typically occurring convection zones in the geothermal system. 52
- 3.3 (a) The change of BHT within a shut-in period of 20 days under four different heat transfer coefficients (h) in the borehole. (b) The Horner-plots of the four temperature curves shown in (a) (the x-axis value is the opposite of the Horner dimensionless time (Equation 3.1), the minimum x-axis value of the temperature data on the curves corresponds to when $t_s = 1$ hr, the maximum x-axis value corresponds to when $t_s = 140$ days). 55
- 3.4 The HM plots (lines) using BHT measurements (markers) at (a) early shut-in time ($t_s = 12, 18$ and 24 hours) and (b) long-term shut-in ($t_s =$ two, three, and four days) for each of the four different heat transfer coefficients (h) considered. (c) Comparison of the results of SFT estimation with the true SFT value: the black bars are the four SFT estimates using early shut-in time BHT data; the dark grey bars represent the four SFT estimates using long-term shut-in BHT data; the solid line stands for the referencing value which is the true SFT (257 °C). 56

3.5	Estimated SFT profile under different flow rates (Q) in the annulus during the 2 nd period versus depth when assuming (a) a linear SFT profile and (b) S-shaped SFT profile (black dots represent the true SFTs, red lines represent the SFT estimates under real shut-in conditions). (c) Errors in SFT estimates for the linear-shaped SFT profile case. (d) Errors in SFT estimates for the S-shaped SFT profile case.	58
3.6	The generated temperature logs for the S-shaped SFT profile case considering different percentages of fluid loss at a depth of 3.35 km. (a) Results for the injection flow rate of 5 L/s. (b) Results for the injection flow rate of 50 L/s.	60
3.7	The ratio of temperature gradient below the fluid loss zone (3.35 km depth) to the gradient above the fluid loss zone versus the percentage of fluid loss (S-shaped SFT profile is assumed).	61
4.1	(a) Schematic of the simulation set-up with the boundary and initial conditions. Injection temperature at the well-head is 10 °C, SFT is a linear function of vertical depth and is applied as the initial condition and the Dirichlet boundary condition at the right edge of the formation. (b) Synthetic temperature logs after different injection durations (3, 6, 9 and 12 hours) at an rate of 50 L/s. (b) Synthetic temperature logs obtained under different flow rates (25, 50, 75, and 100 L/s) after 6 hours of injection.	74
4.2	Comparisons of the maximum and minimum values of the estimated SFT at the bottom-hole (4500 m depth) considering: (a) different injection durations (3, 6, 9 and 12 hours), flow rate of 50 L/s and $RSME_{thres}=1.0$ °C; (b) different flow rates (25, 50, 75 and 100 L/s), injection duration of 6 hours and $RSME_{thre} = 1.0$ °C; (c) different $RSME_{thre}$ values (0.5, 1.0, 1.5, and 2.0 °C), injection duration of 6 hours and flow rate = 50 L/s.	75
4.3	Synthetic temperature logs of the borehole fluid after different injection durations (3, 6 and 12 hours) considering a flow rate of 50 L/s above 3500 m and 25 L/s below 3500 m due to the loss.	76
4.4	Contour plot of the $RMSE$ as a function of the two estimated variables: SFT at bottom-hole depth (horizontal axis) and the flow rates below 3500 m (vertical axis). The black star marks the true values for bottom-hole SFT and flow rate below 3500 m (which corresponds to an $RMSE$ value of 0.0 °C).	77

- 4.5 Predefined SFT profile of formation F1 (black line), borehole temperature profile (blue line) calculated after 6 hours injection at 50 L/s and the derivative of temperature with respect to depth (red dashed line). 78
- 4.6 Contour plot of the $RMSE_{thres} = 1.0$ °C in the exploration space of SFT value at the bottom hole and the flow rate below 3500 m for model F1A1 and F1A2. The blue star marks the true values for the SFT and the flow rate (500 °C, 25 L/s). 79
- 4.7 Maximum (circles) and minimum (squares) values of the estimated SFT at the bottom-hole using temperature logs obtained under injection rate 25 L/s (blue line) and 50 L/s (red line) after different injection durations (1, 2, 3, 4, 6, 9 and 12 hrs) considering $RMSE_{thres} = 1.0$ °C (for the described model in Chapter 4.3.1.1). 81
- 4.8 Left: borehole temperature logs (L1,L2) that both satisfy $RMSE$ equals 1.0 °C in model F1A1, but are simulated with different values of SFT at the bottom-hole and flow rate below 3500 m. L1 (filled circles) is simulated with a bottom-hole SFT value of 298 °C and a flow rate of 16.9 L/s below 3500 m, and L2 (filled triangles) with a bottom-hole SFT value of 737.4 °C and a flow rate of 34.5 L/s below 3500 m. Right: temperature differences of L1 (hollow circles) and L2 (hollow triangles) with respect to the synthetic temperature log. 82
- 4.9 Contour lines in the parameter space (bottom-hole SFT and the flow rate below 3500 m) where the following criteria for model F1A1 are satisfied: (1) $RMSE_{thres} = 1.0$ °C (F1A1-M1, black line); (2) the maximum absolute difference between the simulated and the logged temperature for each measurement is 1.0 °C (F1A1-M2, red line). The blue star marks the true values for the SFT (500 °C) and the flow rate (25 L/s). 84
- 4.10 The true SFT profiles of formation F1 (black) and F2 (red). 85
- 4.11 Contour lines for $RMSE$ equals 1.0 °C for model F1 (black) and F2 (red) in the model space of SFT at the bottom-hole and the flow rate below 3500 m, when both assuming a constant geothermal gradient for the investigated depth interval between 2500 and 4500 m. The blue star marks the true values for the SFT (500 °C) and the flow rate (25 L/s). 85

5.1	A three-layer feed-forward Multilayer Perceptron (MLP) model. I number input neurons are feed into the network. The two hidden layers which contain J and K number of neurons, respectively, perform nonlinear transformations of the inputs (i.e., by multiplying their associated weights, w) to the N number of outputs.	95
5.2	(a) Schematic of the simulation set-up with the boundary and initial conditions. Depends on the scenario, a flow loss of 20% may occur at 3500 m. (b) The SFT profile when assuming the five layers have the same thermal gradient. (c) Synthetic temperature logs for different scenarios: no flow loss occurs and the temperature log is measured with no error (reference, solid line), no flow loss occurs and temperature measurements have random error of $\sim N(0, 1)$ °C (case 1, black dot line), 20% flow is lost into the formation and the temperature log is measured with no error (case 2, red dash line).	98
5.3	Sensitivity of the maximum approximation error ($RMSE_{max}$) in the test set to the training sample size for model S1 and S2.	100
5.4	Marginal PPDF for the SFT (sft1–sft5) at the base of each layer in the reference case. The true value and the 95% confidence interval are marked with the black and green dash line, respectively.	101
5.5	Case 1: marginal PPDF for the SFT at the base of each layer.	102
5.6	Case 2: marginal PPDF for the SFT at the base of each layer and the remaining flow rate after the loss zone at 3500 m.	103
5.7	(a) The SFT profile in the upper 2500 m around the RN-15 (red line); and temperature log of RN-15/IDDP-2 measured on January 3 rd , 2017 (black line) with circulation loss zones indicated. (b) The flow history at the well-head from the start of drilling to the end of the temperature logging. The upper zoom plot shows the flow history on the day of the logging. (c) The change of the temperature measuring depth with time (0 equals when the logging starts) during the downward trip of logging device.	104
5.8	200 prior realizations of borehole temperature profiles and the observation temperature log (\log_{obs} , red line). The profiles are shown in different colors corresponding to four different ranges of the relative flow loss at the first loss zone (3400 m): > 90%, 80-90%, 70-80%, < 70%.	107
5.9	Sensitivity of the maximum approximation error ($RMSE_{max}$) in the test set to the training sample size for model M1 and M2.	108

5.10	The best-fit temperature log predicted by the surrogate model M1 based on the single-layer assumption ((a), blue line) and the surrogate model M2 based on the five-layer assumption ((b), green line). The black dots and the arrows in (a) and (b) represent the measured temperatures and the location of three circulation loss zones, respectively.	109
5.11	Prediction results of the two models: the optimal SFT profile (single-layer model: black dash line; five-layer model: red dash line); 95% confidence interval of SFT (single-layer model: blue shaded; five-layer model: green shaded); 95% confidence interval of the accumulated flow loss ratio (%) at 3400 m, 4200 m and 4375 m with the optimal estimate marked using a vertical tick (single-layer model: magenta horizontal line; five-layer model: green horizontal line. For better readability, the lines are shifted vertically away from the exact depths (marked with black stars) of the loss zones.	111
A.1	Marginal PPDFs of the estimation parameters (SFT at the 4500 m and the three accumulated flow losses, ALS1-ALS3) for the single-layer model. The blue dash lines mark the 95% confidence interval of each parameter.	123
A.2	Marginal PPDFs of SFT at the base of each layer (sft1-sft5) and the three accumulated flow losses (ALS1-ALS3) for the five-layer model.	124
B.1	Three different flow-time functions applied at the wellhead over 145 days. FL1: The average flow over a period of 145 days. FL2: Daily average flow rates. FL3: Daily average flow rates, except that flow rate is averaged every ten minutes for the four weeks prior to logging.	128
B.2	(a) Temperature logs simulated with the three different flow average scheme FL1–FL3. (b) Temperature difference along depth between the logs simulated with FL1 and FL3 (blue), and the logs simulated with FL2 and FL3 (red).	129
B.3	(a) Drilling schedule. (b) Upper panel: Change in well temperature at 3400 m, 4200 m and 4375 m as a function of drilling time. Lower panel: Variation of injection flow rate at the wellhead with time. . .	130
B.4	Simulated temperature logs when assuming a pre-existed well before the injection (red cross) and when considering the drilling schedule (black dashed line), and the difference between the two logs (blue solid line).	131
B.5	(a) Flow rate variation with time during logging. (b) Change in the depth location of the logging tool with time.	132

B.6	(a) Snapshots of the temperature profile along the borehole at the beginning ($temp_t_{begin}$) and end of logging as well as the measured profile ($temp_t_{end}$). (b) Difference between the log and the temperature profile of the borehole at the beginning of the logging (green line) and between the profile of the log and the temperature profile of the borehole at the end of the logging (red line).	132
B.7	The measured temperature log (black circles) and calibrated temperature logs for the upper 2500 m (blue dash line).	134

List of Tables

2.1	Geometric parameters and material properties used in the simulation of the counterflow heat exchange model.	34
3.1	Boundary and initial conditions of the thermal-hydraulic models. . .	47
3.2	Geometry and material properties used in the modeling of circulation and shut-in.	51
3.3	Geometrical extensions of the wellbore.	53
4.1	Parameters for the modeling space, the KNN model and convergence criteria used for the inversion models in this study.	73
5.1	Geometry and completion of the RN-15/IDDP-2 well (referenced to the ground surface)	105
5.2	Summary of the mean, 95% confidence range as well as the optimal estimation of each parameter in the single-layer and five-layer model.	112
B.1	Material properties of the casing, cementing program and the formation	133

Nomenclature

Acronyms

Symbol	Description
SFT	Static formation temperature
DTS	Fiber-optic distributed temperature sensing
BHT	Bottom-hole temperature

Dimensionless Numbers

Symbol	Description	Definition
Ra	Rayleigh number	Eq 2.18
Re	Reynolds number	$\frac{\rho v d}{\mu}$
Pr	Prandtl number	$\frac{\mu c_p}{\lambda}$
Nu	Nusselt number	Eq 3.9-3.12

Greek Symbols

Symbol	Description	Units
λ	Thermal conductivity	$\text{W m}^{-1} \text{K}^{-1}$
μ	Dynamic viscosity	Pas
ρ	Density	kg m^{-3}
ϕ	Porosity of rock	-
β	Volumetric thermal expansion coefficient	K^{-1}

σ	Stefan-Boltzmann constant	$\text{W m}^{-2} \text{K}^{-4}$
	Standard measurement error	K or $^{\circ}\text{C}$
ε	Emissivity	-
	Temperature measurement error	K
α	Geothermal gradient	$^{\circ}\text{C m}^{-1}$
Γ	Interfacial area between fluid and solid structures	m^2
ν	Kinematic viscosity	$\text{m}^2 \text{s}^{-1}$
κ	Thermal diffusivity	$\text{m}^2 \text{s}^{-1}$
θ	Thermal model parameters	-

Other Symbols

Symbol	Description
ALS	Accumulated flow loss
EP	Geothermal energy potential

Roman Symbols

Symbol	Description	Units
\dot{m}	Mass flow rate	kg s^{-1}
c_p	Specific heat capacity	$\text{J kg}^{-1} \text{K}^{-1}$
R	Radiogenic heat production	$\mu\text{W m}^{-3}$
H	Thickness or height	m
h	Heat transfer coefficient	$\text{W m}^{-2} \text{K}^{-1}$
r	Radius	m
	Acceptance rate	-

z	Depth	m
U	Over-all heat transfer coefficient	m
T_D, t_D	Dimensionless temperature and time	-
F	Time function for transient heat transfer	-
A	Cross-sectional area	m^2
d	Hydraulic diameter	m
L	Length of tube	m
C	Constant, Eq 3.14	-
	Label predicted by K-Nearest Neighbor, Eq 4.5	-
W	Thermal model	-
w	Weight	-
a	Constant, Eq 2.2	mKW^{-1}
b	Constant, Eq 2.2	mW^{-1}
	Bias	-
t, t_s, t_c	Time, shut-in time, fluid circulation time	s
h	Enthalpy	$kJkg^{-1}$
u	Random number	-
T	Temperature	K
q	Heat flux	Wm^{-2}
v	Fluid velocity	ms^{-1}
K	Rock permeability	m^2
P	Pressure	Pa

g Gravitational acceleration m s^{-2}

Superscripts

Symbol	Description
c, cond	Heat conduction
conv	Heat convection
f	Fluid
s	Solid
m	Averaged properties of fluid and solid matrix
ra	Radiation
t_o	Outer tubing
c_i	Inner casing
bh	Bottom-hole
in	Injection
p	Production
A,D,C	Annulus, drill pipe, casing
ls	Line source model
sr	Spherical-radial heat-flow model
chs	Cylindrical heat-source model
hm	Horner-plot method
cl	Circulation
sh	Shut-in
wb	Wellbore

w	Tubing wall
abs	Absolute temperature
free	Free convection
cr	Critical thermal gradient
thres	Threshold value
sim	Simulated value
measure	Measured value
obs	Observation
pr	Previous sample

Chapter 1

Introduction

The global energy consumption has increased nearly every year for more than half a century, with an averaging growth rate at around 1% to 2% (Vaclav 2017). The existing energy supply and demand situation is such that very soon all the energy from available sources would need to be harnessed. Continuation of the use of conventional resources is set to face multiple challenges such as depletion of fossil fuel reserves, continued and substantial price rise for oil and gas, global warming and other environmental concerns, etc. Therefore, there is a compelling demand for transitions toward renewable energy resources. Among these green energies, geothermal has its special position due to its availability everywhere and at any time of the day and thus also its significant potential to provide base-load electric power. The theoretical calculation indicates that the energy reserves in the upper 10 km of the earth's crust are approximately 1.3×10^{27} J (Lund et al. 2008). Such an amount of energy can support a global assumption for about 217 million years, considering the average annual energy consumption rate of 6.0×10^{20} J in the past ten years (Looney 2020).

1.1 Deep and high-enthalpy geothermal energy

The utilization of geothermal energy covers a wide range of applications at various temperature and depth levels or based on different technologies to extract geothermal heat. For example, a notional criteria at reservoir depth of 400 m and temperature of 20 °C has been used to differentiate between shallow and deep geothermal energy systems (Breede et al. 2015). The shallow geothermal systems, which are not in the scope of this dissertation, extract energy from the uppermost layer of the earth's crust and usually require energy conversion with e.g. heat pumps. On the other hand,

deep geothermal systems exploit energy by means of deep boreholes. The harvested thermal energy can be used directly and does not require further conversion (Stober and Bucher 2013). Based on the method of exploration, deep geothermal systems are commonly categorized into two types: the hydrothermal geothermal system and the enhanced geothermal system (EGS) (Figure 1.1). A hydrothermal system uses existing aquifers to directly produce hot geothermal fluid stored in the pore space of rocks. Three components are considered indispensable, namely, adequate water storage and permeability, and sufficiently high temperature, so the implementation of such systems is somewhat limited by their locations and ultimate potential. In contrast, an EGS extracts heat from deep rock formation by circulating fluids such as water, brine or CO₂ across fractures and permeable hot rocks between injection and production boreholes (Tomac and Sauter 2018). EGSs do not require a reservoir with high permeability and high-yield aquifers and can access more abundant heat by creating artificial fractures in the hot rocks in areas without adequate hydrothermal resources (Lu 2018). Therefore, in theory, they can be developed anywhere by drilling deep enough into high-temperature reservoirs. Driven by the goal of mining more energy, EGS technology continues to progress at deeper levels, providing the ability to extract heat stored in deep underground at 2–5 km depths with temperatures between 150 °C and 400 °C. Given the enormous energy potential, EGS is considered the most important future use of geothermal resources (Kubik 2006).

Based on different forms of utilization (e.g., heating and electricity), deep geothermal energy is also distinguished between high-enthalpy and low-enthalpy systems. Here, the enthalpy (unit: Joule J) is a thermodynamic quantity that reflects the heat content of the liquid. Although the distinction between these two systems varies among different authors, it is generally accepted that reservoirs are able to provide high enthalpy fluids with temperatures above 150–225 °C (Lee 1996). At such high temperatures, these systems are usually primarily considered for producing electrical power. The presence of these fields is typically linked to tectonic and volcanic activities at plate boundaries. Some high enthalpy regions are also related to hydrothermal convection associated with magma chambers and igneous intrusions that act as deep heat sources (Arnórsson 1995; White 1957). There, aqueous fluids present can develop convective flow because of the strong density contrast caused by a very high temperature gradient. If they are sufficiently hot, these rising hydrothermal fluids will depressurize at a depth where the fluid pressure equals the vapor saturation pressure and start to boil. Studies have shown that permeability of the host rock above the intrusion has a primary control on the temperature distribution and extent of boiling zones (Cathles 1977; Scott et al. 2016; Andersen and Weis 2020). According to a numerical study of Scott et al. (2016), high permeability of the host rock (larger than 10^{-14} m²) allows a higher rate of

heat transfer from the intrusion to geothermal fluids but also leads to moderate fluid temperatures and enthalpies with boiling zones confined to a shallow depth (less than 1 km). Moderate permeability (about 10^{-15} m^2) reduces the overall heat transfer but results in systems with higher fluid temperatures and enthalpies, where boiling zones may extend vertically from the ground surface to the intrusion.

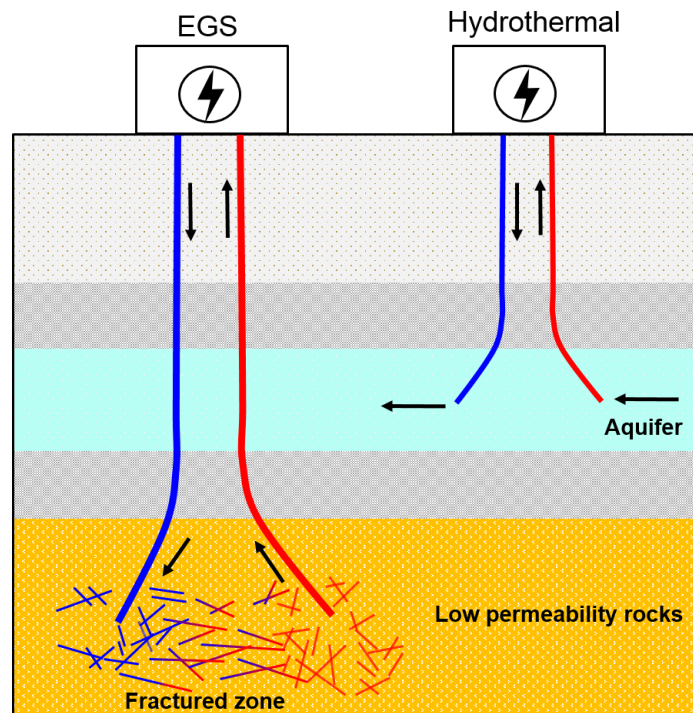


Figure 1.1: Principle of hydrothermal and enhanced geothermal system (EGS). For the EGS (left), cold water is injected through injection well into an artificially created fracture network. The heated water is extracted by a production well and fed to the binary power plant system on the surface to produce electrical power. Later, the cooled water is re-injected into the reservoir and the loop begins. In the hydrothermal system (right), thermal water is produced from a natural aquifer and injected back into the aquifer.

The yield of geothermal power from high-enthalpy geothermal fields is strongly linked to the liquid-vapor transition of water. It is common that high-enthalpy systems produce electricity directly from dry steam or liquid-dominant flash steam (Chamorro et al. 2012). Due to the high temperatures at great depths in magmatic environments, the fluids can also exist under supercritical conditions (i.e., $374 \text{ }^\circ\text{C}$ and 221 bars for pure water, and $405 \text{ }^\circ\text{C}$ and 302 bars for seawater). Producing supercritical fluids can both improve the productivity and efficiency of power generation. According to Fridleifsson and Elders (2005), the electrical power produced by a conventional dry-steam well with a downhole temperature of $235 \text{ }^\circ\text{C}$, pressure of 30 bar, and a flow rate of $0.67 \text{ m}^3 \text{ s}^{-1}$ is around 5 MWe, whereas a supercritical well with a downhole temperature of $430\text{--}550 \text{ }^\circ\text{C}$ and pressure greater than 200 bar could generate around

50 MWe with the same flow rate. This is due to, on the one hand, the high specific enthalpy of the supercritical fluid and, on the other hand, the low viscosity of the fluid which significantly improves hydraulic conductivity (i.e., the increased ratio between buoyancy forces to viscous forces) and leads to high mass transfer rates. These positive prospects have motivated attempts to develop supercritical geothermal fields in a number of countries, such as the HADES project in New Zealand (Bignall 2010), DEEPEGS project in Iceland (Fridleifsson et al. 2016), JBBP project in Japan (Asanuma et al. 2012), and DESCramBLE project in Italy (Bertani et al. 2018).

From a physical perspective, the biggest challenge for extracting heat from very deep, hot rocks is the drastically reduced permeability at supercritical conditions that occur near the brittle-ductile transition (BDT) zone, where the higher temperature plastic zone closer to the magma chamber discharges fluids into the overlying cooler brittle rock (Fournier 1999). As the temperature increases, the mechanical behavior of the rock changes at BDT, leading to a change in deformation mode from brittle fracturing to plastic flow, closing connected fluid flow paths. Studies show that heat transport would be conduction-dominated if permeabilities are below 10^{-16} m^2 (Norton and Knight 1977; Cathles 1977), and drilling into such conditions would encounter uneconomic rates of fluid production. Previous experimental results suggested that permeability may still be sufficiently high to extract fluids at BDT under certain stress and temperature conditions (Watanabe, Numakura, Sakaguchi, Saishu, Okamoto, Ingebritsen and Tsuchiya 2017). In case of insufficient fracture density, enhancement strategies such as hydraulic fracturing are likely to be successful (Watanabe, Egawa, Sakaguchi, Ishibashi and Tsuchiya 2017), proving that applying EGS techniques in reservoirs with low permeabilities close to the ductile crust is possible.

At present, the functional exploitation of supercritical geothermal resources for industrial use is still not possible due to unresolved technical difficulties. One is that, the high content of dissolved gases and solids in the aqueous fluids due to high temperature and pressure conditions makes the geothermal brine much more acidic and metal-rich than dilute geothermal water, resulting in corrosion and scaling of the borehole of surface equipment (Hardardóttir et al. 2010). As such, the handling of fluid and the development of corrosion-resistant material can be elaborate and expensive. Drilling wells to supercritical fluid reservoirs is also an enormous challenge. At extremely high temperatures of 400 °C and more, the temperature resistance of casing materials, drilling mud, geophysical logging instruments, as well as the strength of the materials still pose great limitations. For example, even those robust drills made of special steel alloys can withstand harsh conditions only thanks to the massive injection of cooling

water. Cooling may also be required during well logging as mostly accessible tools can only operate under 300 °C for temperature logging and 150–260 °C for geophysical logging such as seismic, acoustic, resistivity, etc (Lee 2019). Another common problem in geothermal wells is circulation losses, usually due to typical fracturing of the formations in a geothermal field, or damaged strings and casings caused by thermal fatigue or acid corrosion. The performance of the cement job in the loss zones can be severely affected due to the impact of the high temperature environment on the kinetics of cement setting. For further detailed descriptions of the challenges/failures encountered during the drilling some high-enthalpy exploration wells, reference can be made to the reviews by Reinsch et al. (2017), Kruszewski and Wittig (2018) and Tomac and Sauter (2018). To meet the current requirements in the development of supercritical geothermal systems, innovative exploration, measurement and logging technologies are needed. In parallel, advanced methods for evaluating and interpreting the sparse and valuable data are in great demand to overcome the current limitations in data acquisition.

1.2 Motivation: the drilling of the RN-15/IDDP-2 well aimed for supercritical geothermal resources

The RN-15/IDDP-2 well is drilled as part of the Iceland Deep Drilling Project (IDDP) operated by HS Orka, which aims to increase power production at the Reykjanes geothermal site from 100 MWe to 150 MWe by exploiting supercritical geothermal resources (Friðleifsson et al. 2011). To achieve this goal, it is expected that a reservoir temperature of 450–600 °C will be reached and supercritical fluids can be produced from a depth of 3.5 km to 5 km. The entire drilling phase consisted of deepening the existing RN-15 well from the original depth of 2507 m to a slant depth of 4659 m (4.5 km vertical depth), with the deeper well referred to as IDDP-2. A major challenge during the drilling operation was the total circulation loss below 2.5 km, which could not be remedied by blocking materials or by multiple cement jobs. Accordingly, drilling continued to total depth with no cuttings returned. Highly permeable zones were encountered at multiple depth levels below 3 km depth to bottom, with the largest loss occurring at about 3.4 km.

Since the main objective to drill the RN-15/IDDP-2 well is to reach supercritical reservoir conditions and evaluate the energy potential of the geothermal site, it is of great interest to obtain an estimate of the temperature distribution along the depth in

the target region. Prior to the drilling, the formation temperature profile in the upper 2.5 km was derived from direct temperature measurements in the old RN-15 well during a maintenance shut-in in 2010 (Jónsson et al. 2010). To determine the formation temperature below 2.5 km, several conventional methods are expected to provide some insight using different types of data, such as the geochemical composition of fluids, retrieved drill cores, geophysical logs, and temperature measurements from the well and other nearby wells. However, due to the total loss of circulation, some of the measurement instruments, including the gas spectrophotometer and sampling device on the flowline provided by the ICDP-OSG at GFZ, and the conductivity and pH sensors set up by ISOR and HS Orka, could not provide useful data during the drilling (Friðleifsson et al. 2017). In addition, few results have been published on the success of deep formation fluid sampling and compositional analysis (Friðleifsson et al. 2020). The first pressure and temperature logs showing that the well reached supercritical conditions were obtained on January 3rd, 2017. The measured temperature is 426 °C and the pressure is 34.0 MPa near the well bottom. Since around 40 L/s of cold water was injected at the wellhead to cool the well at the time of logging, it could be assumed that the well was far from thermal equilibrium and that the maximum formation temperature was, therefore, certainly higher than 426 °C.

To the author's knowledge, four studies have presented their work on the evaluation of the formation temperature for the RN-15/IDDP-2 well at the time of this writing. Based on pressure/temperature regimes at various depths derived from measurements of other wells in the region, Fridriksson et al. (2015) considered three possible fluid states in the well: subcritical single-phase fluid, superheated steam, and a mixture of low salinity vapor and brine. They arrived at very different temperature values at 5 km depth: 382 °C, 441 °C and 550 °C. Zierenberg et al. (2017) carried out preliminary analyses of the drilled cores to identify the hydrothermal alteration minerals that provide rough constraints on the maximum possible formation temperatures, which range from 450 °C to 600 °C. Hokstad and Tanavasuu-Milkeviciene (2017) applied a multi-geophysical inversion method to first predict the formation temperature for the pre-drill condition. This was done by integrating electrical resistivity and density models obtained from the inversion of magnetotelluric (MT) and gravity data, followed by a joint Bayesian inversion procedure. The formation temperature at 5 km vertical depth was estimated to be 513 ± 62 °C. In a second step, a resistivity log acquired during drilling was used to update the temperature estimate. The result was 50-100 °C higher than the prediction for the condition before drilling. This may be due to the uncertainties introduced by the resistivity correction procedure due to the cooling effect of the injected water. In addition, the assumed trend of porosity as a function of depth is another source of uncertainty due to insufficient data, leading to an inherent

ambiguity in the inversion since porosity has a similar effect on resistivity and density as temperature, according to the rock physics model. The final study is based on direct temperature measurements during a one-week warm-up experiment in late May 2017, during which four consecutive temperature logs were measured. Therein, Tulinius (2017) applied the so-called Horner-plot method which requires temperature values recorded at different shut-in times (i.e., no fluid injection in the well) to calculate the equilibrium formation temperature. The highest temperature estimate is 535 °C at about 4.6 km slant depth. However, during the temperature logging, the well was not in a strict shut-in condition as 5 L/s of cold water was still injected into the annulus between the well and a 7" stimulation liner string to cool the well casing. Although most of the flow was assumed to be lost to the formation after some depth, it is difficult to confirm whether the shut-in condition exists in the measured deeper parts of the well, so the effect of any residual flow on temperature predictions is unclear.

The extremely hot conditions and presence of loss zones in the well RN-15/IDDP-2 clearly complicate the interpretation of the drilling and logging data. Although the above research shows promise in using different types of field data to determine formation temperature, most of these approaches do not constrain the formation temperature well and would still rely on further future investigations. In this context, the obtained temperature data, especially those measured during drilling under injection conditions, are still very valuable for assessing the down-hole condition of the borehole. In combination with advanced numerical simulations and interpretation techniques, these data may overcome the lack of information. The RN-15/IDDP-2 well, located in the Icelandic geothermal system, provides a natural case study that tests proposed research methods against real-world cases. Therefore, the results of this dissertation will also inform ongoing efforts by existing deep drilling projects to exploit high-enthalpy geothermal resources.

1.3 Access and evaluation of formation temperature using temperature data

Exploration of geothermal resources often faces a significant amount of uncertainties and risks due to the fact that geothermal energy is stored mostly deep underground. It has been widely recognized that the exploration risk for a geothermal project can be defined as: not achieving an economically acceptable production capacity with minimum flow rates and formation temperatures (Schulz et al. 2007). This can be

explained through a simple quantification for the potential of a geothermal reservoir using the formula (Jha and Puppala 2017):

$$EP = \int_{t_s}^{t_e} \dot{m} \Delta \dot{h}(T_{in}, T_p, t) dt, \quad (1.1)$$

where EP is the geothermal energy potential, \dot{m} is the produced mass flow rate, t_s and t_e are the starting and ending time for the production, $\Delta \dot{h}$ is the difference between the carried enthalpies of the injected and produced fluid which depends on the injection (T_{in}) and production temperature (T_p) respectively. Theoretically, T_p depends on the temperature of the rock formation (T_s), the flow rate Q and the production time $t_e - t_s$. For long periods of fluid production under high flow rates, the difference between T_p and T_s becomes much less distinct, which further leads to a rough estimation for the amount of geothermal energy extraction, $P \propto Q \cdot T_s$. Therefore, formation temperature is a crucial parameter both for assessing the heat reserve of a reservoir before the drilling and later for determining the installed capacity of a geothermal plant.

1.3.1 Data acquisition

The temperature of the subsurface is normally directly accessed by conducting temperature measurements in a borehole. These measurements are then interpolated or extrapolated to get more extensive information about spatial variation of the temperature distribution (Agemar et al. 2012; R uhaak et al. 2014). Typically, temperature data are available as single values recorded at the bottom-hole (bottom-hole temperatures, BHTs) or as temperature-depth profiles (temperature logs). During a conventional temperature logging process such as wire-line logging, temperatures are recorded while the sensor or the probe is moving down inside the borehole or reaching the target depth. In contrast, recent logging tools developed based on fiber-optic distributed temperature sensing techniques (DTS) are more advanced by allowing instantaneous temperature profile sampling with high spatial resolution (Fenta et al. 2021). Such advancement will enable a much more efficient acquisition of temperature data as nowadays they are still relatively sparse compared to other types of geophysical logs (Maryadi and Mizunaga 2021).

Most temperature logging devices are rated for continuous operation limited to 175 °C, and only a few tools can tolerate up to 300 °C (Lee 2019). As of today, the development of logging technologies and instruments is highly demanded to follow the needs for deep geothermal resource exploration. In several high-temperature

drilling projects, temperature logging devices have been designed to withstand the hostile down-hole conditions. Some of these tools are based on logging to an internal memory system and powered by high-temperature resistant batteries. The measured temperature is allowed to reach the critical point of water at around 374 °C (the HiTI project) or even higher at 450 °C (the DESCRAMBLE project) (Ásmundsson et al. 2014; Vedum et al. 2017). However, the short endurance time of these tools (up to eight hours as reported) remains a limitation when obtaining temperature measurements under certain borehole operating conditions such as the so-called shut-in or thermal-recovery period, when the temperature rises after injection or production have stopped or the flow rate is reduced to very low values (Reinsch et al. 2017).

1.3.2 Uncertainties in the data

Besides the temperature data acquisition tools, proper interpretations of these data are also crucial. The interpretation of temperature measurements in mechanically drilled deep boreholes filled with drilling fluids can be complicated for several reasons. First, temperature data are usually recorded soon after drilling. Due to the thermal disturbance from the drilling fluid caused by its temperature difference with the surrounding formation and additional frictional heat introduced by the drilling bit, the measured temperature often deviates from the true (i.e., static or undisturbed) formation temperature and needs to be corrected. Second, since the temperature is measured in the borehole fluid, not in the surrounding formation, an important consideration is to account for the heat transfer mechanism between the borehole fluids and the contacting wall. Usually, the thermal equilibrium condition needs to be justified before the measurement. Third, convective mixing driven by density difference in a static water-filled column in the borehole can establish due to the vertical temperature gradient (Diment 1967; Gretener 1967; Pfister and Rybach 1995; Klepikova et al. 2018). Fourth, the temperature measurements have an inherent uncertainty due to the sensor response time, noise from built-in electronics, incorrect recording depth due to cable elongation and slippage, etc (Clow 2008; Sharma et al. 2021). Thus, temperature logging inside deep boreholes should obey a proper protocol in terms of the logging speed, the measurement direction, borehole settling time, and so on to improve the quality of the data (Talalay et al. 2020).

1.3.3 Data interpretation

Till now, a majority of the studies concerning the determination of the static formation temperature from borehole temperature measurements have been relying on several classical analytical models that were established between the 1940s and 1980s to predict the thermal response of the borehole fluid during and after the drilling. These methods require at least three or more BHT measurements carried out at the same borehole depth but at different shut-in times. However, large discrepancies between the predictions and the true (synthetic) SFT, as well as among the predictions using different models, are very often found when applying those methods (Espinoza-Ojeda et al. 2011). For instance, in a comparison study from Andaverde et al. (2005), the prediction error from analytical models for the synthetic data sets can be around 10%. However, the deviation among the prediction results for the real-world data can be over 100 °C. These discrepancies are typically associated with the underlying oversimplification of the physical model compared to the real borehole drilling process when assuming a constant cooling source (Bullard 1947), or an unrealistic thermal transfer model between the borehole and the formation by considering the same thermal properties of the formation and the borehole fluid (Leblanc et al. 1981), as well as those uncertainties from the measured data mentioned previously.

On the other hand, modern numerical methods provide opportunities to resolve the technical aspects of simulating all the principal heat flow mechanisms involved in the thermal recovery of a borehole and surrounding formation from the drilling disturbance (Kohl et al. 2002; Espinosa-Paredes and Garcia-Gutierrez 2003; Raymond et al. 2011; Pan and Oldenburg 2014; Korzani et al. 2019). Moreover, insights into the dominating physical processes and the interactions between them can be gained by specifying the number of control parameters and performing uncertainty and sensitivity analysis (Fernández et al. 2017; Fuchs and Balling 2016; Konrad et al. 2019). So far, only a limited number of studies have adopted numerical methods in the procedure of formation temperature prediction (Espinosa-Paredes and Garcia-Gutierrez 2003; Yang et al. 2015). However, the simulated scenarios are still relatively simple (e.g., continuous mud injection with a constant injection rate and simplified heat transfer model for the shut-in phase), and a general approach for quantifying the uncertainties in the estimation procedure is still missing.

1.4 Thesis overview

The focus of this cumulative dissertation is in the context of deep drilling and high-temperature geothermal exploration, and aims at two major aspects: firstly, to gain an improved understanding of the key factors that control the borehole thermal process during drilling operations by performing numerical investigations. Secondly, to develop reliable and efficient interpretation methods for borehole temperature data to determine key parameters for geothermal exploration and to quantify the associated uncertainties rigorously. In particular, my study mainly focuses on interpreting temperature logs obtained from high-temperature boreholes under injection (or cooling) conditions. In other words, the present work is based on the use of thermal information acquired from borehole under subcritical conditions to infer the initial undisturbed thermal condition of the reservoir, which could be in the supercritical state. Such a concept arises from the unique challenges of obtaining thermal recovery data from wells in high-temperature environments, such as the RN-15/IDDP-2, due to the limitations of logging instruments (section 1.3.1) and safety concerns regarding borehole casing programs (Kruszewski and Wittig 2018).

The first part of this dissertation (chapter 2) provides the fundamentals of heat transfer mechanisms that occur within the borehole, and between the borehole and its surrounding formation. Therein, the governing equations for the thermal modeling and the underlying assumptions, as well as the relevant empirical relationships controlling the heat transfer process, are introduced. In addition, an overview of the classical analytical models for deriving the SFT is given, and the limitations and validity of their applications are presented. Thereafter, the manuscript consists of three progressive studies that address the following questions:

- What are the key factors influencing the borehole temperature distribution under different flow conditions? (Chapter 3)
- Which data and methods are suitable for predicting SFT for high-temperature wells operated with intensive injections and which are not? (Chapter 3 and Chapter 4)
- How much are the uncertainties in the SFT estimates when inverting injection temperature logs? (Chapter 4)
- Can the SFT be solved together with unknown drilling losses from temperature observations through inverse modeling? (Chapter 5)

The answers to above questions are provided in the following outlined studies:

Temperature log simulations in high-enthalpy boreholes (chapter 3)

This study has been published in *Geothermal Energy*.

In the first study, various flow conditions (e.g., flowing and shut-in) are simulated to mimic real-world drilling operations for high-temperature boreholes. The lack of understanding of the critical processes controlling the temperature evolution in the well under complex drilling conditions was the incentive for conducting this numerical investigation. These drilling conditions involve drilling (or circulation) losses and different flow conditions such as injection and shut-in in different well sections (e.g., drill pipe and annulus) due to the specific requirements of continuous cooling for a high-enthalpy well. The results highlight the important role of free convection in the thermal recovery during shut-in period and show that parameterization of the contribution of free convection to the overall heat transfer rate may be required. The injection temperature log can be used to identify and characterize the flow losses, as the temperature distribution in the borehole along the depth is susceptible to the flow rate. It can also be shown that conventional methods using thermal recovery data to derive the SFT may not be applicable to high-temperature wells that are not in a fully shut-in condition even when they are operated at very low flow rates. This synthetic study serves as the basis for the selection of well data used to estimate formation temperature and for the development of an inverse modelling scheme for the two subsequent studies.

Uncertainty analysis of the numerical inversion of temperature logs from boreholes under injection conditions (chapter 4)

This study has been published in *Journal of Geophysics and Engineering*.

Based on the results of the previous study, injection temperature logs are then investigated for their applicability to derive SFT for high-temperature wells. The focus of this study is to develop a rigorous method for evaluating various factors that influence the accuracy of SFT estimates. These factors involve many aspects such as the injection conditions (time and flow rate), the logging methods, the presence of circulation loss zone, the quality of the temperature data, and the constraints applied in the inversion procedure. The applied inversion scheme was based on a data-driven approach using the machine learning algorithm (k-nearest neighbor) and proved to be very efficient in finding the solution space of parameters leading to temperature logs having the same quality of fit to the correct borehole temperature. One of a major findings of this study is that SFT estimates derived from temperature logs measured after higher flow rate injection or longer injection times are more reliable. Furthermore, the estimation error

in SFT exhibits an almost linear dependency on the standard error of the temperature measurement. The flow losses and the SFT show a strong positive correlation when they are jointly estimated. Therefore, the combination of flow logs or prior knowledge about the amount of flow loss may be necessary in order to correctly interpret the temperature data.

Surrogate-based inversion of borehole logs for formation temperature determination (chapter 5)

This study is prepared for publication in a scientific journal.

The final study is intended to fill up the gap between the work in chapter 4, where a deterministic approach is used to quantify the uncertainty of estimation parameters in the inversion of temperature data. In this study, the inverse problem is solved in a statistical framework by constructing the posterior probability density function (PPDF). The Bayesian inference approach—Markov Chain Monte Carlo is applied to construct the PPDF for the estimation parameters, such as the SFT and flow losses. To address the fundamental problem of the high computational cost of PPDF sampling, the forward models are run using surrogate models trained with artificial neural networks. The inversion method is first successfully verified with synthetic logs and then applied to the temperature data of the RN-15/IDDP-2 well to jointly estimate the SFT and unknown flow loss at three different depths. It is found that drilling losses can be well constrained for this well using an injection temperature log regardless of the assumed number of geothermal layers (e.g., layers that are divided according to the change in geothermal gradient). In contrast, there can be significant differences in SFT estimates when different numbers of geothermal layers are used. Nevertheless, the estimate of the SFT at 4500 m from this study is in good agreement with other relevant studies.

Chapter 2

Fundamentals of heat transfer in the borehole and formation

The thermal state of a geothermal system is not only affected by natural processes but also human activities during geothermal energy exploration and exploitation, such as the drilling of boreholes, flow testing, injection and production of fluids, etc. One of the most important physical properties used to study a thermal process is temperature. It is a parameter that varies both spatially and temporally on different time scales, from the temperature variation within a few hours when monitoring a borehole to the evolution of the whole Earth's thermal field (as a large geothermal system) that lasts billions of years. Temperature differences between different structures will be equilibrated through heat transfer.

The focus of this chapter is on the heat transfer occurring in the borehole scale and in the formation, and the thermal interaction between the borehole and the formation. Understanding the physical processes that control the heat transfer within the borehole-formation is essential for thermal modeling of the system, as well as identifying key factors for a successful interpretation of the temperature data. This chapter presents the fundamentals of heat transfer mechanisms and some of the most classical thermal models for deriving the formation temperature in a thermal equilibrium state.

2.1 Heat transfer in the formation

Temperature, as a physical property that determines the direction of heat flow, is considered to increase with depth, thereby causing geothermal heat to flow from the earth's interior to the surface. In general, there are three types of heat transfer

mechanisms that can occur either separately or simultaneously when heat flows, namely conduction, convection, and radiation. Heat conduction dominates primarily in low-porous and impermeable rock types, such as plutonic and metamorphic rocks, but also in sediments being low permeable to impermeable such as highly compacted sandstones, mudstones and dense carbonates. Convective heat transport dominates in permeable rock formations such as porous sediments or highly fractured rocks, where fluids can circulate through the interconnected pores and fractures. Radiation is another that mainly exists in the continental crust, which contributes to the heat flow. The following discusses the basic concepts of these mechanisms and their respective roles in deciding the heat flow and temperature distribution inside the earth.

2.1.1 Physical processes

Heat conduction

The conductive heat transfer is described by the Fourier's law which has the following differential form:

$$q_{cond} = -\lambda \cdot \nabla T, \quad (2.1)$$

where q_{cond} is the heat flow per unit area per unit time (also known as heat flux, W m^{-2}), λ is the thermal conductivity ($\text{W m}^{-1} \text{K}^{-1}$) and ∇T is the temperature gradient. The negative sign indicates the heat flows in the direction of the negative temperature gradient (i.e., from warm to cold body). When considering the heat flow of the Earth, the heat flux is towards the surface (one-dimensional), i.e., $\lambda \partial T / \partial z$ where the z -axis extends vertically downward.

For porous structures such as rocks, the value of λ is an averaged quantity that depends on the porosity, water saturation, mineral composition (Schön 2015). Typical rocks have λ values ranging from 1.5 to 10 $\text{W m}^{-1} \text{K}^{-1}$, with most igneous rocks such as basalt and granite having a narrower range between 1.8 $\text{W m}^{-1} \text{K}^{-1}$ and 3.5 $\text{W m}^{-1} \text{K}^{-1}$. From surface to deep underground, thermal conductivity can not be considered as a constant due to great temperature and pressure differences. Experiments show that λ and T have an inverse-proportional relationship up to about $T = 700 \text{ }^\circ\text{C}$. According to Buntebarth (2012), the following empirical relation between λ and T can be applied:

$$\lambda = 1/(a + bT) \quad (2.2)$$

where T is in $^{\circ}\text{C}$. For the upper crust, a is 0.33 m K W^{-1} and b is $0.33 \times 10^{-3} \text{ m W}^{-1}$, for the lower crust, a is 0.42 m K W^{-1} and b is $0.29 \times 10^{-3} \text{ m W}^{-1}$. The impact of pressure on λ also depends on the magnitude of the pressure itself. Under low pressures, rock porosity gradually decreases with increasing pressure, and the closure of pores leads to increased λ . At pressures up to 100 MPa, the pressure correction for crustal rocks is about 10%. Under greater pressures, there is only slight increase of λ (about $2 \times 10^{-3} \text{ W m}^{-1} \text{ K}^{-1}$ per 100 MPa) due to crystal lattice deformation (Schloessin and Dvorak 1972). In a normal geothermal setting where temperature and pressure increase with depth, the temperature and pressure would therefore cause opposite trends in the change of λ . Due to lack of sufficient data where λ was measured simultaneously as a function of temperature and pressure, most current thermal models often ignore the corrections to in situ λ (Fuchs and Balling 2016; Freyemark et al. 2017; Przybycin et al. 2015). A few studies in which both temperature and pressure dependencies are taken into account for λ at depths relevant for geothermal exploration (i.e., the uppermost crust) are published, for example, by Schintgen et al. (2015), Förster et al. (2018) and Norden et al. (2020).

The temperature gradient in Eq 2.2, also called geothermal gradient, varies in different regions from as low as $10 \text{ }^{\circ}\text{C km}^{-1}$ in stable continental region, to more than $200 \text{ }^{\circ}\text{C km}^{-1}$ in volcanic zones (Kranz 2006). Assuming a typical gradient of $25 \text{ }^{\circ}\text{C km}^{-1}$, the heat flux is estimated to be around 60 mW m^{-2} . In practice, geothermal heat flow in formations is determined by assuming conductive flow in a vertical direction (Eq 2.2). In some cases, the heat flux must be corrected to account for laterally varying thermal conductivity (e.g., due to non-horizontal thermal contact between formations, resulting in a distortion of the heat flow in the vertical direction) and inclination of the borehole (when calculating the geothermal gradient). Moreover, there can be other effects due to topographic relief, paleo-climatic change and groundwater motion through fracture and permeable formations. These effects are discussed in Chapter 2.1.4.

Heat convection

The convective heat transfer occurs through a combination of molecular collision and energy transportation during the movement of fluid particles. Fluid flow in the

reservoir is commonly defined according to Darcy's law by:

$$v_D = -\frac{K}{\mu}(\nabla P + \rho_f g), \quad (2.3)$$

where v_D is the Darcy's velocity (m/s), K is the rock permeability (m^2), μ is the fluid's dynamic viscosity ($\text{Pa}\cdot\text{s}$), P is the pore pressure (Pa) and ρ_f is the density of the fluid (kg m^{-3}).

According to Eq 2.3, the movement of geothermal fluid is controlled by both the properties of both the fluid (μ and ρ_f) and the rock (K). μ and ρ_f are determined using the so-called equations of state (EOSs) that describe both bulk fluid properties and the thermodynamic properties of the dissolved rock components (in case of fluid-rock interaction) over wide ranges of temperature, pressure, and chemical composition. EOSs are considered fundamental for modeling hydrothermal processes and accurate formulations for water as the most relevant geothermal fluid have been available for several decades (Wagner and Pruß 2002; Johnson et al. 1992; Driesner and Heinrich 2007). The biggest challenge for comprehensive geochemical modeling so far is the missing of valid EOSs for aqueous solutes and chemical reactions over the whole range of geothermal conditions in the Earth's crust. This is especially relevant for conditions that are difficult to handle experimentally, namely moderate pressures between 10 MPa and 30 MPa and temperatures above 350 °C, as encountered in geothermal systems such as mid-ocean ridge hydrothermal convection, magmatic-hydrothermal systems, and deep root zone high-enthalpy systems (Stefánsson et al. 2018).

In a natural formation, permeability, K , is a key controlling physical parameter for the exploitation of geothermal resources, as economic fluid production rates are only possible when the formation is sufficiently permeable. When permeability is below 10^{-16} m^2 , the predominant heat transfer mechanism in the formation will change from convection to conduction (Cathles 1977; Norton and Knight 1977). The primary factors affecting K are pressure and temperature. It has been long established that permeability will decrease as the effective stress increases due to compaction of the rock structure, leading to a decrease in pore volume (McLatchie et al. 1958; Shmonov et al. 1994). The temperature dependence of K can be more complex. Both increases and decreases in K can occur with increasing temperature, and the reasons have been linked to either the closure of intergranular channel way or the cracking of grains as a result of anisotropic and inhomogeneous thermal expansion coefficients of mineral grains in the rock (Potter 1978; Liu, Li, Tian and Wu 2018).

Depending on the cause of the fluid motion, convection is further distinguished by two

mechanisms. One is free convection or natural convection that is driven by buoyancy forces, which are induced by density differences due to the temperature gradient existing in an aquifer. Free convection is taken into account in the calculation of the velocity vector in the second constitute of Equation 2.3. The other is called forced convection or very often advection, which is controlled by pressure gradients (∇P , Equation 2.3) caused by variations in the groundwater level. The convective heat flux is then given by:

$$q_{conv} = \rho_f c_{pf} v_D T, \quad (2.4)$$

where c_{pf} is the specific heat capacity of the fluid.

Radiogenic heat production

The radiogenic heat production of rock in the shallow crust is the largest internal source of heat for the Earth and an important contribution to terrestrial heat flux, apart from the mantle heat flow (Korenaga 2011). The radiogenic heat production mainly comes from three unstable radioactive isotopes: uranium (C_U), thorium (C_{Th}), and potassium (C_K). According to Haenel et al. (2012), the generated heat can be estimated using the following formula:

$$R = 10^{-5} \cdot \rho_s \cdot (9.52C_U + 2.56C_{Th} + 3.48C_K) \quad (2.5)$$

where R is the radiogenic heat production of rock ($\mu\text{W m}^{-3}$), ρ_s is the rock density (kg m^{-3}). C_U , C_{Th} and C_K are the concentrations of uranium and thorium in parts per million (ppm) and potassium in weight percent (wt.%), respectively. These concentrations can be directly measured from core samples (Liu, Giroux, Harris, Quenette and Mansour 2018) or derived from geochemical models data (Murthy 2007). If such data are not available, the heat radiogenic production can also be inferred from its correlation with the seismic velocity (Cermak et al. 1990) and by conducting mineral physics and thermodynamic modeling (Mattern et al. 2005).

2.1.2 Conservation governing equations

With the three heat flux component introduced previously, the energy conservation equation in the formation can be written as:

$$\rho_m c_{pm} \frac{\partial T}{\partial t} + \rho_f c_{pf} \nabla(\mathbf{v} \cdot T) - \lambda_m \nabla^2 T - R = 0. \quad (2.6)$$

The subscript m indicates that the properties are averaged over the fluid-filled pores and the solid matrix by their volume contributions which are characterized by the porosity ϕ . For the scalar quantity, thermal capacity ($rhoc_p$), simple arithmetic mixing rule can be applied (i.e., Kopp's law). For instance:

$$\rho_m c_{pm} = \phi \rho_f c_{pf} + (1 - \phi) \rho_s c_{ps}, \quad (2.7)$$

Thermal conductivity depends on both λ_f and λ_s and on the configuration of grains and pores (Bear 2018). Different mixing laws for λ_m are discussed in Clauser (2006), the following simple mixing law is still widely used:

$$\lambda_m = \lambda_f + (1 - \phi) \lambda_s. \quad (2.8)$$

The velocity component, \mathbf{v} , in Equation 2.6 is the Darcy velocity as defined in Equation 2.3. To complete the formulation of the problem, the mass conservation equation is required:

$$\frac{(\phi \rho_f)}{t} + \nabla(\rho_f \mathbf{v}) + q = 0, \quad (2.9)$$

where q ($\text{kg m}^{-3} \text{s}^{-1}$) is the sink/source term for the mass flow.

2.1.3 Analytical solutions for classical thermal problems

Equation 2.6 can be solved for a defined thermal problem according to the thermal-hydro properties of the fluid and rock materials and the prescribed boundary conditions. Herein, solutions to selected classical heat transfer problems, taken from Turcotte and Schubert (2002), are illustrated. Only 1-D steady-state problems are presented to illustrate some of the key factors affecting the distribution of formation temperature. Solutions for time-dependent problems with different boundary conditions can be consulted from Jaeger and Carslaw (1959).

1-D thermal conduction

Under a one-dimensional steady state condition, the temperature distribution in the formation satisfies:

$$\frac{d}{dz} \left[\lambda \frac{dT(z)}{dz} \right] + R = 0 \quad (2.10)$$

The applied boundary condition at $z = 0$ is

$$T(z = 0) = T_0, \quad (2.11)$$

and at the bottom depth ($z = H$) of the formation is:

$$\left(\frac{dT}{dz} \right)_{z=H} = \frac{q}{\lambda} \quad (2.12)$$

The solution for the temperature distribution of the formation $T(z)$ is:

$$T(z) = T_0 + \frac{1}{\lambda} qz + \frac{RH}{\lambda} z - \frac{R}{2\lambda} z^2 \quad (2.13)$$

1-D thermal convection

Advection is an important heat transport mechanism in a hydrothermal system. The hot intrusions heat the groundwater that becomes less dense and rises. During up-welling, the water cools and its density increases. It then sinks and recharges the aquifers and porous rock near the intrusion, which in turn starts the next cycle of the circulation process. To illustrate the phenomenon of up-welling flow, a one-dimensional model is described here. Assuming a steady, incompressible upward flow process, Equation 2.6 and Equation 2.9 can be simplified to:

$$\frac{dv}{dz} = 0, \quad (2.14)$$

$$\rho_f c_{pf} v \frac{dT}{dz} - \lambda_m \frac{d^2 T}{dz^2} = 0. \quad (2.15)$$

Assuming a constant temperature T_0 at the surface and uniform reservoir temperature T_r at great depth, the boundary condition at $y \rightarrow \infty$ is:

$$\begin{aligned}\frac{dT}{dz} &= 0 \\ T &= T_r\end{aligned}\tag{2.16}$$

The formation temperature as a function of depth z is given by:

$$T = T_r - (T_r - T_0) \exp\left(\frac{\rho_f c_{pf} v}{\lambda_m} z\right),\tag{2.17}$$

By adopting some representative values for the parameters, e.g., subsurface temperature T_0 : 20 °C, thermal conductivity λ_m : 3.0 W m⁻¹ K⁻¹, density of fluid: 1000 kg m⁻³, heat capacity of fluid: 4185 J kg K⁻¹, groundwater flux v : -6×10^{-8} m s⁻¹, surface heat flux q : 60 mW m⁻², radiogenic heat production rate R : 1 μW m⁻³, the formation temperature from surface to 5 km can be calculated for four different scenarios using Equation 2.13 and Equation 2.17. Case (1): pure thermal conduction; case (2): thermal conduction with radiogenic heat production; case (3): pure thermal conduction in formation consisting of two layers having different thermal conductivity (first layer: 3 W m⁻¹ K⁻¹, second layer: 2 W m⁻¹ K⁻¹); case (4): pure thermal convection. The formation temperature profile for each case is plotted in Figure 2.1, and discussions based on this figure is given in Chapter 2.1.4.

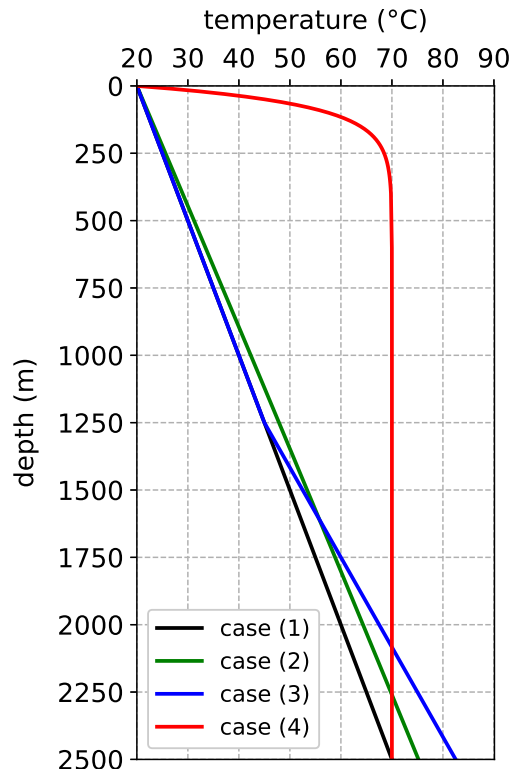


Figure 2.1: Formation temperature profile for four different cases: (1) heat conduction (black line), (2) heat conduction with radiogenic heat production (green line), (3) heat conduction in formation with varying thermal conductivity (blue line), and (4) heat convection (red line).

2.1.4 Impact factors on the temperature distribution in the subsurface

The most effective method of gathering information about subsurface temperature is to conduct temperature measurements in boreholes. Numerous studies have been conducted to use these measurements to resolve some of the very important parameters for geothermal developments, such as the heat-flux and groundwater flux, or rock properties, such as the thermal conductivity; or to assist the analysis of other geophysical logs, such as flow log and resistivity logs. In many cases, these studies are undertaken by fitting the measured data with the data predicted using developed models. However, the underlying risk of such a process is the oversimplification of the thermal models (e.g., neglecting key processes, applying constant parameters, etc.), which may create inconvenient misfits during the data calibration process. Therefore, it would be necessary to understand the factors that would affect the subsurface temperature distribution for more reliable interpretations of the temperature observations.

Radiogenic heat production

Radiogenic heat production causes variation in heat flow along with the depth and thus also thermal gradient. According to Equation 2.13, the thermal gradient is not linear but a quadratic function of depth. The heat flow is higher at the surface than at depth. According to the simple example calculated in Chapter 2.1.3, the uppermost few hundred meters is relatively insensitive in heat production. But as depth increases, the impact of the heat production also increases. The temperature increase caused by heat production at 2500 m is only 5 °C, which is not significant compared to these impacts from thermal conductivity and fluid convection, according to Figure 2.1. However, as radiogenic heat production exists on a crustal-scale with can generally extend to 30–45 km deep (Mooney 2003), the radiogenic heat production can be an important heat flow component to the terrestrial heat flow that accounts for 30–40% of the total heat flux (Hokstad et al. 2017; Turcotte and Schubert 2002; Mareschal and Jaupart 2013). In some research studies, the locally anomalously high heat flow is found to be related to radiogenic heat production. In a series of studies conducted on the Cooper Basin (Australia), high heat production of 3.8–8.7 $\mu\text{W m}^{-3}$ in basement granite and thick sedimentary rocks with low thermal conductivity acting as a thermal barrier resulted in high temperature of 240 °C at 3.5 km depth (Hillis et al. 2004; Meixner and Holgate 2009; Meixner et al. 2014). In Zhang, Hu, Zhang, Li, Zhang, Kong, Zuo, Song, Jiang and Wang (2020), the radiogenic heat production is found to be about 48.3 mW m^{-2} , 47.3% of the high terrestrial heat flow and is therefore an important source of hot dry rock geothermal resources in the studied area. Furthermore, as pointed out from Zhou (2013), the exact value of radiogenic heat production may have a fine-tuning effect on the results when calibrating formation temperature predictions from numerical models using field temperature measurements.

Thermal conductivity

Unlike radiogenic heat production, variation in thermal conductivity only affects the thermal gradient but not the heat flow. As shown in the previous example, the impact of a change in the thermal conductivity on the temperature distribution can be depth-dependent. Namely, the decrease of thermal gradient from 3 $\text{W m}^{-1} \text{K}^{-1}$ to 2 $\text{W m}^{-1} \text{K}^{-1}$ within the second layer only causes a temperature increase of less than 1.0 °C in the upper 100 m but results in 13 °C temperature increment at a depth of 1250

m in that layer. Another perspective related to thermal conductivity is the presence of geological layers that consist of sand, clay, and moraine materials which can have far lower thermal conductivity values compared to other rock types Midttoemme (1997). These layers, sometimes also called overburden layers, can act as thermal blankets that dramatically increase the formation temperature at depths. However, according to the calculations from Slagstad et al. (2008), in shallower geothermal systems, thick low-conductivity layers (from the surface at least 50 to 100 m) or with unrealistically low thermal conductivity values are required to produce temperature anomalies of only a few degrees (less than 2 °C). Drilling through the overburden layers would often require the boreholes to be cased, which leads to higher drilling costs (Hossain 2015). The existence of such layers can discourage the extraction of ground source heat despite their advantage for providing higher temperatures.

Groundwater convection

Groundwater convection can redistribute the conductive formation temperature profile due to the movement of heat carrier fluid in the reservoir. As shown in Figure 2.1 (red dash line), convection of high-temperature fluid upward can cause a very high thermal anomaly at the shallower depth which significantly increases the geothermal potential of the formation. In fact, studies show that convective fluid flow can leave a distinct pattern on the local geothermal gradient indicated by borehole measurements. A well-studied case is the Soultz-sous-Forêts geothermal project in the Upper Rhine Graben. At the beginning of the project, borehole temperature data at 1000 m depth was found to be above 110 °C and temperatures of 150–170 °C were expected at a depth around 2000 m (Guillou-Frottier et al. 2013). However, in reality, a temperature of 160 °C is only found at 3600 m. The temperature gradient was found to decrease below 1000 m within a permeable sandstone formation and become very low in a permeable granitic basement and then recovered to normal (30 °C km⁻¹) below 3500 m in the poorly permeable granitic basement (Genter et al. 2010). Numerical modeling has been conducted to reproduce the observed temperature data and concluded that these thermal features, i.e., both high and low thermal anomalies, can only be explained by fluid circulation occurring in the fractured formation (Kohl et al. 2000; Guillou-Frottier et al. 2013; Magenet et al. 2014). Furthermore, the thermal effect is found to be critically dependent on the pre-existing thermal gradient, the thickness, and the permeability of the geological layers (Pasquale et al. 2013; Niederau et al. 2019). The justification of the buoyancy force induced thermal convection (Chapter 2.1.1) can be

carried out using Rayleigh number (Lipsev et al. 2016) which is defined as:

$$Ra = \frac{K\beta\rho^2c_{pf}gH\Delta T}{\mu\lambda}, \quad (2.18)$$

where Ra is the Rayleigh number, β is the volumetric thermal expansion coefficient ($^{\circ}\text{C}^{-1}$), H is the thickness of the aquifer (m), ΔT is the temperature difference across layer ($^{\circ}\text{C}$).

Palaeoclimatic history

Long-term climatic change can affect the underground temperature field. Because rock thermal diffusivity is very low ($1 \times 10^{-6} \text{ m}^2/\text{s}$), any temperature perturbation on the surface will slowly transmit downward (Kohl 1998). Such perturbations penetrate into the underground depending on the frequency of the temperature signal: a few meters for the annual cycle and about 80 m for a one-hundred-year cycle. In a typical well of 600 m deep, the temperature record of the subsurface contains not only the near-date warming event but also temperature history until to the last few hundred years. As the subsurface temperature is commonly measured in boreholes, especially in shallow boreholes (< 500 m), to determine geothermal gradient, which is later used for constructing a heat flow map. The transient signals are found to cause thermal anomalies in the determined heat fluxes (Hartmann and Rath 2005). Golovanova et al. (2014) observed a clear reduction in geothermal flux over depths of around 1000 m or more as a result of paleoclimate, notably due to the last glacial maximum and the little ice age. Therefore, the flux map often requires to be corrected for the paleoclimatic effect.

Topographic effect

The geothermal heat flux across the Earth's surface is only spatially uniform at a large scale. For smaller scales, the surface topography causes lateral variations in surface heat flow by distorting the parallel isothermals. The most manifest topographic effect on subsurface temperature distribution is the compressed isotherms within valleys (e.g., thermal anomalies) and reduced gradient beneath topographic rises. The magnitude of such effect depends primarily on the topographic relief (i.e., the

difference between the highest and lowest elevations) (Colgan et al. 2021). van der Veen et al. (2007) estimated that the local geothermal heat flux could double in deeply incised valleys beneath the Greenland ice sheet by considering the topographic effect. Similar to how it impacts the geothermal gradient distribution directly, the greater relief such as mountainous terrain can cause an enhanced vertical component of groundwater flow which in turn enhances the advective disturbance of the thermal field. Furthermore, when the ridges and valleys are closely spaced, large-amplitude and short-wavelength due to restrictions for development in lateral directions (Forster and Smith 1989).

2.2 Heat transfer in the wellbore

In a general case, a geothermal wellbore consists of pipe flow (flow inside the drilling or production string), the tubing wall, the annulus between the tubing and casing, the casing wall, and cement. Although this thesis focuses on wellbores in a drilling context, the heat transfer processes in most practical situations such as injection and production wells, or multiple borehole systems such as ground heat exchangers are the same. During the drilling phase (e.g., fluid injection and circulation), the governing heat transfer mechanism can be different at different borehole regions. Namely, the heat transfer in the wellbore includes the forced convection between the flow and inner tubing, the thermal conduction in the tubing wall, the forced or natural convection and radiation in the annulus, and the thermal conduction in the casing wall and cement. As the thermal conduction process in the fluid and the solid structures is already introduced in the previous part, only the heat transfer within the pipe flow and the annulus is briefly discussed.

2.2.1 Physical processes

Convection

Similar to the convective heat transfer mechanisms in the formation, two types of convective-flow induced heat transfer also exist at the borehole scale: forced convection and free convection (Figure 2.2).

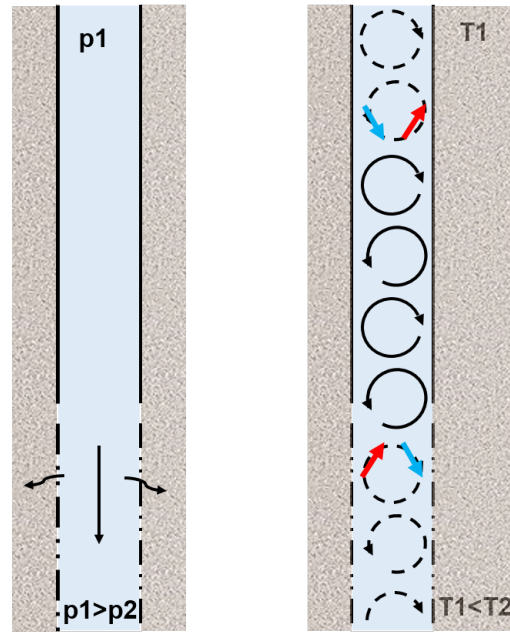


Figure 2.2: Schematic illustration of forced convective flow due to a hydraulic gradient (left) and free convective flow due to a temperature gradient (right) in boreholes (p : pressure, T : Temperature). After Berthold (2010).

Convection in the borehole is referred to as forced when the fluid is driven by external forces such as pumps. Such flow can be inside the string pipe and the annulus or both at the same time. Convection is considered to be a much more efficient way of heat exchange compared to heat conduction. It occurs as the result of the moving fluid passing by the solid surface (e.g., tubing wall) and exchanging the carried heat with the surface. Due to the lateral heat flow, the surrounding formation is eventually cooled down or heated up which thereby fulfills the process of geothermal energy extraction from underground. The heat flux can be calculated according to Newton's law of cooling, which is:

$$q = h(T_s - T_f), \quad (2.19)$$

where T_s and T_f are the temperature of the tubing wall and borehole fluid temperature, respectively, h is the heat transfer coefficient which depends on the fluid physical properties, flow regimes, and geometry of the solid surface and also the state of the fluid (single phase or gas-liquid phase). Herein, only single-phase fluid flow is investigated. The details for the determination of h can be found in Chapter 3.

Free convection in the borehole is generated by density differences in the fluid due to temperature gradients. It can be evidenced by detecting oscillations on the temperature log using a high-resolution logging tool (Diment 1967; Pfister and Rybach 1995). The presence of convection cells adds noise to the temperature measurements, causing temperatures to deviate from natural temperatures of the formation. Thus noise can be a

limiting factor for an accurate determination of the geothermal gradient. Furthermore, the significance of the noise is found to depend on the depths of the borehole. Diment (1967) measured temperatures in a static water column as a function of time and depth in a 340 m deep borehole. They found the amplitudes of temperature oscillations won't exceed 0.05 °C. Kutasov and Devyatkin (1973) applied a thermal modeling approach to examine the possible temperature disturbance caused by free convection in boreholes with typical diameters ranging from 8 to 10 cm. Their conclusion is consistent with the finding of Diment (1967) that the thermal disturbances in deep boreholes (>20 m) do not exceed 0.01-0.05 °C. Such disturbances are usually still within the resolution of the temperature logging instruments. However, in shallower boreholes (< 20 m), the effect of thermal convection is found to be more pronounced (thermal disturbance up to 3-5 °C). In a later study, a method for the justification of the occurrence of free convection in a borehole will be presented (see Chapter 3.2.3).

Radiation

Radiation usually occurs in the annulus when it is filled with gas, and it is the only heat transfer mechanism that requires no medium. The influence of radiation is dependent on the heat diffusion of the external tubing and the heat absorption of the inner casing. A general engineering approach to quantify the radiation energy is by calculating an equivalent radiative heat transfer coefficient, h_{ra} , according to the Stefan-Boltzmann Law:

$$h_{ra} = \frac{\sigma (T_{to}^2 + T_{ci}^2) (T_{to} + T_{ci})}{\frac{1}{\varepsilon_{to}} + \frac{r_{to}}{r_{ci}} \left(\frac{1}{\varepsilon_{ci} - 1} \right)}, \quad (2.20)$$

where T represents the absolute temperature (K), σ is the Stefan-Boltzmann constant which is $5.67 \times 10^{-8} \text{ W m}^{-2} \text{ K}^{-4}$, ε is the emissivity [-], r represents the radius, the subscript to and ci denote the outer tubing and inner casing respectively.

2.2.2 Analytical solutions for borehole temperature distribution

Ramey's analytical solution

Most of the literature on wellbore heat transfer is based on the classical work by Ramey Jr et al. (1962). A simple physical model that describes the wellbore heat transmission consists of fluid flow in a straight, non-cased borehole that is embedded in the two-dimensional formation. It is assumed that heat flux is only in the radial direction, and heat transfer from borehole to the formation is rapid compared to that in the formation, thus can be considered as in steady state. In addition, physical and thermal properties of the formation and fluids are constant. The derivation of the conservation equations can be found in Ramey Jr et al. (1962). Here, the solutions are briefly introduced and discussed.

For the injection case, the solution of temperature distribution in the well is given by:

$$T(z) = T_0 + \alpha z - \alpha A + (T_{in} - T_0 + \alpha A)e^{-\frac{z}{A}}, \quad (2.21)$$

where z is the depth, T_{in} is the injection temperature, T_0 is the surface temperature, α is the geothermal gradient, A is defined by:

$$A = \frac{\dot{m}c_p f(t_D)}{2\pi\lambda_s}, \quad (2.22)$$

where \dot{m} is the mass flow, $f(t_D)$ is the so-called dimensionless time function which represents the transient heat transfer from the borehole to the formation, t_D is defined as $\lambda_s t / (\rho_s c_{p_s} r_{wb}^2)$, where λ_s is the thermal conductivity of rock, ρ_s is the rock density, c_{p_s} is the specific heat capacity of rock, r_{wb} is wellbore radius.

According to Ramey and Sanyal (1981), temperature in a production well is calculated by:

$$T(z) = (T_{bh} - \alpha z) + \alpha A(1 - e^{-\frac{z}{A}}) + (T_s - T_{bh})e^{-\frac{z}{A}} \quad (2.23)$$

The time function $f(t_D)$ in Eq 2.21 and Eq 2.23 can be derived from solutions for radial heat conduction in the semi-infinite cylinder. Such solutions have been presented in many texts (Jaeger and Carslaw 1959; Buntebarth 2012). Different types of boundary conditions have been applied at the interface between borehole and formation, namely,

constant heat-flux line source, cylindrical source losing heat at constant temperature or radiation or convective flux. Solutions of all conditions have been presented both graphically and analytically (Jaeger and Carslaw 1959; Fontanilla 1980; Hellstrom 1992). These solutions converge to the same line and the convergence time is on the order of one week, at which temperature is controlled by formation conditions for many reservoir problems. However, for the early-stage transient periods, the solutions can be very different.

Ramey adopted an approximation for the constant heat-flux line source solution that works for a time greater than one week. However, such a solution can produce large errors for very early predictions. A number of studies have attempted to improve Ramey's solution and derive more efficient and stable approximations to small, medium, and large-time solutions for wellbore heat transmission problems by giving their specific expressions for $f(t_D)$ (Kutasov 1987, 2003; Wu and Pruess 1990; Kutun et al. 2014, 2015). In this work, the temperature distribution of the wellbore-formation is solved numerically using an in-house numerical tool (Korzani et al. 2019). To validate the simulation code, the numerical simulation results are compared with the analytical solutions given in Eq 2.21 and Eq 2.23. The simplified expression for $f(t_D)$ given by Kutun et al. (2015), based on the best curve fit of Ramey's dimensionless time function data, is applied:

$$T(z) = \ln(1 + 1.7\sqrt{t_D}) \quad (2.24)$$

The injection and production cases were modeled by considering three different scenarios: (1) water being injected at the same temperature as the surface temperature; (2) water being injected at a higher temperature than the surface temperature; (3) water being extracted from the reservoir. The model is set up in the cylindrical coordinate, the geometry and thermal properties data used in the simulations are the same as defined in Table 3.2 (Chapter 3), except that the well with 0.15 m radius is simplified as one-dimensional.

Figure 2.3 presents a comparison of temperatures obtained from analytical solutions given by Ramey and the numerical model. Maximum temperature differences (errors) for the three different simulations on day one, day five and day ten, respectively. Case (1): $|\Delta T|_{max} \leq 1.9$ °C, case (2): $|\Delta T|_{max} \leq 0.21$ °C, and case (3): $|\Delta T|_{max} \leq 1.9$ °C. It can be seen that the analytical and the numerical solutions match well. The difference between the solutions decreases as the simulation time increases. This can be due to that the applied time-function is less accurate for a shorter simulation time.

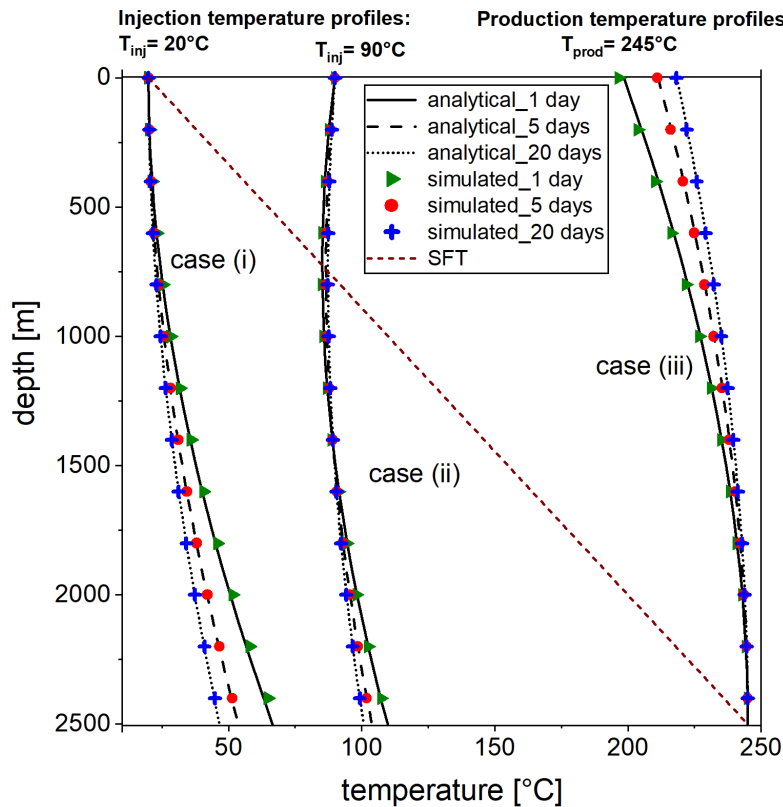


Figure 2.3: Comparison of analytical and simulated solution of Ramey's heat transmission model: case (1) and case (2) are the injection scenarios, where injection temperatures at well-head are 20°C and 90°C , respectively; case (3) is the production scenario: fluid is produced from bottom-hole at 245°C reservoir temperature. The analytical solution was plotted in lines: solid lines (one day), dash-dot lines (5 days), and dot lines (20 days). The simulated solution was marked in symbols: green crosses (one day), red circle (5 days), diamonds with lower half black (20 days). Wang et al. (2019).

As seen in Figure 2.3, for the three cases, the temperature profile after the shortest injection (production) time, which is one day, shows more curvature compared to profiles of the later times. This is due to the stronger effect of heat gain or loss at the earlier time since as the injected (or produced) gradually cools down or heats up the formation, the thermal contrast between the borehole fluid and the surrounding decreases with time. It can also be seen that the cooling or heating rate decreases with time, and the temperatures at depths along the borehole will finally converge to the injection temperature at the well-head (or the temperature at the bottom-hole inlet).

Ramey's model, also referred to as the line source model, has been adopted to solve a wide range of heat transfer problems for geothermal applications, such as calculation of thermal energy extraction from wells (Nian and Cheng 2018), prediction of undisturbed formation temperature (Chapter 2.3), thermal response test of borehole

heat exchanger (BHE) (Wagner and Clauser 2005). However, due to the intrinsic assumptions of this model, its limitations in practical engineering applications have also been reported. One is related to the steady-state heat transfer from the borehole to the formation. Such an assumption is not realistic for early-stage borehole conditions because the heat transport can be highly dynamic within some minutes to hours, and the thermal storage effect of wellbore completions needs to be taken into account (Bahonar et al. 2011). Sass and Lehr (2011) pointed out that exclusively radial heat flux is not valid for most BHEs due to the disturbing axial heat flux and that a cylindrical source boundary should be used instead. They concluded that an acceptable level of error with the linear source model can only be achieved for a BHE with a length-to-width ratio greater than 1000:1.

The coaxial flow model

Ramey's model has only considered downward flow, however, during the drilling process of a well, a coaxial contour flow can be more general as the mud is often circulated to bring the drilling cuttings back to the surface. During circulation, the drilling mud flows downwards (axial direction) in the drill pipe. The heat exchange process of the system involves two mechanisms: convective heat transport and heat transfer of the drilling mud with the pipe wall (forced convection heat transfer). At the bottom, fluid exited through the drill bit into the annulus. The temperatures at the outlet of the drill pipe and the inlet of the annulus are considered to be the same. The fluid in the annulus moves upwards to the surface. The annulus fluid temperature is controlled by the rate of convective heat transport and forced convection heat transfer at two fluid-solid interfaces: annulus fluid/outer drill pipe wall, annulus fluid/wellbore wall. Bobok and Szarka (2012) derived analytical solutions to predict the temperature distribution of the fluid both in the drilling pipe and in the annulus for the circulation scenario. In his model, drilling fluid is considered steady and incompressible and conductive heat flux in the fluid is negligible in the axial direction. The forced convective transfer at the pipe and casing wall is considered in the model. The fluid temperature inside the drill pipe can be calculated according to:

$$T(D) = C_1 e^{N_1 z} + C_2 e^{N_2 z} + T_0 + \alpha z - B\alpha, \quad (2.25)$$

The annulus fluid temperature is given by:

$$T_A = C_1(1 + BN_1)e^{N_1z} + C_2(1 + BN_2)e^{N_2z} + T_0 + \alpha z, \quad (2.26)$$

$$A' = \frac{\dot{m}(\lambda_s + r_{Ci}U_{Ci}f(t))}{2\pi r_{Ci}U_{Ci}\lambda_s} \quad \text{and} \quad B = \frac{\dot{m}}{2\pi r_{Di}U_{Di}} \quad (2.27)$$

$$N_1 = \frac{1}{2A'} \left(1 + \sqrt{1 + \frac{A'}{B}} \right) \quad \text{and} \quad N_2 = \frac{1}{2A'} \left(1 - \sqrt{1 + \frac{A'}{B}} \right), \quad (2.28)$$

$$C_1 = \frac{D_1}{D} \quad \text{and} \quad C_2 = \frac{D_2}{D} \quad (2.29)$$

$$D = N_2e^{N_2H} - N_1e^{N_1H}$$

$$D_1 = N_2(T_{in} - T_0 + B\alpha)e^{N_2H} + \alpha \quad (2.30)$$

$$D_2 = -N_1(T_{in} - T_0 + B\alpha)e^{N_1H} - \alpha$$

where T_{in} is the injection temperature in the drill pipe, H is the whole depth of the borehole, U represents the overall heat transfer coefficient, the subscript Di and Ci represents the inner surface of the drill pipe and the casing.

The above analytical solution is then also used for the numerical validation of the mud circulation model. The model size was 4600 m in the axial direction and 50 m in the radial direction. The mesh was discretized in 15 m steps in the axial direction and mesh sizes in the radial direction ranged between 10^{-3} m and 6.5 m. The geometric parameters of the wellbore and thermal properties data used in the modeling are given in Table 2.1. The comparison of the analytical solution and the simulated solution of the drill pipe fluid and annulus temperature is shown in Figure 2.4. Maximum estimation differences for the temperature of drill pipe fluid and annulus fluid are calculated, respectively: 0.72 °C, 1.06 °C after 4 days circulation; 0.32 °C, 0.51 °C after 10 days circulation; 0.08 °C, 0.17 °C after 20 days circulation. Again, the predictions from the numerical and the analytical models are minor.

According to Figure 2.4, the temperature of the downward flow in the drill pipe increases with depth. As the flow exits the drill bit and turns upward, the temperature continues to rise until it reaches a maximum. The depth at which the maximum temperature occurs hardly seems to change over the course of 20 days. Above this

depth, the temperature of the up-flow decreases and approaches the temperature of the down-flow with increasing time.

Property	Unit	Value
Formation temperature at the surface	°C	7
The geothermal gradient	°C/m	0.1
Casing, Cement and Formation thermal conductivity	W/(m°C)	50, 1.2, 1.5
Formation rock density	kg/(m ⁻³)	3000
Formation specific heat capacity	J/(kg°C)	840
Well depth	m	4600
Inside radius of the drill pipe	m	0.0352
The outside radius of the drill pipe	m	0.0445
Inside radius of the casing	m	0.0797
The outside radius of the casing	m	0.089
The radius of the wellbore/formation interface	m	0.1
Mass flow rate (\dot{m})	kg/s	15
Water injection temperature (T_{inj})	°C	20
Water density	kg/(m ⁻³)	1000
Water specific heat capacity	J/(kg°C)	4194
Water viscosity	Pa·s	1e-3
Water thermal conductivity	W/(m°C)	0.6

Table 2.1: Geometric parameters and material properties used in the simulation of the counter-flow heat exchange model.

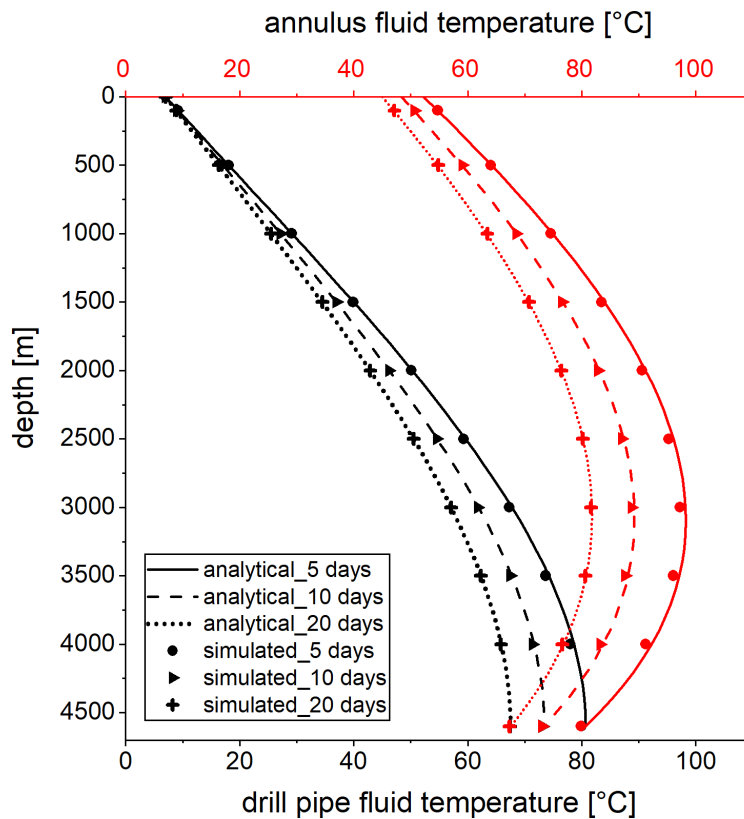


Figure 2.4: Comparison of analytical solution and simulated solution for the counterflow heat exchange model. The black color represents the temperature of the fluid inside the drill pipe, and the red color represents the temperature of the annulus fluid. Solutions were calculated and compared at three different circulation times: 5 days, 10 days, 20 days. The analytical solution was plotted in lines: solid lines (5 days), dash-dot lines (10 days), and dot lines (20 days). The simulated solution was marked in symbols: circles (5 days), squares (10 days), crosses (20 days) Wang et al. (2019).

2.3 Static formation temperature estimation using borehole temperature data

As already mentioned in the previous chapter, the distribution of subsurface temperature can be strongly influenced by several natural processes. Temperature measurements from boreholes provide the opportunity to quantify these processes by interpreting their characteristic thermal responses. However, the drilling of boreholes (i.e., fluid circulation) introduces transient perturbation to the temperature field around the wellbore region. This is primarily due to the temperature difference between the rock and the drilling mud, which creates large thermal contrast and thereby significant heat exchange between them. Other sources of thermal disturbances are related to

the specific drilling methods, they can be related to the frictional heating caused by the drilling bit for most drilling methods, the direct heat injection at the bottom-hole, and the heat generated by motors, etc (Clow 2008). Since the formation rock has low thermal diffusivity, the perturbations will take time to dissipate before the formation temperature obtain its equilibrium or the initial state. This often requires a long shut-in time of the borehole, which can be several weeks or months, which is often not possible due to commercial and regulatory aspects of the drilling operation. Instead, temperatures are often measured relatively short time after drilling stops and therefore need to be corrected to infer the true SFT. Since the past half-century or more, numerous research works have been engaged in reconstructing the SFT from perturbed borehole temperature data.

2.3.1 The line-source model

The first class of methods is developed based on the classical line-source model to represent the drilling and shut-in processes (Bullard 1947). These methods are referred to as the Horner type due to their analogy to a method proposed by Horner (1951) for analyzing pressure buildup data to obtain the well static pressure. Dowdle et al. (1975) first justified the conditions for applying the Horner temperature plot method. Štulc (1995) extended the method's applicability to discontinuous drilling situations, which are rather commonly encountered in real practice.

The physical model for the line-source method treats the well as an infinitely long heat source with no cross-section. During drilling and shut-in time, the well extracts heat at a constant rate, q , from the formation (a homogeneous, isotropic, and infinite medium). Under radial conditions, the mathematical model has the following form:

$$\frac{\partial^2 T}{\partial r^2} + \left(\frac{1}{r}\right) \frac{\partial T}{\partial r} = \left(\frac{\rho_s c_{ps}}{\lambda_s}\right) \left(\frac{\partial T}{\partial t}\right), \quad (2.31)$$

The solution of the model can be expressed as:

$$T_{bh} = T_{ls} + m_{ls} \ln\left(\frac{t_c + t_s}{t_s}\right) \quad (2.32)$$

where t_s and t_c are the shut-in time and the circulation time before circulation stop, respectively. $(t_c + t_s)/t_s$ is called the dimensionless Horner time. m is the slope.

T_{bh} are the BHT measurements, T_{ls} is the temperature when shut-in time approaches infinity, which is essentially the SFT.

The validity of the line-source model for geothermal applications has been under long debate due to its inherent assumptions, such as negligible radial geometry of the borehole, and constant heat flow, which is only in the radial direction. It has been found that the line-source model tends to yield underestimated SFT using early shut-in temperature measurements (Roux et al. 1980; Kutasov and Eppelbaum 2005). Furthermore, a consistent finding confirmed by Dowdle et al. (1975); Luheshi (1983); Shen and Beck (1986) is that the solutions of the line-source type methods are more accurate for long shut-in times when the thermal recovery process is insensitive to the details of the drilling process, the size of the borehole, and the thermal property differences between the formation and the borehole fluid.

The optimal duration of the shut-in is still controversial since the borehole size and thermal contrast between the borehole and the formation are case-dependent. Drury (1984) and Clow (2015) proposed shut-in times to be at least 2–5 times the circulation period. However, it should be noted that longer shut-in times can cause the drilling cost to increase significantly and thus become unfeasible for real practices. Nevertheless, the line-source model is still a practical tool to evaluate the SFT due to its simplicity and has been still extensively applied in both petroleum and geothermal applications.

2.3.2 The spherical-radial heat-flow model

The spherical-radial heat-flow model was put forward by Ascencio et al. (1994) who argued that during the drilling, heat flows more in a spherical-radial manner than in a strictly horizontal radial form at the bottom-hole (BH). The model assumes a thermally perturbed zone around the BH to be a sphere of radius R , and the formation is infinite, homogeneous, and isotropic with constant thermo-physical properties. By neglecting the convective heat flow, the governing equation of the model can be written as:

$$\frac{\partial^2 T}{\partial r^2} + \left(\frac{2}{r}\right) \frac{\partial T}{\partial r} = \left(\frac{\rho_s c_{p_s}}{\lambda_s}\right) \left(\frac{\partial T}{\partial t}\right), \quad (2.33)$$

The solution at the center of the sphere (where the BHT is measured) is approximated by:

$$T_{bh} = T_{sr} + m_{sr} \ln \left(\frac{1}{\sqrt{t_s}} \right), \quad (2.34)$$

It can be noticed that this method does not require the circulation time, the SFT, i.e., T_{sr} , is where the straight line that depicts BHTs against the time function $1/\sqrt{t_s}$ intercepts with the vertical axis (i.e., $t_s \rightarrow \infty$). In their another contribution, Ascencio et al. (1997) discussed the criteria for a successful application of such a model, namely,

$$t_s > \frac{2\pi m_{sr}^2}{T_{sr} - T_f}, \quad (2.35)$$

and

$$T_{bh} > T_{sr} - 0.4(T_{sr} - T_f), \quad (2.36)$$

where T_f is the mud circulation temperature. In addition, it was emphasized that the spherical-radial heat-flow model should only be applied at the BH. At other depths, a cylindrical-radial heat-flow model is more suitable.

2.3.3 The cylindrical heat-source method

The cylindrical heat-source models were developed to improve the prediction of the borehole temperatures for the short shut-in times. First models of this type, like the other two types of models, don't differentiate the thermal properties of the fluid inside the borehole and the surrounding structures (e.g., casing program and formation) (Middleton 1979; Leblanc et al. 1981). These models are later improved by several other works by taking into account the property contrast between the drilling fluid and the formation and different types of boundary conditions to approach the effects of fluid circulation. For instance, Lee (1982) and Luheshi (1983) both considered the constant temperature of the drilling fluid, which is an appropriate simplification for a rapid mud circulation case. Shen and Beck (1986) additionally discussed the constant heat-flux boundary condition for cases where flow in the borehole is slow and incorporated the thermal diffusivity of the borehole fluid in the model. Hasan and Kabir (1994) presented so far one of the most realistic analytical models which simulates the transient heat transfer processes that occur during the drilling operation by including the convective heat flux boundary condition at the borehole wall following Newton's law of cooling. The equation of the fluid temperature during

shut-in is given by,

$$\frac{dT_f}{dt} = - \left(\frac{2\pi}{\dot{m}c_{pf}} \right) \left(\frac{r_w U \lambda_s}{\lambda_s + r U T_D} \right) (T_f - T_{chs}), \quad (2.37)$$

where T_f is the fluid temperature at the borehole center, U is the overall heat-transfer coefficient that accounts for the convective heat transfer at the borehole wall, the conductive transfer within the solid components of wellbore (casing and cement), r is the radius of the borehole, \dot{m} is the mass flow rate of the drilling mud, T_{chs} represents the SFT, and T_D is the dimensionless temperature which is given by:

$$T_D = \begin{cases} 1.1282\sqrt{t_D}(1 - 0.3\sqrt{t_D}), & \text{if } t_D < 1.5 \\ (0.4063 + 0.5\ln t_D) \left(1 + \frac{0.6}{t_D}\right), & \text{if } t_D > 1.5 \end{cases}, \quad (2.38)$$

where t_D is the dimensionless time for the circulation defined as $\frac{\lambda_s t_c}{\rho_s c_{ps} r^2}$. Hasan and Kabir (1994) proposed the final equation for calculating the bottom-hole temperature after dimensionless time (t_D) elapsed after circulation stops is

$$T_{bh} = T_{CHS} + m_{chs} F(t_D), \quad (2.39)$$

Similar to the other methods, the SFT can be extrapolated using the plot of T_{bh} against the time function F (Hasan and Kabir 1994, for details).

Chapter 3

Temperature log simulations in high-enthalpy boreholes

This part is reproduced from the manuscript that has been published in the journal of *Geothermal Energy*.

Jia W., Fabian N., Maziar G. K., Thomas K. [2019]: Temperature log simulations in high-enthalpy boreholes; *Geothermal Energy* (7), 1-21

Abstract

Temperature logs have important applications in the geothermal industry such as the estimation of the static formation temperature (SFT) and the characterization of fluid loss from a borehole. However, the temperature distribution of the wellbore relies on various factors such as wellbore flow conditions, fluid losses, well layout, heat transfer mechanics within the fluid as well as between the wellbore and the surrounding rock formation, etc. In this context, a numerical simulation approach is applied to investigate the influencing parameters/uncertainties in the interpretation of borehole logging data. To this end, synthetic temperature logs representing different well operation conditions were numerically using our in-house wellbore simulator. Our models account for several complex operation scenarios resulting from the requirements of high-enthalpy wells where different flow conditions, such as mud injection with- and without fluid loss and shut-in, occur in the drill string and the annulus. The simulation results reveal that free convective heat transfer plays an important role in the earlier evolution of the shut-in-time temperature; high accuracy SFT estimation is only possible when long-term shut-in measurements are used. Two

other simulation scenarios for a well under injection conditions show that applying simple temperature correction methods on the non-shut-in temperature data could lead to large errors for SFT estimation even at very low injection flow rates. Furthermore, the magnitude of the temperature gradient increase depends on the flow rate, the percentage of fluid loss and the lateral heat transfer between the fluid and the rock formation. As indicated by this study, under low fluid losses (< 30%) or relatively higher flow rates (> 20 L/s), the impact of flow rate and the lateral heat transfer on the temperature gradient increase can be ignored. These results provide insights on the key factors influencing the well temperature distribution, which are important for the choice of the drilling data to estimate SFT and the design of the inverse modeling scheme in future studies to determine an accurate SFT profile for the high-enthalpy geothermal environment.

3.1 Introduction

Geothermal explorations depend strongly on reservoir conditions which are evaluated by increasingly sophisticated reservoir simulators (Cacace et al. 2010; O'Sullivan and O'Sullivan 2016; Konrad et al. 2019). Also, data acquisition, mostly of seismic data, has reached a high degree of complexity. This is however contrasted by little effort in the evaluation of logging data, especially of temperature logs. Usually, the primary objectives of running a temperature survey in a well are to obtain valuable information on geothermal reservoirs such as the static formation temperatures (SFT) and the location of fluid loss zones. This requires temperature logs measured at different stages (mud circulation and shut-in) during the evolution of the temperature in the borehole fluid-formation system as well as different interpretation techniques of these temperature logs (Witterholt et al. 1972).

The SFT is usually inferred from the measurement of bottom-hole temperature (BHT) when the drilling circulation has stopped and the borehole fluid temperature gradually develops towards the initial or unperturbed formation temperature. Due to the thermal disturbances caused by the drilling mud, the measured BHT is usually lower than the true SFT and needs to be corrected to obtain a reliable estimate (Deming 1989; Goutorbe et al. 2007). Various temperature correction methods based on different simplified physical models have been developed, e.g., the Horner-plot method (or constant line source method (Bullard 1947; Dowdle et al. 1975); the spherical and radial heat flow method (Ascencio et al. 1994, 2006); the Hasan-Kabir method (or

conductive-convective cylindrical heat source model (Hasan and Kabir 1994) and the Kutasov-Eppelbaum method (or generalized Horner method (Kutasov and Eppelbaum 2005)).

These methods are based on linear or non-linear regression models that describe the relationship between measured BHT and time functions (Verma et al. 2006*a,b*; Wong-Loya et al. 2012) accounting for the transient effects of thermal recovery during the shut-in phase of the borehole. The simplicities in these methods make them very prevalent engineering tools for estimating SFT.

Another important application of temperature logs is the identification of fluid loss or feed zones from temperature data obtained under hydraulic testing conditions. Examples of using temperature measurements in boreholes are multifold. Pehme et al. (2010) identified hydraulically active fractures in dolomite and sandstone aquifers; Klepikova et al. (2011) estimated local transmissivities and hydraulic head differences; Nian et al. (2015) predicted flow rates in oil and gas production wells. These authors stressed the satisfactory accuracy of temperature-derived flow velocities compared to direct flow measurement. In recent years, fiber-optic distributed temperature sensing (DTS), which is a robust means of acquiring continuous temperature profiles instantaneously along the length of the cable (Großwig et al. 1996), has also been extensively used to improve the accuracy of flow rate profiling and the detection of fracture zones (Read et al. 2013, 2015; Coleman et al. 2015; Bense et al. 2016).

In a high-temperature environment, the acquisition of logging data from exploration and drilling projects in geothermal fields is more challenging compared to its petroleum counterparts. In recent years, high-temperature geothermal systems have gained attention due to their large potential for energy extraction. In fact, a number of wells drilled in geothermal fields such as The Geysers (USA), Los Hornos (Mexico), Kakkonda (Japan), Larderello (Italy), and Reykjanes (Iceland) have been reported (Reinsch et al. 2017; Kruszewski and Wittig 2018) to even reach supercritical conditions for water ($T > 374$ °C, $P > 221$ bar). Reliable logging in such extreme well conditions is currently very challenging using conventional tools, which are normally rated up to 175 °C bottom-hole temperature (Baird et al. 1998). Although high temperature and pressure logging tools are available (Ikeuchi et al. 1998; Sekine et al. 2004; Reinsch et al. 2013), these tools are generally all restricted to specific operating conditions in harsh environments. For example, the electronic Kuster K10, a commonly used commercial tool in the industry, can operate at a maximum of 350 °C only up to 4 hours (Danielsen 2008). This short period may be sufficient for the tripping of the logging tools but not for collecting data to resolve the transient thermal response under shut-in condition. DTS, which is considered better suited for use at

elevated temperatures, gives erroneous temperature readings under high temperatures ($> 300\text{ }^{\circ}\text{C}$) due to the chemical and thermal degradation of the optical fiber (Reinsch et al. 2013; Laarossi et al. 2019). To keep the temperature of the measuring device below its maximum tolerance, cooling through continuous injection during logging is necessary for extreme high-temperature boreholes (Friðleifsson et al. 2020).

The present study focuses on the analysis of temperature logging data from high-temperature geothermal wells. It particularly addresses the specific conditions (e.g. drill pipe-and-annulus geometry and continuous injection) which result from the requirements of such an environment. Two sets of simulation examples are analyzed to reflect possible logging conditions in a high-enthalpy well. In the first example, fluid injection followed by shut-in is simulated. This example is used to examine the validity of applying simple BHT correction methods on the shut-in temperature data to estimate SFT, as well as to evaluate the impact of the free convection heat transfer in the build-up of borehole fluid temperature and the SFT estimation results. To the authors' knowledge, the later was hardly discussed in former wellbore simulation studies (Espinosa-Paredes et al. 2009; Yang et al. 2015). The second example investigates two new topics for high-temperature geothermal wells under-injection. One scope of the investigation is whether simple BHT type correction methods are still applicable to logging data from boreholes which are under continuous cooling due to the restriction of the logging tool. Furthermore, a new method is discussed to quantify the fluid loss percentage from temperature logs by computing the ratio of temperature gradient below and above the fluid loss point.

3.2 Methodology

3.2.1 Analytical approach

Herein, the Horner-plot method (HM) for SFT estimation using shut-in temperature logs is analyzed due to its wide application in the geothermal industry (Andaverde et al. 2005; Kutasov and Eppelbaum 2018). The evaluation of other SFT estimation methods falls outside the scope of this study but can be achieved following very

similar procedure according to their respective analytical models (Chapter 2). Recall the mathematical form of the HM:

$$T_{sh} = T_{hm} + \frac{q}{4\pi\lambda_s} \ln \frac{t_{cl} + t_{sh}}{t_{sh}}, \quad (3.1)$$

where T_{sh} is the borehole shut-in temperature, T_{hm} is the SFT, t_{sh} is the shut-in time, t_{cl} is the circulation time, q is the heat extraction rate. Following the standard procedure of HM method, the SFT is the yielded intercept of the line (shut-in temperatures against $(t_{cl} + t_{sh})/t_{sh}$) with the vertical axis on the semi-logarithmic plot.

3.2.2 Numerical Approach

An in-house numerical simulation tool is used to model the thermal behavior of the wellbore and its surrounding formation. The simulator is an application developed based on the MOOSE framework which provides a multiphysics object-oriented simulation environment (Gaston et al. 2009). MOOSE allows for efficient utilization of a wide range of computational hardware by using both shared-memory and distributed-memory parallelism (Gaston et al. 2013). The MOOSE based application consists of different physics modules which can be easily added, removed and coupled for solving variables in an implicit and fully coupled manner.

Figure 3.1 shows the schematic of typical wellbore flow and heat transfer scenarios. The cold drill fluid is considered to be either injected both in through the drill pipe and the annulus (coflow); or injected in the drill pipe and circulated back to the surface (counterflow). The simulator assumes the wellbore to be treated either as a one-dimensional or a two-dimensional structure depending on the problem being studied. When a two-dimensional wellbore structure is considered, the wellbore components, such as the fluid inside the drill pipe, the drill pipe wall, the annulus, and the casings, are treated as different regions (region 1, 2, 3, 4, respectively) in which the temperatures (T1, T2, T3, and T4) need to be solved as individual variables (Figure 3.1). These variables are linked through the interfacial heat transfer relationships between the fluid and the solid. The injection fluid was assumed to be pure liquid water. Fluid properties such as density, viscosity, and heat capacity were calculated according to the IAPWS-IF97 formulation (Cooper and Dooley 2007). The fundamental assumptions of the models considered in this work are: the geometries of the wellbore and formation are cylindrical, the fluid is incompressible, fluid flow

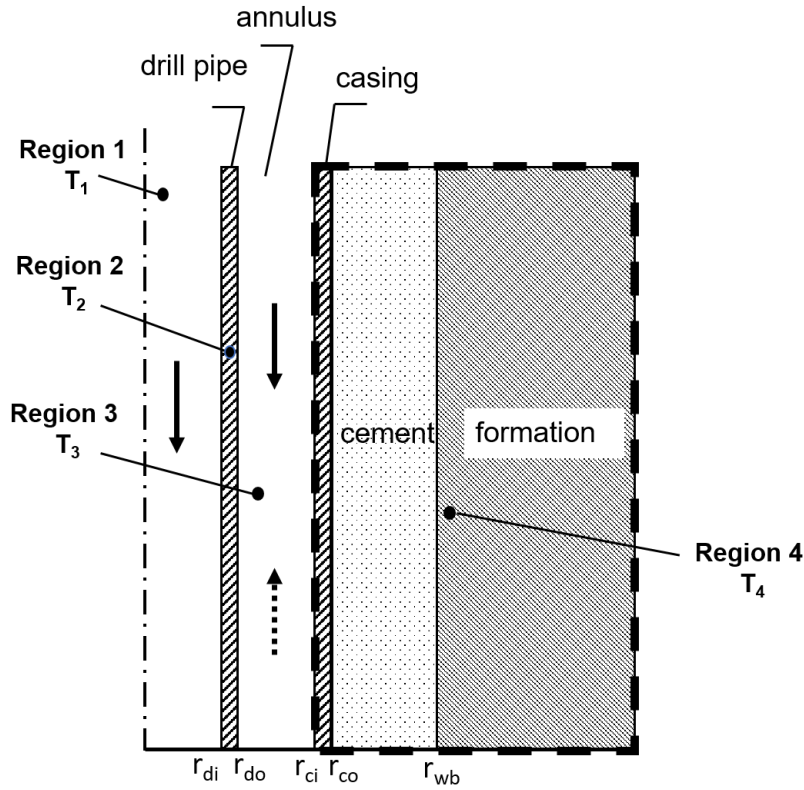


Figure 3.1: Schematic of the heat exchange model between the wellbore and the formation. Governing equations are solved in four regions: the fluid inside the drill pipe (Region 1), the drill pipe wall (Region 2), the annulus (Region 3), casing-cement-formation (Region 4). The solid arrow pointing downwards and the dashed arrow pointing upwards in the annulus refer to coflow and counterflow scenarios in the wellbore, respectively.

is in the axial direction only, the rock formation is impermeable, there is no radial temperature gradient within the fluid when the wellbore is considered to be a two-dimensional structure, thermal dissipation and expansion effects are negligible.

Making these assumptions, the energy conservation equation for the fluid inside the drill pipe and annulus is written in the following form:

$$\rho_f c_{p_f} \left(\frac{\partial T_f}{\partial t} + v_{rf} \frac{\partial T_f}{\partial r} + v_{zf} \frac{\partial T_f}{\partial z} \right) - \frac{\lambda_f}{r} \frac{\partial T_f}{\partial r} - \lambda_f \frac{\partial^2 T_f}{\partial r^2} - \lambda_f \frac{\partial^2 T_f}{\partial z^2} = 0. \quad (3.2)$$

The continuity equation for incompressible flow is given by:

$$\frac{1}{r} \frac{\partial (rv_{rf})}{\partial r} + \frac{\partial v_{zf}}{\partial z} = 0, \quad (3.3)$$

where ρ_f is the fluid density, c_{p_f} is the fluid specific heat capacity, v_z and v_r are the axial and radial flow velocities, respectively, λ_f is the thermal conductivity.

The energy conservation equation for the pipe wall, casing and formation can be expressed as:

$$\rho_s c_{p_s} \frac{\partial T_s}{\partial t} - \frac{\lambda_s}{r} \frac{\partial T_s}{\partial r} - \lambda_s \frac{\partial^2 T_s}{\partial r^2} - \lambda_s \frac{\partial^2 T_s}{\partial z^2} = 0, \quad (3.4)$$

where ρ_s , c_{p_s} , λ_s is the density, heat capacity and thermal conductivity of the pipe wall, casing and formation, respectively.

The final forms of the above governing equations for regions 1,2,3,4 (Figure 1) are simplified into:

$$\frac{\partial v_{zi}}{\partial z} = 0, i = 1, 3 \quad (3.5)$$

$$\rho_f c_p \left(\frac{\partial T_i}{\partial t} + v_{zi} \frac{\partial T_i}{\partial z} \right) - \frac{\lambda}{r} \frac{\partial T_i}{\partial r} - \lambda \frac{\partial^2 T_i}{\partial r^2} - \lambda \frac{\partial^2 T_i}{\partial z^2} = 0, i = 1, 3 \quad (3.6)$$

$$\rho_f c_p \frac{\partial T_i}{\partial t} - \frac{\lambda}{r} \frac{\partial T_i}{\partial r} - \lambda \frac{\partial^2 T_i}{\partial r^2} - \lambda \frac{\partial^2 T_i}{\partial z^2} = 0, i = 2, 4 \quad (3.7)$$

where i refers to the region number.

The initial and boundary conditions of the thermal-hydraulic models considered in this work are given in Table 3.1.

BC&IC	Expression	Description
IC	$T_i(r, z, t = 0) = T_f(r, z), i = 1, 2, 3, 4, \forall r, 0 \leq z \leq H$	The initial temperature is equal to the formation temperature
BC1	$v_{zi} = \frac{\dot{m}_i}{\rho A_i}, z = 0, i = 1, 3$	The velocity of the drill pipe fluid and the annulus fluid are calculated according to the mass flow rate at the wellhead
BC2	$q = -\lambda \left(\frac{\partial T}{\partial r} \right) \Big _{\Gamma_{ij}} = h(T_i - T_j),$ on $\Gamma_{12}, \Gamma_{23}, \Gamma_{34}$	Heat flux across the solid-fluid interface is determined by the heat transfer coefficient times the temperature difference between fluid and solid wall
BC3	$-\lambda \left(\frac{\partial T_1}{\partial r} \right) = 0$ at $z = H, z = 0$	No thermal gradient at the surface and bottom of the reservoir
BC4	$T_4(r = \infty, z, t) = T_f(r, z)$ at $r = \infty$	No thermal gradient at the surface and bottom of the reservoir
BC5	$T_1(r, z = 0, t) = T_{inj}$ at $0 < r < r_1, z = 0$	The temperature at the well-head equals the injection temperature
BC6	$T_1(z = H, t) = T_3(z = H, t)$	The fluid temperature of the drill pipe fluid and the annulus fluid at the bottom hole are equal. This is only validated for the counterflow scenario (mud circulation)

A_i is the flow cross-section, Γ_{ij} is the interfacial area between the fluid and solid structures, e.g., drill pipe, casing and formation, H is the well depth, $T_f(r, z)$ is the formation temperature, T_{inj} is the injection temperature of the fluid, h is the heat transfer coefficient.

Table 3.1: Boundary and initial conditions of the thermal-hydraulic models.

3.2.3 Heat transfer coefficients

As mentioned above, the thermal exchange between different wellbore regions is modeled via thermal transfer relations at their interfaces (Table 3.1, BC2). The heat transfer coefficient, h , is the proportionality constant between the heat flux and the thermodynamic driving force for the heat flow (i.e., the temperature difference between adjacent wellbore components, ΔT). In this work, the heat transfer coefficients under forced convection and shut-in condition are correlated and calculated using different approaches.

Forced convection

Under forced convection, the heat transfer coefficient is defined as (Yang et al., 2015):

$$h = \frac{Nu \cdot \lambda_f}{d}, \quad (3.8)$$

where Nu is the Nusselt number, d is the hydraulic diameter of the drill pipe and annulus.

For laminar flow inside the annulus, Nu is calculated using the Sieder-Tate correlation (Kohl et al., 2002) :

$$Nu = 1.86(RePr)^{1/3} \left(\frac{d}{L}\right)^{1/3} \left(\frac{\mu}{\mu_w}\right)^{0.14}, \text{ for } Re \leq 2300, \quad (3.9)$$

where L is the length of the tube, Pr is the Prandtl number, Re is the Reynolds number, μ is the dynamic viscosity of the bulk fluid, μ_w is the fluid viscosity at the temperature of the tube wall.

In the laminar regime inside the drill string:

$$Nu = 4.364, \text{ for } Re \leq 2300. \quad (3.10)$$

For highly turbulent flow, the Dittus-Boelter equation (Dittus and Boelter 1985) is applied:

$$Nu = 0.023 \cdot Re^{0.8} \cdot Pr^{0.3}, \text{ for } Re \geq 1e4. \quad (3.11)$$

For the transition between laminar and highly turbulent flow, the Nusselt number is estimated by the following linear interpolation (Diersch et al. 2011; Gnielinski 2013):

$$Nu = (1 - \gamma) \cdot 4.364 + \gamma \cdot 0.023 \cdot Re^{0.8} \cdot Pr^{0.3}, \text{ for } 2300 < Re < 1e4, \quad (3.12)$$

$$\text{with } \gamma = \frac{Re - 2300}{10^4 - 2300}.$$

Shut-in condition

So far in most theoretical and simulation studies, pure conductive heat flow in a static water column is assumed when estimating temperature recovery during borehole shut-in (Shen and Beck 1986; García et al. 1998; Espinosa-Paredes et al. 2001; Yang et al. 2015). The heat transfer coefficient in the borehole fluid is then approximated by:

$$h_c = \frac{\lambda_f}{r_{wb}}, \quad (3.13)$$

where r_{wb} is the borehole radius.

However, several studies have reported the existence of another key factor in the heat transfer, which is free convection caused by density differences arising from vertical temperature gradients (Diment 1967; Gretener 1967; Pfister and Rybach 1995; Berthold and Börner 2008; Klepikova et al. 2018). The critical parameters for the free convection process can be indicated by the following equation (Diment and Urban 1983):

$$\nabla T_{cr} = \frac{g \cdot \beta \cdot T_{abs}}{c_p} + \frac{C \cdot \nu \cdot \kappa}{g \cdot \beta \cdot r_{wb}^4}, \quad (3.14)$$

where ∇T_{cr} is the critical thermal gradient to initiate free convection, g is the acceleration due to gravity, β is the thermal expansion coefficient, T_{abs} is the absolute temperature (K), C_p is the specific heat capacity, C is a constant with a value of 216 for tubes, ν is the fluid kinematic viscosity, κ is the fluid thermal diffusivity. Taking the following values as typical for the borehole fluid: $\nu = 1e - 6 \text{ m}^2/\text{s}$, $\beta = 2e - 4 \text{ K}^{-1}$, $\kappa = 1.4306e - 7 \text{ m}^2/\text{s}$, $c_p = 4149 \text{ J}/(\text{kgK})$, absolute temperature range of 273.15–573.15 K. This equation reveals that for a borehole with a radius of 35~150 mm, the average critical thermal gradient needed to initiate free convection is 2.36e-4~1e-2 K/m.

Unlike forced convection, which normally acts only in the axial direction, free convection enhances the heat transfer in all directions through fluid circulation and mixing.

However, a well-established quantitative description of the thermal effect of free convection in boreholes is still missing, and a general modeling approach is not available. Luheshi (1983) showed that free convection does not significantly enhance vertical heat transfer. Since the radial temperature gradient is typically much larger, the contribution to heat flux in the vertical direction by free convection is considered negligible. However, he mentioned it might be necessary to account for the enhancement in radial heat flux due to the mixing effect of fluid motion induced by buoyancy forces. In our work, we have assumed the increase of the heat transfer rate due to free convection only acts in the radial direction. The overall heat transfer coefficient can be written as:

$$h = h_c + h_{free}, \quad (3.15)$$

which means that the heat transfer for the shut-in condition results from conduction and free convection.

In our models, the heat transfer coefficient for forced convection was calculated explicitly according to Equation (3.8-3.13). While for the shut-in condition, the heat transfer due to free convection was either neglected ($h_{free} = 0$) or was implicitly evaluated (e.g. h_{free} is a factor or fraction of h_c).

3.3 Simulation Scenarios

In the simulation studies, we began with the application of HM to the simulated shut-in temperature logs. Then we simulated two logging scenarios in a high-temperature environment. In one scenario, temperature logs obtained under continuous borehole cooling were used to estimate SFT and the sensitivity of the estimation error to different flow rates was investigated. In another scenario, temperature logs were used to quantify the fluid loss in the well.

3.3.1 Shut-in temperature logs simulation

The evaluation of the HM was conducted by numerical simulation of both the circulation and shut-in stage of well operation. In this model, fluid flow in a straight, non-cased two-dimensional well embedded in the two-dimensional formation was considered. The modeling parameters can be found in Table 3.2. The model domain size

of 2500 m in the axial direction and 50 m in the radial direction was chosen to reflect the reservoir depth and to ensure that the lateral outer boundary represents far-field conditions which were not affected by thermal perturbations from well operations. The FE mesh was discretized with 150 layers in the axial direction ($\Delta z = 16.7m$). In the radial direction, the mesh was refined near the well ($\Delta r_{min} = 10^{-3}m$) and coarsened at a larger lateral distance ($\Delta r_{max} = 4m$). The final mesh size was determined by performing a sensitivity analysis yielding asymptotic smaller variations for the calculated temperatures (maximum temperature variations of less than $10^{-2} \text{ }^\circ\text{C}$). The procedure mentioned above for determining the model domain, mesh sizes, etc., has been applied analogously to each of the models in this work.

Property	Unit	Value
Formation temperature at the surface	$^\circ\text{C}$	20
Bottom-hole temperature	$^\circ\text{C}$	245
Formation rock density	kg/m^3	2650
Formation thermal conductivity	$\text{W}/(\text{m}^\circ\text{C})$	2.92
Formation specific heat capacity	$\text{J}/(\text{kg}^\circ\text{C})$	1000
Well depth	m	2500
Well radius	m	0.15
Water injection rate (Q_{inj})	kg/s	20 (first 10 days); 0 (after 10 days)
Water injection temperature (T_{inj})	$^\circ\text{C}$	20
The geothermal gradient	$^\circ\text{C}/\text{m}$	0.09
Water specific heat capacity	$\text{J}/(\text{kg}^\circ\text{C})$	3160
Water thermal conductivity	$\text{W}/(\text{m}^\circ\text{C})$	0.6

Table 3.2: Geometry and material properties used in the modeling of circulation and shut-in.

The total simulation time was 150 days with 10 days being the cooling (injection) period followed by the shut-in period. The numerically predicted temperatures of borehole fluid during shut-in were used to estimate the SFT according to Equation 3.1. The rate of heat transfer during the shut-in period was controlled by the magnitude of the heat transfer coefficient in the model. In order to investigate the impact of free convection on the temperature recovery during shut-in, we considered different values of h_{free} : $0, h_c, 9h_c, \infty$. According to Equation 3.15, the heat transfer coefficients then became: (1) $h = h_c$; (2) $h = 2h_c$; (3) $h = 10h_c$; (4) $h = \infty$. Case (4) corresponds to the condition where the fluid acts as a perfect conductor and thermal resistance in the well does not exist.

3.3.2 High-temperature environment simulation

In this section, we focus on the simulation of temperature logs in a high-temperature environment. For this purpose, we have assumed the SFT to be in a temperature range from 5 °C (surface) to 500 °C (bottom-hole). Two different SFT profiles were analyzed. The profile was either linear-shaped which could be linked to a geothermal system controlled by pure heat conduction, or S-shaped representing commonly observed heat convection zones (Figure 3.2). The wellbore layout included the drill pipe, annulus and several casings (Table 3.3). The above described SFT profiles and wellbore layout were used in each of the following simulation cases.

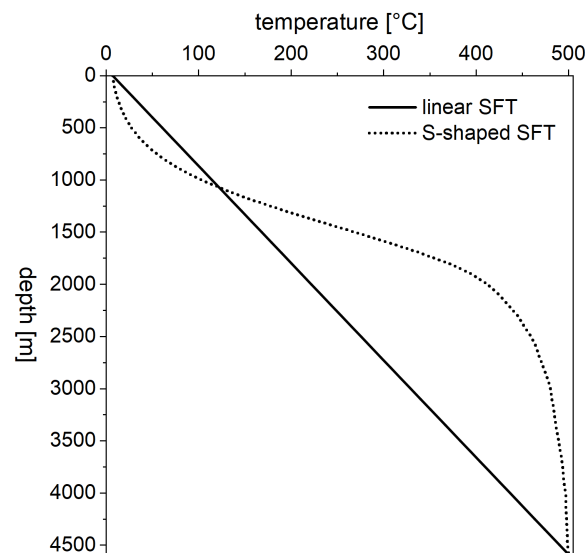


Figure 3.2: Two different SFT profiles assumed in the high-temperature environment simulations: linear SFT describes a pure heat conduction geothermal system, S-shaped SFT reflects typically occurring convection zones in the geothermal system.

Wellbore completion	Inner radius (m)	Outer radius (m)	Cross-sectional area (m ²)	Depth(m)
Drill pipe	0.0352	0.0445	2.33×10^{-3}	0-4589
Casing i	0.0797	0.0889	4.87×10^{-3}	0-1304
Casing ii	0.11	0.122	8.75×10^{-3}	0-2941
Casing iii	0.1577	0.1699	1.26×10^{-3}	0-793
Annulus	0.0445	0.0797	1.37×10^{-2}	0-1304
	0.0445	0.11	3.18×10^{-2}	1304-4589

Table 3.3: Geometrical extensions of the wellbore.

Continuous borehole cooling

The simulations assumed that cold water (7 °C) was injected for ten days both into the drill pipe and into the annulus at a flow rate of 15 L/s and 45 L/s, respectively (1st period). In the 2nd period (thermal recovery), injection into the drill pipe stopped while annulus injection continued but the flow rate was reduced to Q (Q ranged between 0-5 L/s). The borehole was under the full shut-in condition when Q was 0 L/s; otherwise, it was under partial shut-in condition. Temperatures of the fluid inside the drill pipe at different warm-up times were measured and then used to estimate SFT by applying the HM.

Fluid loss

The impact of fluid loss on the temperature response in a borehole is analyzed by generating a series of dynamic temperature logs based on forward simulations where different fluid loss amounts under different flow rates in the borehole were assumed. These temperature logs were used as samples for the analysis of the temperature response to the fluid loss in the borehole. Again cold water (7 °C) was injected through the drill pipe and the annulus separately, and the temperature logs were only 'recorded' in the drill pipe. For simplicity, the total amount of fluid being injected was distributed such that the flow velocities in the string and the annulus were equal. The fluid loss occurred at 3.35 km depth from the annulus through a hydraulic connection

to the formation. The total amount of injected fluid was varied from 5 L/s to 50 L/s. The percentage of fluid loss from the annulus was varied between 0% and 100%.

3.4 Results and Discussion

3.4.1 Estimating SFT using shut-in temperature logs

The evolutions of BHT with respect to time considering four different heat transfer rates are given in Figure 3.3.a. It is shown that the recovery of BHT is influenced by the heat transfer rate in the borehole during the early stage of shut-in. The higher the heat transfer rate is, the faster the temperature builds up. A maximum difference of 30 °C between the predicted BHTs is found. However, the four temperature curves have approximately the same build-up rate after 20 days. Furthermore, the sensitivity of temperature build-up on the heat transfer rate decreases when the heat transfer rate reaches $10h_c$. Figure 3.3.b shows the plots of the BHT against the Horner dimensionless time. For each curve, two different BHT data sets are used to estimate the SFT. One contains the early shut-in-time temperature data measured within one day ($t_s=12, 18, 24$ hr); another one contains long-term shut-in measurements of several days ($t_s=$ two, three, four days). The regression lines for the early and the long-term shut-in BHT measurements are plotted in Figure 3.4.a and Figure 3.4.b, respectively. Figure 3.4.c displays the comparison between the intercepts of these regression lines (SFT estimates) and the true SFT value. In all cases, the SFT is underestimated with a large error when early shut-in-time temperature data are used. The underestimation errors range from -61.9 °C to -31.3 °C depending on the rate of heat transfer assumed in the model. On the other hand, the accuracy for SFT estimation is improved when using long-term shut-in temperature data, and again, the influence of the heat transfer rate on SFT estimation is observed. The SFT tends to be overestimated under low heat transfer rates ($h = h_c, 2h_c$) and underestimated under higher heat transfer rates ($h = 10h_c, \infty$).

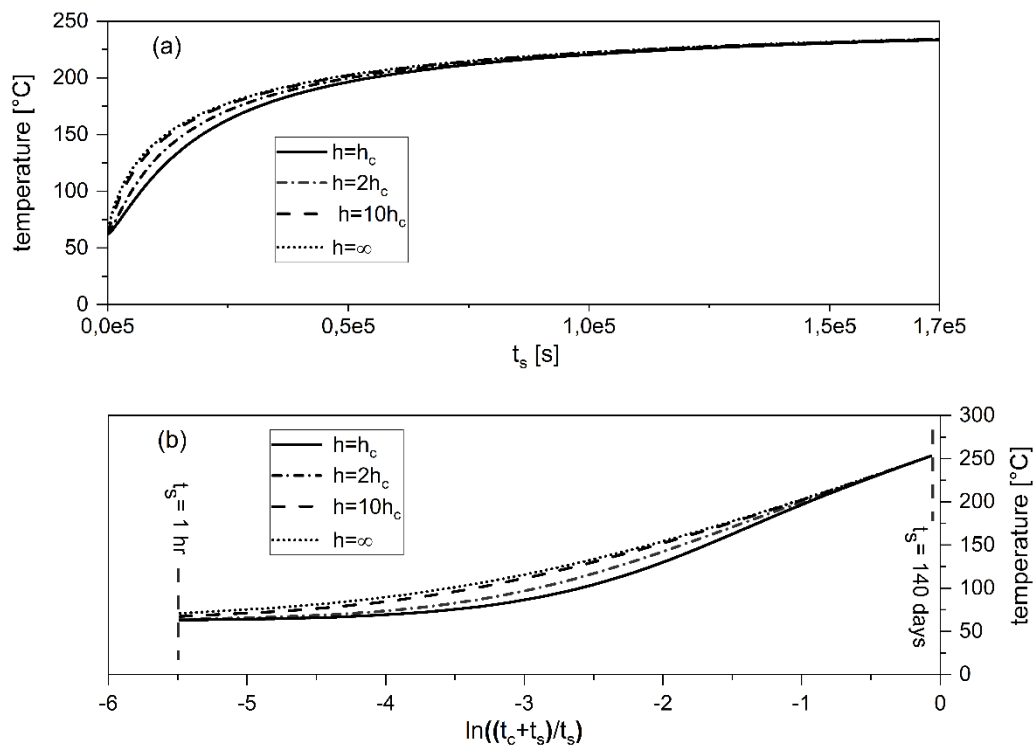


Figure 3.3: (a) The change of BHT within a shut-in period of 20 days under four different heat transfer coefficients (h) in the borehole. (b) The Horner-plots of the four temperature curves shown in (a) (the x-axis value is the opposite of the Horner dimensionless time (Equation 3.1), the minimum x-axis value of the temperature data on the curves corresponds to when $t_s = 1 \text{ hr}$, the maximum x-axis value corresponds to when $t_s = 140 \text{ days}$).

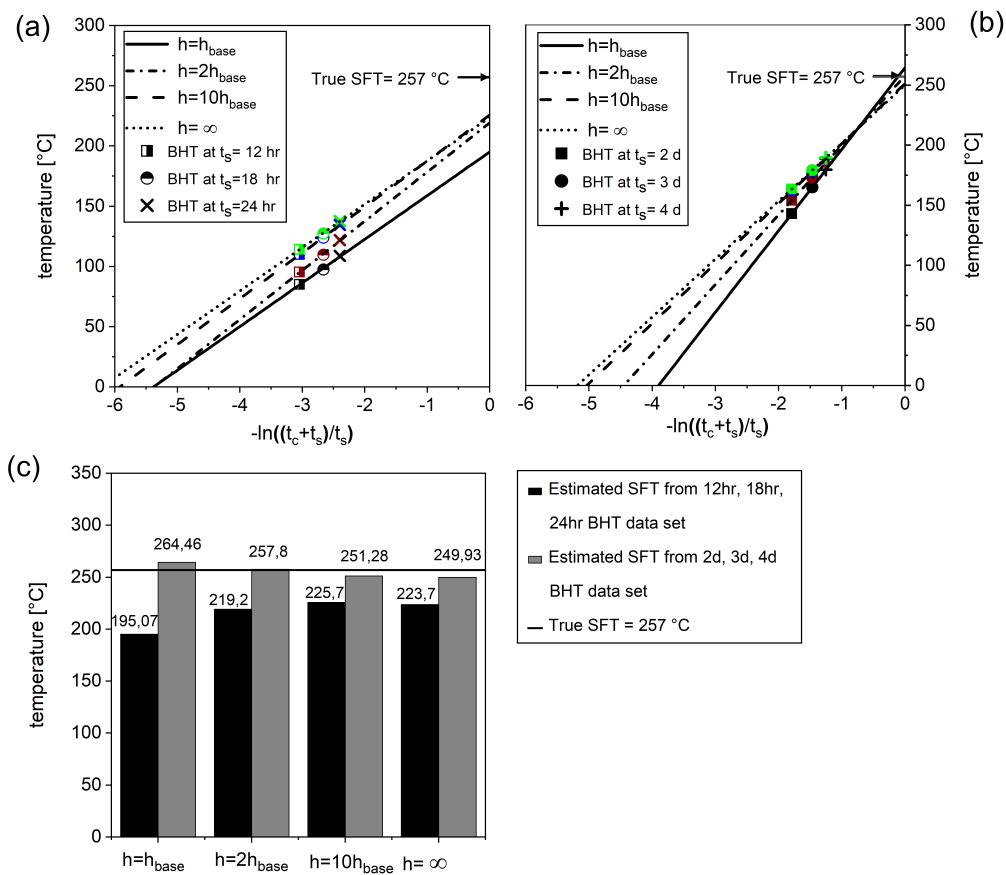


Figure 3.4: The HM plots (lines) using BHT measurements (markers) at (a) early shut-in time ($t_s=12, 18$ and 24 hours) and (b) long-term shut-in ($t_s=2, 3$, and 4 days) for each of the four different heat transfer coefficients (h) considered. (c) Comparison of the results of SFT estimation with the true SFT value: the black bars are the four SFT estimates using early shut-in time BHT data; the dark grey bars represent the four SFT estimates using long-term shut-in BHT data; the solid line stands for the referencing value which is the true SFT (257 °C).

3.4.2 Estimating the SFT using temperature logs obtained under borehole cooling

As shown earlier, both the heat transfer rate in the borehole and the measurement time have an impact on the final result of the estimated SFT. In the following SFT calculations, long-term shut-in temperature data measured after one day, two days and three days since the start of the 2^{nd} period were used. The heat transfer coefficient h for the full shut-in conditions was then calibrated by trial and error until an accurate SFT estimation was achieved (see Figure 3.5, shut-in case). The calibrated h was

examined to be $1.4hc$ (the SFT estimation error at the bottom-hole was $0.15\text{ }^{\circ}\text{C}$ for the linear SFT profile scenario, and $0.24\text{ }^{\circ}\text{C}$ for the S-shaped SFT profile scenario) and it was used to account for the heat transfer rate within the drill pipe in the 2^{nd} period. In the annulus, forced convective heat transfer dominates the heat transfer process. The SFT was estimated assuming different annulus flow rates and the estimation error at bottom-hole was calculated (Figure 3.5). As expected, the SFT was underestimated when temperature measurements under cooling conditions were used in all cases. This is because with continuous cold injection in the annulus during the 2^{nd} period, the temperature was only partially recovered in the borehole compared to the shut-in condition. The higher the flow rate in the annulus was, the less the heat would recover and the larger the resulting underestimation error in the SFT (Figure 3.5.c, Figure 3.5.d). For small values of flow rate in the annulus up to 0.7 L/s (corresponding fluid velocity of 0.05 m/s at the bottom-hole), the maximum estimation error at the bottom-hole was around $74\text{ }^{\circ}\text{C}$ (14.8%, error in percentage) when the linear SFT profile was assumed and $24\text{ }^{\circ}\text{C}$ (4.8%) for the S-shaped SFT profile. The reason for the smaller estimation error for the S-shaped profile is the higher SFT value along most parts of the well. Therefore, the fluid is less cooled, resulting in earlier thermal recovery. However, it is noticed that the maximum SFT estimation error along the well depth could be in some cases much greater than the error at the borehole bottom (Figure 3.5.b, maximum underestimation error of $143\text{ }^{\circ}\text{C}$ was found at 1800 m depth for the flow rate of 0.5 L/s in the annulus).

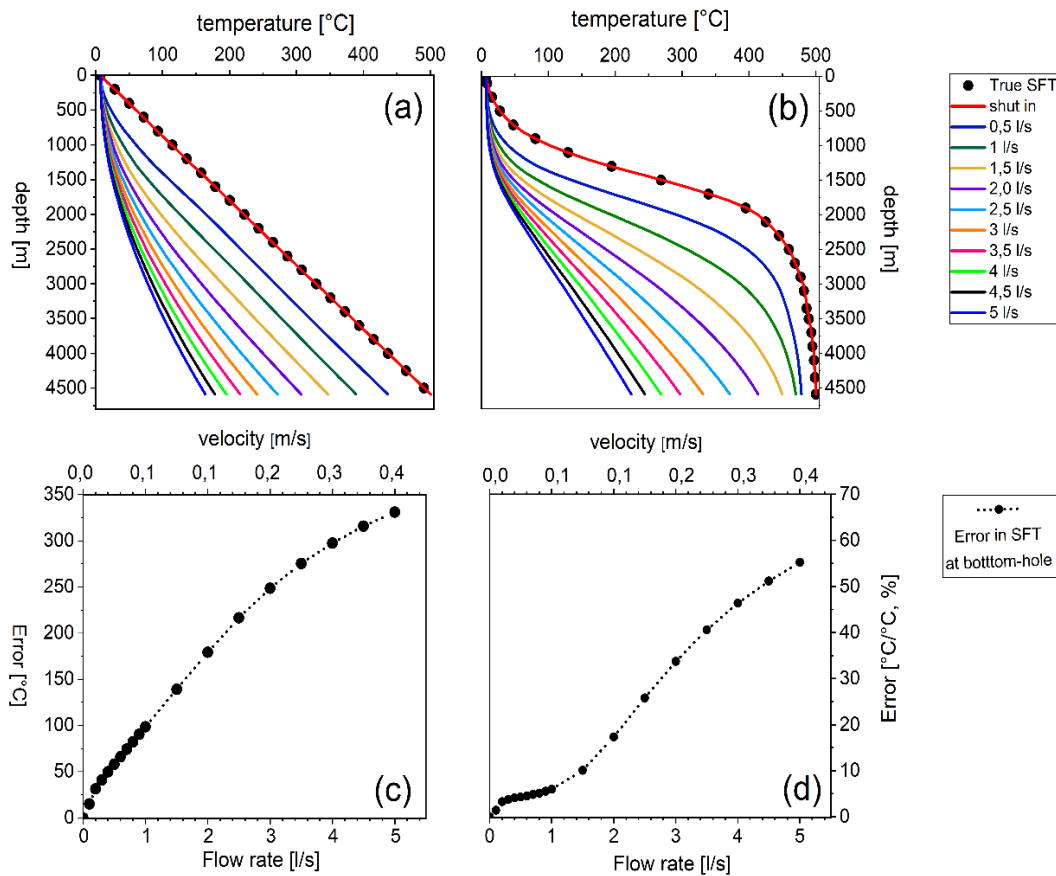


Figure 3.5: Estimated SFT profile under different flow rates (Q) in the annulus during the 2nd period versus depth when assuming (a) a linear SFT profile and (b) S-shaped SFT profile (black dots represent the true SFTs, red lines represent the SFT estimates under real shut-in conditions). (c) Errors in SFT estimates for the linear-shaped SFT profile case. (d) Errors in SFT estimates for the S-shaped SFT profile case.

3.4.3 Characterization of the fluid loss in the well

Herein, we present exemplary simulated temperature logs under flow rates of 5 L/s and 50 L/s for an S-shaped SFT profile (Figure 3.6). The results for the linear SFT profile were omitted since it was observed that the shape of the SFT profile had a negligible influence on the temperature response to fluid loss. An abrupt increase in the vertical temperature gradient below the loss zone at 3.35 km depth is detected in each temperature log. It is also noticed that the relationship between the increase of the temperature gradient and the percentage of fluid loss is non-monotonic. On the one hand, when the percentage of fluid loss is below 95%, a steeper temperature gradient indicates a higher amount of fluid loss in the borehole. Such behavior can be explained

by the fact that with more fluid being lost from the annulus, the fluid remaining in the borehole has more residence time to gain heat from the hotter surroundings and thereby the fluid temperature tends to increase. On the other hand, the increase in the temperature gradient drops when the fluid is almost completely lost. This is due to the fact that very high fluid losses cause very low remaining flow rates. As a result, the heat transfer rate from the formation to the annulus fluid is also strongly impaired. The reduced heat flux results in lower fluid temperatures both in the annulus and drill pipe. We performed further analyses by calculating the increase of the vertical temperature gradient due to the presence of fluid loss for each of the generated temperature logs. This increase was quantified by computing the ratio of the slope of the temperature profile above the loss zone to the slope below the loss zone. Since the borehole temperature was considered to approach steady-state after ten days, the temperature slope could be approximated using a linear gradient. The relationship between the gradient ratio and the percentage of fluid loss under different flow rates is illustrated in Figure 3.7. The non-monotonic relationship between the gradient ratio and the fluid loss (with maximum temperature gradient ratios occurring when the fluid loss exceeds 95%), which has already been discussed earlier, is observed for each flow rate under consideration. Moreover, the dependence of the gradient ratio on the flow rate seems to be more complex. The gradient ratio tends to be independent of the flow rate if the percentage of fluid loss is low, e.g., < 30%. For fluid losses > 30%, smaller temperature gradient ratios are observed for lower flow rates. However, for flow rates greater than 20 L/s (flow velocity > 0.5 m/s), the gradient ratio is almost independent to the flow rate except when the fluid loss is greater than 90%.

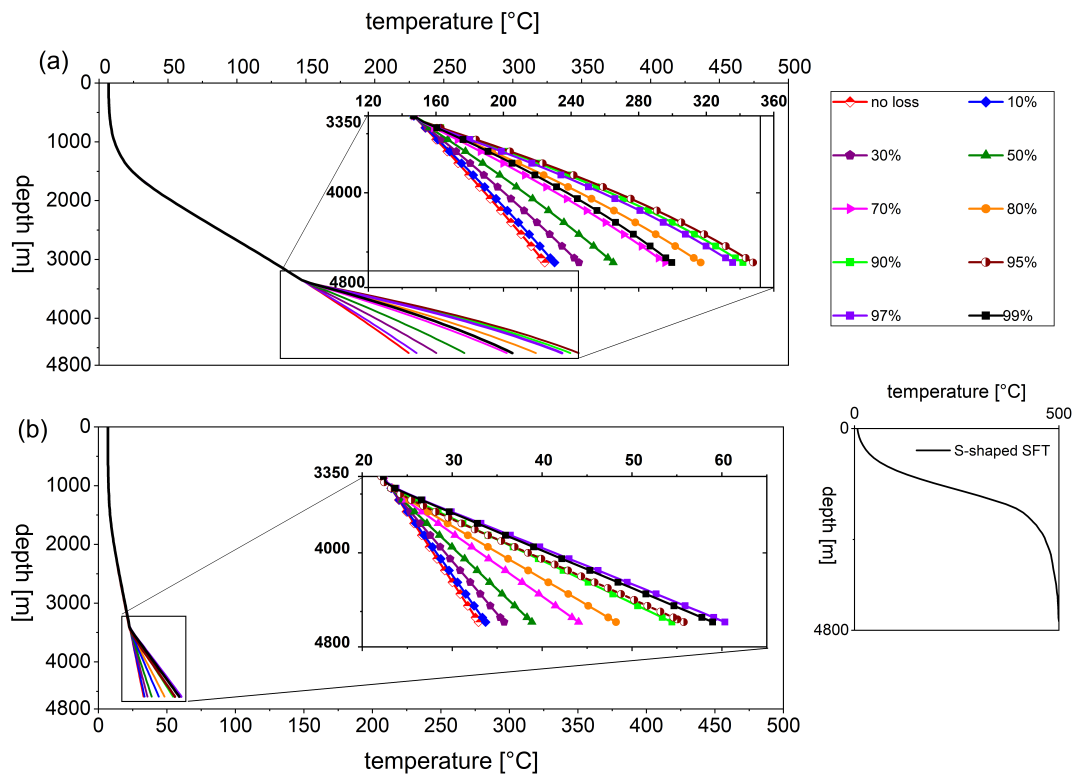


Figure 3.6: The generated temperature logs for the S-shaped SFT profile case considering different percentages of fluid loss at a depth of 3.35 km. (a) Results for the injection flow rate of 5 L/s. (b) Results for the injection flow rate of 50 L/s.

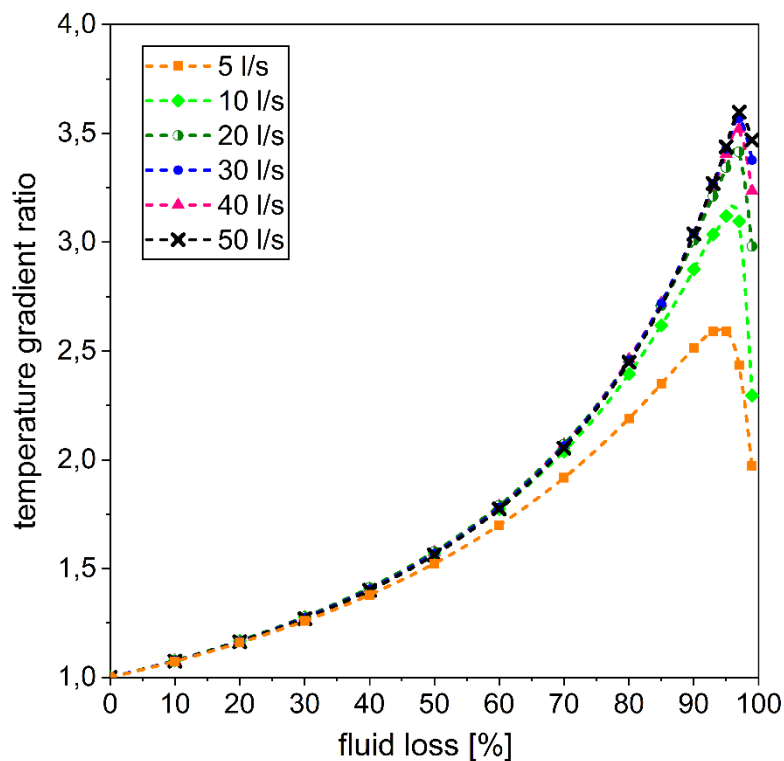


Figure 3.7: The ratio of temperature gradient below the fluid loss zone (3.35 km depth) to the gradient above the fluid loss zone versus the percentage of fluid loss (S-shaped SFT profile is assumed).

3.5 Conclusion

The assessment of geothermal reservoirs relies on the information supplied by logging tools, with temperature logs among the most important ones. The in-house numerical tool developed to simulate the thermal response of the wellbore and the formation during fluid circulation and shut-in conditions is intended to fill the absence of a quantitative interpretation of temperature logs and the associated uncertainties. It accounts especially for the heat transfer process from the formation towards the specific location of the measurement tools including the drill pipe, annulus or open borehole. Particular care is given to the correct treatment of the transient heat transfer through the multiple interfaces (casing – annulus – drill pipe - drill fluid) in such a complex thermal system. The quality of the simulation tool was demonstrated by comparison with borehole temperatures from analytical solutions. In this study,

the simulator was applied to generate synthetic shut-in and dynamic temperature logs. The temperature logs were interpreted for two purposes: SFT estimation and characterization of loss zones. The major findings and the underlying messages conveyed in this study are as follows:

- (1) The shut-in temperature depends significantly on the magnitude of free convection, which enhances the heat transfer rate. In this study, a maximum difference of 30 °C in BHT predictions between the two extreme scenarios of free convection is found. In this regard, a careful parameterization of the heat transfer rate is especially important in the early transient stage of shut-in heat recovery.
- (2) The Horner-plot method may strongly underestimate the SFT if early shut-in (within 24 hours) temperature measurement data are used. However, it provides high accuracy SFT estimates (percentage error < 3%) when using long-term shut-in (two days up to four days) temperature measurement data.
- (3) Using temperature logs obtained under borehole cooling conditions can become inauspicious for the Horner-plot interpretation method even at small cooling flow rates. This can yield significant errors (e.g. 24 °C and 74 °C at a flow rate of 0.7 L/s for a linear- and S-shaped SFT, respectively) in the bottom-hole SFT estimation.
- (4) In the presence of fluid loss, the local temperature gradient change is affected by the flow rate, the percentage of fluid loss as well as the overall rate of the lateral heat transfer from the formation to the borehole fluid. It was found that for fluid losses less than 30%, or under relatively high flow rates (>20 L/s), the gradient change can be independent on the flow rates.

Under the specific conditions of high-temperature boreholes the temperature logging data represents a complex response to the wellbore layout, the flow conditions, the heat transfer mechanism, etc. Under these constraints, a simple interpretation of temperature logs can be strongly misleading and more sophisticated techniques accounting for key factors by numerical simulation are required. Herein, the impacts of these factors were investigated by individual sensitivity analysis. However, in real geothermal applications, these impacts may overlap. Therefore, simulations in this context need to be joined by inverse procedures. In this way, the present contribution represents an important step towards a more sophisticated interpretation of real project data. It requires accounting, in a detailed manner, for the geometrical setting, on the history of injection, drilling, logging (even the time lapse of logging start to logging end) and on the appraisal of measurement errors. Work is now underway to interpret dynamic temperature logs using inverse modeling techniques.

Acknowledgments

The study is part of the DEEPEGS “Deployment of Deep Enhanced Geothermal Systems for Sustainable Energy Business” Project within European Union’s Horizon 2020 research and innovation program. The support from both the Helmholtz portfolio project “Geoenergy” and the program “Renewable Energies”, under the topic “Geothermal Energy Systems”, is also gratefully acknowledged. We also thank the EnBW Energie Baden-Württemberg AG for supporting geothermal research at KIT. This work is supported in part by funds from the European Union’s HORIZON 2020 research and innovation program under Grant Agreement No. 690771.

Chapter 4

Uncertainty analysis of numerical inversions of temperature logs from boreholes under injection conditions

This part is reproduced from the manuscript that has been published in the journal of *Journal of Geophysics and Engineering*.

Jia W., Fabian N., Emmanuel G., Thomas K. [2021]: Uncertainty analysis of numerical inversions of temperature logs from boreholes under injection conditions; *Journal of Geophysics and Engineering* (18), 1022–1034

Abstract

Conventional methods to estimate the static formation temperature (SFT) require borehole temperature data measured under thermal recovery periods. This can be both economically and technically prohibitive in the real operational conditions, especially for high-temperature boreholes. This study investigates the use of temperature logs obtained under injection conditions for SFT determination through inverse modeling. In particular, an adaptive sampling approach based on machine learning techniques is adopted to explore the model space with efficiency by iteratively proposing samples based on results from previous runs. Synthetic case studies are carried out with a rigorous assessment of the factors affecting the quality of the SFT estimates for deep hot

wells. The results show that using temperature data measured under higher flow rates or after longer injection times could lead to less reliable results. Moreover, the estimation error exhibits an almost linear dependency on the standard error of the measured borehole temperatures. Besides, potential flow loss zones in the borehole would lead to increased uncertainties in the SFT estimates. Consequently, any prior knowledge about the amount of flow loss could improve the estimation accuracy considerably. For formations with thermal gradients varying with depth, prior information on the location depths of the gradient change is necessary to prevent spurious results. The presented inversion scheme is demonstrated an efficient tool assisting the uncertainty quantification for borehole data interpretation. Although only temperature data is considered in this work, other types of data such as flow and transport measurements can be jointly used in this method for geophysical and rock physics studies.

4.1 Introduction

The undisturbed or static formation temperature (SFT) is a key objective of the analysis of borehole measurements. It is a particularly crucial parameter during the exploration and exploitation of geothermal and hydrocarbon resources, as it reveals the thermal reserves (Prensky et al. 1992), affects the transport properties of hydrocarbons (Kutasov and Eppelbaum 2010), and determines the drilling operation and production parameters in geothermal and oil reservoirs (Bu et al. 2012). Over the past decades, temperature surveys from geothermal and petroleum wells have been widely applied to infer the SFT (Roux et al. 1980; Hasan et al. 1994; Espinosa-Paredes and Garcia-Gutierrez 2003; Bassam et al. 2010). Most of these methods rely on different analytical models that extrapolate borehole-temperature buildup data after a previous thermal perturbation period (the drilling process) under shut-in conditions (i.e., in a static water column). Advanced approaches have been developed, for instance, to apply neural networks to synthetic and field thermal recovery data (Bassam et al. 2010; Wong-Loya et al. 2012). To date, the challenges in these numerical approaches have been hardly overcome due to unrealistic assumptions on the borehole drilling process, neglecting measurement errors, etc (Aabø and Hermanrud 2019; Andaverde et al. 2005).

On the operational side, the acquisition of temperature data for a relatively long thermal recovery period (hours up to several days) can become a difficult endeavor in real situations, especially in high-temperature boreholes. Technical challenges may

arise since conventional tools have an upper operating temperature limit (~ 300 °C). Recent developments are in high-temperature measuring instruments rated above 350 °C (Ásmundsson et al. 2014; Bertani et al. 2018; Friðleifsson et al. 2018; Okamoto et al. 2019). However, the endurance time of these logging tools to the harsh environment is limited to only a few hours, which imposes limitations for applying the aforementioned correction methods on the shut-in temperature data.

On the other hand, dynamic temperature logs acquired under flow conditions could also provide valuable information about the borehole and its surrounding formation. Barton et al. (1995) and Steingrímsson (2013) analyzed thermal logging data to determine the feed/loss zone locations, their relative sizes, and associated flow rates by detecting “kick” in the temperature profiles. Patterson et al. (2017) used snapshots of the temperature profile at discrete times to indicate the rate of wellbore heat gain/loss as well as the evolution of reservoir temperature under normal borehole operating conditions. Drakeley et al. (2006) and Wang et al. (2010) applied optic fiber Distributed Temperature Sensing (DTS) to monitor real-time downhole temperatures at high frequency and spatial resolution. Following the pioneering work of Nowak (1953) on the diagnosis of zonal-flow contributions in the borehole based on temperature data, a few papers presented the use of temperature profiles to derive flow rate measurement (Kabir et al. 2012; Reges et al. 2016; Silva et al. 2019). However, to the authors’ knowledge, the assessment of SFT using temperature logs obtained under dynamic situations (i.e., arising from the drilling process or flow injections) is still missing.

In this study, we apply an inversion modeling approach to analyze the uncertainty in the interpretation of dynamic temperature logs for SFT determination. Specifically, the inversion scheme involves the reduced-order modeling which has proved to be a promising method to solve non-linear inverse problems in recent years (Mirghani et al. 2012; Chen et al. 2017; Schulte et al. 2020). A reduced-order model (ROM), also known as a surrogate model, can be considered as a regression for a set of input-output data obtained from a high-fidelity code. It is often used to replace the complex original physical model to accelerate the computational speed, and to improve the efficiency in the search of model space of an inverse problem (Zhang, Zheng, Chen, Wu and Zeng 2020). A variety of techniques have been tried to construct ROMs, such as polynomials (Oladyshkin et al. 2011), kriging (Mo et al. 2019), while other studies consider machine learning (also referred to as data-driven) methods, including support vector machine (Jhong et al. 2017) and artificial neural networks (Sudakov et al. 2019) to name a few.

We adopt a simple, non-parametric, supervised machine learning model called K-Nearest Neighbor (KNN, see Chapter 4.2.2 for more details) to build a ROM. The ROM is then integrated within the inversion process to propose sampling points in each iteration. A detailed description of the workflow is given in Chapter 4.2. In Chapter 4.3 and Chapter 4.4, the inversion procedure is applied to different case studies to investigate several points affecting the accuracy of the determined SFT which are related to the injection conditions, accuracy of the data, as well as aspects from the inverse modeling such as the prior information and the type of misfit function. Our study aims to contribute to more understanding of these impacting factors and present a method for quantifying the uncertainties associated with them. As such, the capability of the data-driven surrogate modeling approach to solve inverse problems using borehole logging data, which has been rarely investigated in this context before, is also demonstrated.

4.2 Methodology

To determine the parameters of interest, namely the SFT and later the flow loss, together with their uncertainties (deviations from the true values), a two-step approach is applied. The first one consists in the forward modeling, which evaluates the temperature profile along the borehole by simulating advective heat transport within the borehole as well as heat transfer between the borehole and the formation, using an in-house simulator developed on the MOOSE framework (Korzani et al. 2019; Wang et al. 2019). The second step consists in the parameter inversion using an adaptive sampling approach based on the ROM, which is driven by the RAVEN software (Alfonsi et al. 2016). Specifically, RAVEN provides different machine learning algorithms to train a ROM via an Application Programming Interface (API) from the scikit-learn python library (Pedregosa et al. 2011). Besides, it couples natively with a MOOSE-based application, allowing the above two steps to be performed within one software tool. Such a framework also enables the distribution of a large number of calculations on multicore workstations and high-performance computation systems.

4.2.1 Forward thermal modeling

The forward simulation simplifies the thermal modeling procedure by assuming that the geometries of the borehole and formation are cylindrical, the fluid is incompressible and its flowing direction in the borehole is only axial. Furthermore, the rock formation is considered impermeable and the thermal dissipation and expansion effects of the fluid are negligible.

Given above, the thermal transport mechanism in the borehole is governed by both conduction and advection, which is typically expressed in cylindrical coordinates as follows (Yang et al. 2013):

$$\rho_f c_{p_f} \left(\frac{\partial T_f}{\partial t} + v_{r_f} \frac{\partial T_f}{\partial r} + v_{z_f} \frac{\partial T_f}{\partial z} \right) - \frac{\lambda_f}{r} \frac{\partial T_f}{\partial r} - \lambda_f \frac{\partial^2 T_f}{\partial r^2} - \lambda_f \frac{\partial^2 T_f}{\partial z^2} = 0. \quad (4.1)$$

Assuming incompressible flow, the continuity equation is given by:

$$\frac{1}{r} \frac{\partial (r v_{r_f})}{\partial r} + \frac{\partial v_{z_f}}{\partial z} = 0, \quad (4.2)$$

where ρ_f is the fluid density, c_{p_f} is the fluid specific heat capacity, v_z and v_r are the axial and radial flow velocities, respectively, λ_f is the thermal conductivity.

Considering only heat conduction in the formation, the energy conservation equation can be written as:

$$\rho_s c_{p_s} \frac{\partial T_s}{\partial t} - \frac{\lambda_s}{r} \frac{\partial T_s}{\partial r} - \lambda_s \frac{\partial^2 T_s}{\partial r^2} - \lambda_s \frac{\partial^2 T_s}{\partial z^2} = 0, \quad (4.3)$$

where ρ_s , c_{p_s} , λ_s is the density, heat capacity, and thermal conductivity of the formation, respectively.

The thermal exchange between the borehole and formation is modeled via thermal transfer relations at their interface:

$$q = -\lambda_s \left(\frac{\partial T_s}{\partial r} \right) \Big|_{\Gamma_{s,f}} = h(T_s - T_f), \quad (4.4)$$

q is the heat flux, $\Gamma_{s,f}$ is the interfacial area between the fluid and the formation, h is the heat transfer coefficient under forced convection. A detailed description for the calculation of h can be found in Wang et al. (2019).

4.2.2 Adaptive sampling based on the reduced order model

The inversion or estimation of the SFT and the flow rate is conducted using an adaptive sampling approach. It is performed by building a surrogate model using the results of previous simulations, predicting the system behavior, and proposing the most informative region in the model space for the next sampling step. Thus, it reduces the number of iterations to find solutions for the inverted parameters compared to other classical sampling methods such as Monte-Carlo, Latin Hypercube Sampling, etc (Mandelli et al. 2015).

In the following analysis, the ROM is built using perhaps the most simple and transparent surrogate model - the K-Nearest Neighbor (KNN) (Runarsson 2004). KNN is non-parametric and requires no prior knowledge about the mapping function type. Thus, it is free to learn any functional form from the training data (Russell and Norvig 2002). Furthermore, it is easy to implement since the learning consists of simply storing points that are evaluated using the high-fidelity model, and each time a point is added, the trained model is improved. KNN predicts a so-called label (defined, in our case in Equation 4.7) of a sampling point based on the labels of its k-nearest neighbors using the following formula:

$$C = \frac{w_1 C_1 + \dots + w_k C_k}{\sum_{j=1}^k w_j}, \quad (4.5)$$

where C is the label associated with each nearest neighbor, k is the number of nearest neighbors. The weight of the j -th nearest neighbor (p_j) for the evaluated point (p) is defined as $w_j = 1/dist(p, p_j)$, where the distance $dist(p, p_j)$ is the Euclidian distance between p and p_j .

The ROM is then used as a “classifier” that predicts where further exploration of the model space should be oriented to develop a Limit Surface (LS), which identifies the boundary between the positive and negative Boolean labels established according to a user-defined constraint criterion (Alfonsi et al. 2016). In our analysis, such criterion is constructed using the root mean square error ($RMSE$), which describes the discrepancy between the simulated and the measured borehole temperatures as follows:

$$RMSE = \sqrt{\frac{\sum_{i=1}^m (T_{sim} - T_{measure})^2}{m}}, \quad (4.6)$$

where T_{sim} is the simulated temperature, $T_{measure}$ is the measured temperature and m is the number of the sampled borehole temperatures along the depth.

A decision function $C(RMSE)$ is defined to recast the response of the system into a binary form:

$$C(RMSE) = \begin{cases} 1 & \text{if } RMSE < RMSE_{thres} \\ -1 & \text{if } RMSE > RMSE_{thres} \end{cases}, \quad (4.7)$$

where $RMSE_{thres}$ is the $RMSE$ threshold value.

In reality, the $RMSE$ comes from two sources: the errors of (1) the measured temperatures and (2) the calculated T_{sim} in the forward modeling, both are with respect to the true borehole temperatures. The reason for choosing the $RMSE$ as a criterion is that the $RMSE$ can be considered as an analogy to the standard deviation of the measurement data due to their arithmetic similarity (i.e., assuming the data are not biased) (Meyer 2012). Meanwhile, it is also the mostly used metric to measure the model prediction quality, which makes it also suitable for presenting the second type of error source. In all case studies of this work, only one error source is included in the $RMSE$ at a time to investigate separately their impacts on the temperature log interpretation. We will first focus on the measurement errors and later include aspects of the forward modeling by considering wrong model assumptions. Given that temperature logging instruments typically have an accuracy of ± 1 °C (Cao et al. 1988; Förster 2001) and the errors in the measurements can still rise at higher temperatures (Sharma et al. 2021), we explicitly select different $RMSE_{thres}$ values ranging from 0.5 °C to 2.0 °C as the possibly acceptable fitting qualities between the model predictions and the measurements if allowing either data to have some errors..

In the context of our study, the adopted inversion scheme is intended to find the boundary (LS) which delimitates the model space–SFT (one-dimensional) or SFT and the flow loss (two-dimensional), depending on whether the $RMSE$ values of the model predictions are larger or smaller than the $RMSE_{thres}$. In summary, the generalized workflow applied for this work consists of the following steps:

1. Initial sampling points in the model space are generated using the Monte Carlo forward sampling scheme for the model parameters, namely the SFT and flow rate.
2. Borehole temperatures at those measured depths are computed using the borehole simulator for each sampling point.
3. The decision function, Equation 4.7, is evaluated using the results from Step 2.

4. The data pairs {model parameters, decision function value} are used to train the ROM using the KNN classification model.
5. The ROM is used to predict the values of the decision function for all the discretization nodes of the model space and then the LS is determined based on the change of the values of the decision function (i.e., the transition from -1 to 1).
6. A score is assigned to each point on the LS according to its distance to the sampling points already taken (the larger is the distance the higher is the score) and the persistence of its predicted decision function value (the larger is the number of time the prediction for that point have changed the higher is the score). The point with the highest score is added to the training samples.
7. The procedure is repeated starting from Step 2 until convergence is achieved: a) when the LS does not change after a certain number of consecutive iterations (hereafter called persistence step) and b) when the “volume” fraction of each cell in the whole discretized model space reaches a user-defined tolerance (referred to as convergence confidence).

It is worth mentioning the first criterion above is required to prevent the searching algorithm from focusing too much on a certain region of the LS while putting too few points in other zones and thus completely hiding undiscovered regions of the LS. In addition, the latter convergence criterion determines the accuracy of the predicted LS, i.e., the smaller is the tolerance value, the finer is the discretization grid on the model domain, the more accurate is in the computed LS.

4.3 Synthetic case studies

4.3.1 Uniform geothermal gradient

In this section, factors influencing the accuracy of the SFT estimation, namely, the borehole operation parameters such as the injection flow rate and the injection duration, the quality of the temperature measurements and the presence of a flow loss zone, are examined. For simplicity, the formation is assumed to have a constant geothermal gradient.

4.3.1.1 Estimation of SFT alone

Herein, a 2-D domain, which consists of a borehole with a radius of 0.11 m and a non-permeable formation with a vertical extension of 4500 m and a lateral of 50 m is simulated. The rock formation is assumed to have constant thermal properties ($\rho_s = 2700 \text{ kg m}^{-3}$; $c_{ps} = 800 \text{ J kg}^{-1} \text{ K}^{-1}$; $\lambda_s = 2.5 \text{ W m}^{-1} \text{ K}^{-1}$). Figure 4.1a shows the initial and boundary conditions of the model. The SFT is assumed to increase linearly from 10 °C at the surface to 500 °C at 4500 m, and no flow loss occurs along the borehole. Water is injected from the wellhead into the borehole at a constant temperature (10 °C) and a constant flow rate. Borehole temperatures are then simulated assuming constant water properties ($\rho_f = 998 \text{ kg m}^{-3}$; $c_{pf} = 4182 \text{ J kg}^{-1} \text{ K}^{-1}$; $\lambda_f = 0.6 \text{ W m}^{-1} \text{ K}^{-1}$) using the forward modeling approach that was previously described. Figure 4.1b depicts the synthetic temperature logs in the borehole for different injection durations (3~12 hours) at a flow rate of 50 L/s, and Figure 4.1c for different flow rates (25~100 L/s) after a six-hour injection.

Analysis of the sensitivities of SFT estimates to the dynamic injection conditions (injection time and flow rate) and the chosen $RMSE_{thres}$ value is performed using the aforementioned adaptive sampling approach. Note that in this case, the $RMSE_{thres}$ only takes the measurement error into account. Since the SFT is a linear function of depth, only the SFT at the bottom-hole needs to be solved. The number of the realizations required for the adaptive sampling to converge typically depends on the complexity of the inverse problem (e.g., the number of the predicted variables), and the prior uncertainty (e.g., the $RMSE_{thres}$ value and model space of the variables). For all the presented inversion scenarios in this section, the input bottom-hole SFT value is set between 450–550 °C, the ROMs are trained with KNN using five-nearest neighbors (see also Table 4.1 for a summary of the relevant parameters in this study). The total number of the evaluated forward simulations for each model to reach convergence is around 100–200.

Four temperature logs obtained after different injection durations (3, 6, 9 and 12 hours) of injection at 50 L/s are inverted to estimate separately the SFT value at the bottom-hole. According to Figure 4.2a, the estimation errors in the SFT are $\pm 11.5 \text{ °C}$ ($\pm 2.3\%$), $\pm 14.4 \text{ °C}$ ($\pm 2.9\%$), $\pm 16.2 \text{ °C}$ ($\pm 3.2\%$) and $\pm 17.5 \text{ °C}$ ($\pm 3.5\%$) respectively. Figure 4.2b shows the inversion results using temperatures measured at different injection rates (25, 50, 75 and 100 L/s) after the same injection duration of 6 hours. The estimation error is found to be the lowest ($\pm 7.2 \text{ °C}/\pm 1.4\%$) when the flow rate is 25 L/s and highest ($\pm 28.9 \text{ °C}/\pm 5.8\%$) when the flow rate is 100 L/s. These results are obtained for an $RMSE_{thres}$ value of 1.0 °C. Figure 4.2c displays the results for the

Parameter type	Parameter name	Uniform geothermal gradient		Two-layer geothermal gradient	
		SFT alone	SFT & flow rate	F1A1	F2A2
Prior model parameters	SFT at 4500 m	U[450,550] °C	U[400,600] °C	U[298,748] °C	U[250,850] °C
	Flow rate below 3500 m	–	U(0,50) L/s	U(0,50) L/s	U(0,50) L/s
Parameters for the ROM and LS search	K-number of KNN	5	5	5	5
	Persistence step	30	100	100	100
	Convergence confidence	1e-3	1e-5	5e-6	5e-6

Table 4.1: Parameters for the modeling space, the KNN model and convergence criteria used for the inversion models in this study.

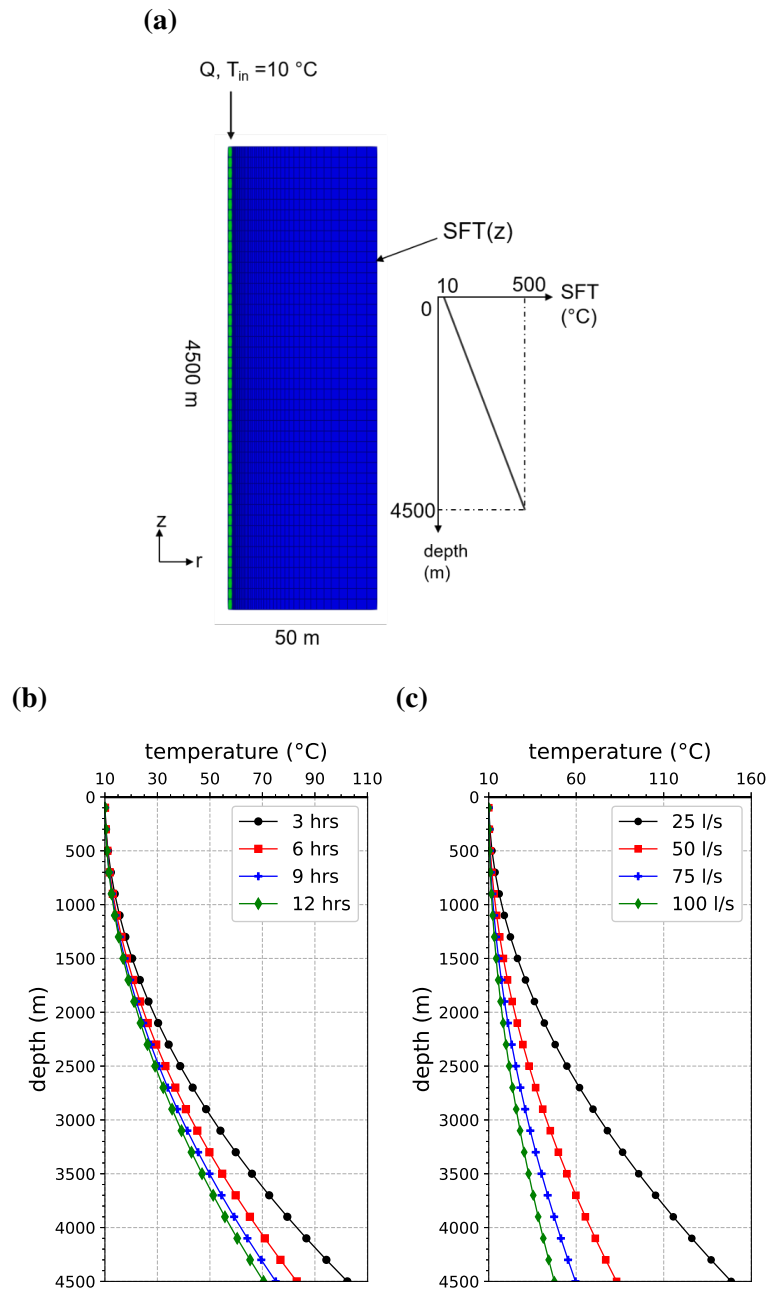


Figure 4.1: (a) Schematic of the simulation set-up with the boundary and initial conditions. Injection temperature at the well-head is $10\text{ }^{\circ}\text{C}$, SFT is a linear function of vertical depth and is applied as the initial condition and the Dirichlet boundary condition at the right edge of the formation. (b) Synthetic temperature logs after different injection durations (3, 6, 9 and 12 hours) at an rate of 50 L/s. (c) Synthetic temperature logs obtained under different flow rates (25, 50, 75, and 100 L/s) after 6 hours of injection.

formation temperature at the bottom-hole by inverting the temperature log obtained after a six-hour injection at 50 L/s considering $RMSE_{thres}$ values varying between 0.5 $^{\circ}\text{C}$ and 2 $^{\circ}\text{C}$ (with a step of 0.5 $^{\circ}\text{C}$). As expected, the error of the estimate increases (from $\pm 7.2\text{ }^{\circ}\text{C}$ to $\pm 28.9\text{ }^{\circ}\text{C}$) as the $RMSE_{thres}$ value increases from 0.5 $^{\circ}\text{C}$ to 2.0

°C.

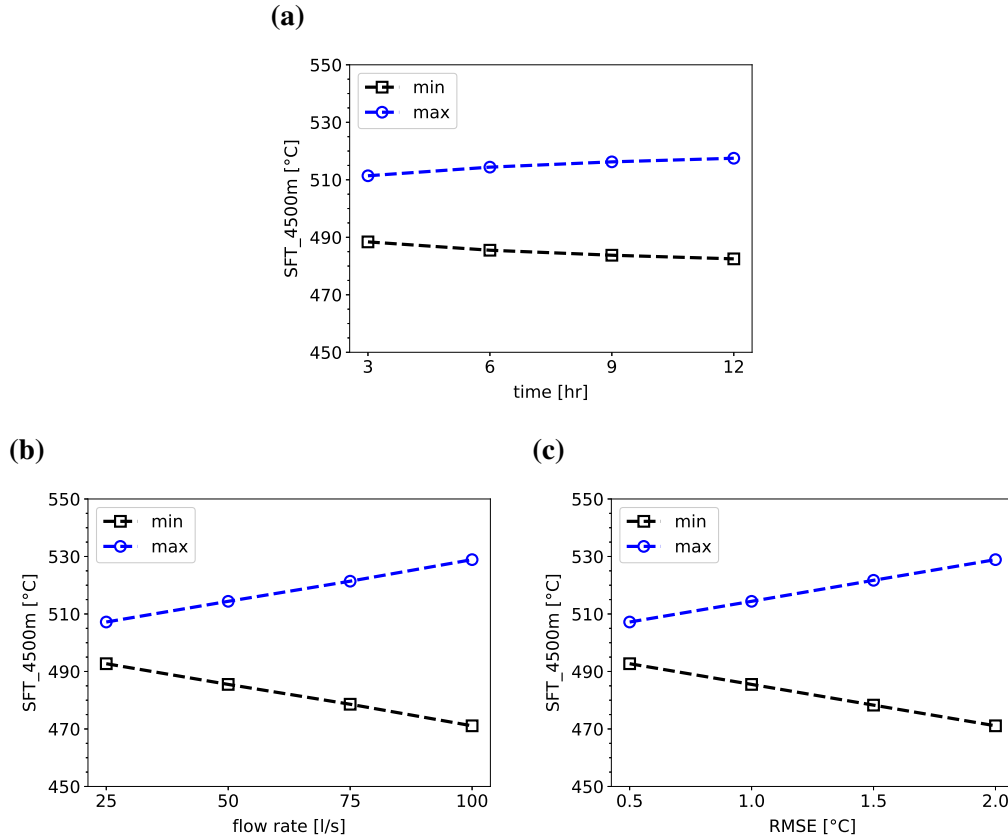


Figure 4.2: Comparisons of the maximum and minimum values of the estimated SFT at the bottom-hole (4500 m depth) considering: (a) different injection durations (3, 6, 9 and 12 hours), flow rate of 50 L/s and $RSME_{thres}=1.0$ °C; (b) different flow rates (25, 50, 75 and 100 L/s), injection duration of 6 hours and $RSME_{thre} = 1.0$ °C; (c) different $RSME_{thre}$ values (0.5, 1.0, 1.5, and 2.0 °C), injection duration of 6 hours and flow rate = 50 L/s.

4.3.1.2 Estimation of SFT and flow loss

The loss of the circulated fluid is commonly encountered for drilled boreholes due to the existence of faulted or fractured formations (Allahvirdizadeh 2020). To take such a case into account, a loss zone at 3500 m is added to the same model explained in Figure 4.1a. It is assumed the injection flow rate becomes 25 L/s below 3500 m due to the loss. As shown in Figure 4.3, a significant temperature gradient increase after the loss zone is observed on each temperature profile measured at a different time.

In the following, the bottom-hole SFT and the remaining flow below the loss zone are inverted simultaneously, using the temperature log obtained six hours after injection starts. The dependency of the results on the accuracy of the temperature measurement is analyzed again by taking four different $RMSE_{thres}$ values in the inversion procedure.

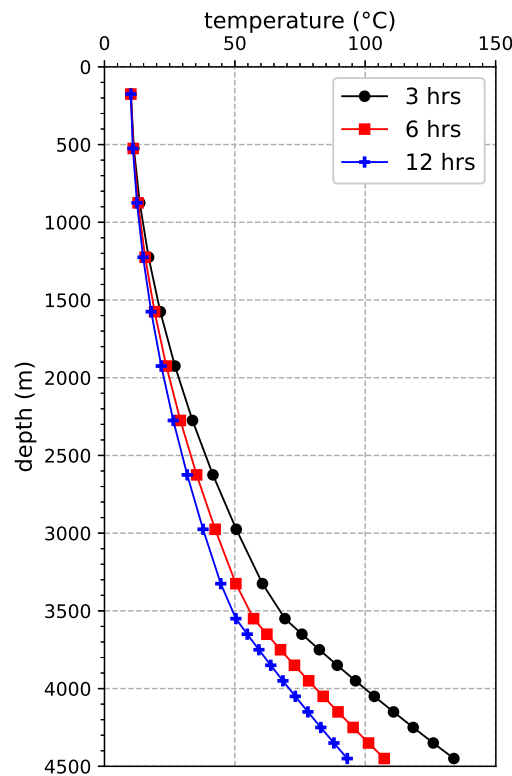


Figure 4.3: Synthetic temperature logs of the borehole fluid after different injection durations (3, 6 and 12 hours) considering a flow rate of 50 L/s above 3500 m and 25 L/s below 3500 m due to the loss.

The prior distributions of the bottom-hole SFT and the remaining flow rate are 400–600 °C and 0–50 L/s respectively. The number of steps for the models to converge is around 1000–1500. As can be seen from Figure 4.4, the errors of both SFT and flow rate estimates arise as the $RMSE_{thres}$ value becomes larger. For instance, when $RMSE_{thres}$ is 0.5 °C, the maximum estimation error is ~ 10 °C (2%) for the bottom-hole SFT and ~ 1.5 L/s (3%) for the remaining flow rate below 3500 m. However, when $RMSE_{thres}$ rises up to 2.0 °C, the maximum estimation error becomes ~ 48 °C (9.6%) for the SFT and ~ 6.5 L/s (26%) for the flow rate. Also, the elliptical shape of the contour lines indicates a positive correlation between the bottom-hole SFT value and the remaining flow rate. Furthermore, it is found that the uncertainty of the SFT estimation increases when a flow loss zone exists. For example, compared with the inversion results from Chapter 4.3.1.1 where no loss occurs, the maximum error in the SFT estimate is increased by 2.8 °C for $RMSE_{thres} = 0.5$ °C and 19.1 °C for $RMSE_{thres} = 2.0$ °C.

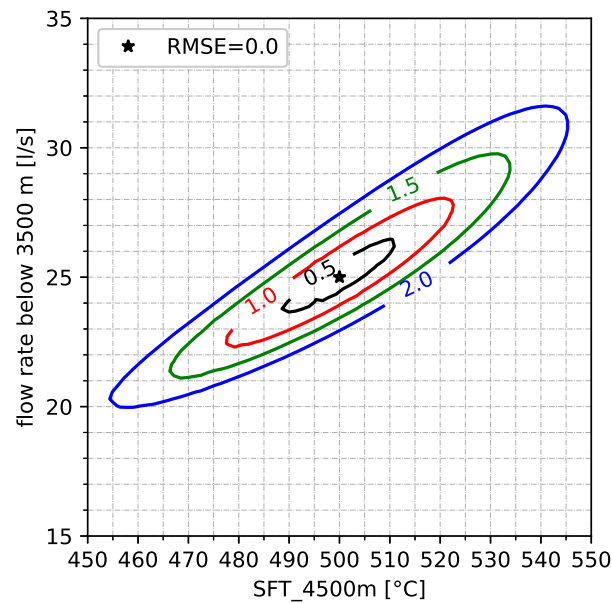


Figure 4.4: Contour plot of the *RMSE* as a function of the two estimated variables: SFT at bottom-hole depth (horizontal axis) and the flow rates below 3500 m (vertical axis). The black star marks the true values for bottom-hole SFT and flow rate below 3500 m (which corresponds to an *RMSE* value of 0.0 °C).

4.3.2 Two-layer geothermal gradient

Herein, we extend the complexity of the above study by considering a formation (hereafter referred to as formation F1) consisting of two layers with different geothermal gradients. The purpose of the new study is to investigate the influence of different prior assumptions about the geothermal gradient (i.e., the second type of error source contributing to the *RMSE*, as discussed in Chapter 4.2.2) on the prediction of the SFT and the flow rate. We would like to mention that this study is inspired by the RN-15/IDDP-2 deep well in Reykjanes, Iceland. The well was drilled by deepening an existing well (RN-15) of 2500 m depth to 4500 m deep. During the drilling, a major flow loss was reported at around 3500 m. High-temperature environments around the well have been confirmed by measured temperatures up to 426 °C (Friðleifsson et al. 2018). The SFT profile from the surface to 2500 m has been directly calculated using the borehole thermal recovery temperature data. However, the determination of the SFT below 2500 m has been an issue of much interest. Furthermore, cold fluid has been continuously injected during the drilling to cool down the casing and the formation (Peter-Borie et al. 2018), which makes only temperature measurements from injection conditions available for assessing the formation temperature.

For F1, the true formation temperature is assumed to increase from the surface with a

constant gradient of $0.096\text{ }^{\circ}\text{C/m}$ to $298\text{ }^{\circ}\text{C}$ at 3000 m and then continue to increase with a gradient of $0.135\text{ }^{\circ}\text{C/m}$ until it reaches $500\text{ }^{\circ}\text{C}$ at 4500 m (Figure 4.5, SFT_F1). Figure 4.5 (blue line) also illustrates the borehole temperature profile after six hours' injection at a rate of 50 L/s . Noticeably, the local flow loss of 25 L/s at 3500 m causes a dramatic increment in the borehole temperature gradient (Figure 4.5, red dashed line), whereas the increase of the SFT gradient after 3000 m has no obvious impact on the local fluid temperature gradient change.

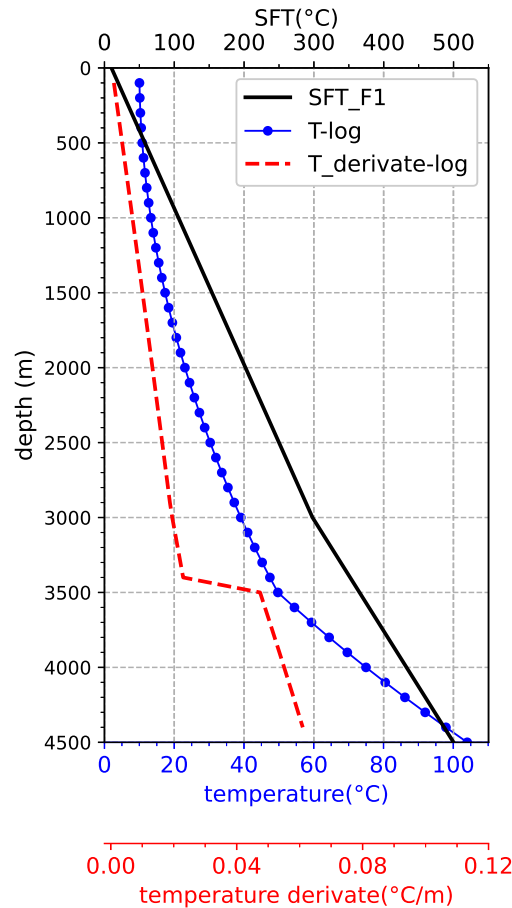


Figure 4.5: Predefined SFT profile of formation F1 (black line), borehole temperature profile (blue line) calculated after 6 hours injection at 50 L/s and the derivative of temperature with respect to depth (red dashed line).

In the following investigated scenarios, the SFT in the upper 2500 m is considered already known. However, different assumptions about the geothermal gradient below 2500 m are made. One model, referred to as F1A1, hypothesizes a constant thermal gradient from the surface until 3000 m (i.e., consistent with the truth) and another possibly different gradient below 3000 m . Therefore, the SFT can be linearly extrapolated from 2500 m until 3000 m but remains unknown for the second layer. In another model (F1A2), however, a linear-shape SFT for the whole depth interval $2500\text{--}4500\text{ m}$ is assumed. By comparing F1A2 to F1A1, a question being addressed is: Without

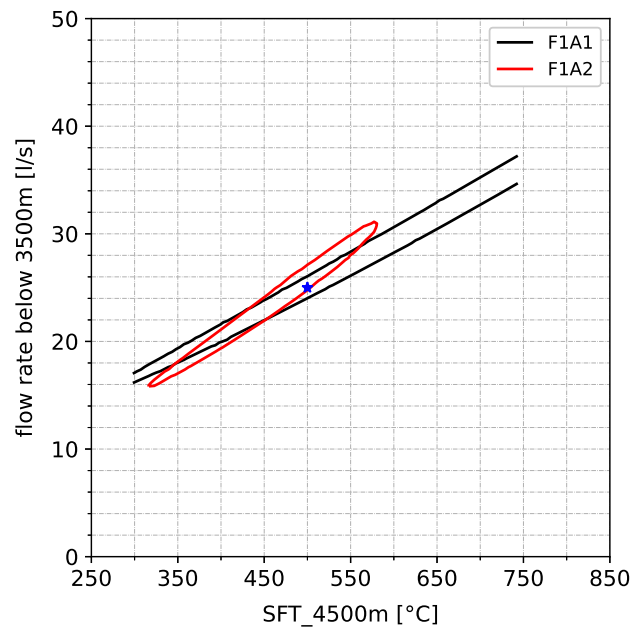


Figure 4.6: Contour plot of the $RMSE_{thres} = 1.0$ °C in the exploration space of SFT value at the bottom hole and the flow rate below 3500 m for model F1A1 and F1A2. The blue star marks the true values for the SFT and the flow rate (500 °C, 25 L/s).

knowing how the geothermal gradient varies within the intended depth interval, what would be the impact of just assuming a uniform geothermal gradient—a commonly adopted simplification in geothermal studies (Gholamrezaie et al. 2018; Al Saedi et al. 2019)—on the determination of SFT?

For both models, the flow rate below 3500 m is a prediction variable. Additional inversion parameter for F1A1 is the SFT in the depth interval 3000–4500 m, and for F1A2, the SFT in the depth interval 2500–4500 m. Again, assuming a constant geothermal gradient within each layer, only the SFT value at the bottom depth (4500 m) to be solved in both cases. The thermal gradient is considered to possibly vary between 0 and 0.3 °C/m (Bahlburg and Breitzkreuz 2018). Accordingly, the explored values for the SFT at 4500 m for F1A1 and F1A2 are 298–748 °C and 250–850 °C, respectively. The flow rate below 3500 m is assumed to be uniformly distributed on the interval [0,50] L/s. The total number of the performed forward simulations for model F1A1 is ~3800 and for model F1A2 is ~2700.

Figure 4.6 shows the contour plots of $RMSE_{thres} = 1.0$ °C for model F1A1 and F1A2 in the explored space of the bottom-hole SFT value and the flow rate below 3500 m. For model F1A1, both the SFT and the flow rate are poorly estimated: the acceptable SFT at 4500 m covers the entire domain allowed, 298–748 °C, and the flow rate can vary between 16 L/s and 38 L/s. Nonetheless, there is still a strong correlation between the flow rate value and the associated SFT value. On the other hand, both variables in

F1A2 seem to be better constrained compared to F1A1, although the variability of the inverted values is still quite high.

4.4 Discussion

4.4.1 Impact of the injection and logging conditions

As shown in Figure 4.2, when assessing the SFT alone through dynamic temperature log interpretation, the accuracy of the results depends strongly on both the flow rate and the duration of the injection before the logs are run. For the same injection period prior to the logging, the errors of the estimates increase with the injection rate. Similarly, for a constant injection rate, longer injection durations lead to decreasing accuracies of the estimates. Therefore, the determination of SFT using dynamic temperature logs requires a careful selection of these logs. As such, the inversion scheme can also be applied to propose appropriate temperature logs to be used. For example, for the investigated case in 4.3.1.1, the time at which the log is acquired needs to be restricted according to the injection rate and the desired accuracy of the SFT estimates. To achieve an accuracy of ± 10 °C, temperatures measured within 12 hours of injection can be accepted for an injection rate of 25 L/s, whereas only those logs conducted within the first two hours of injection can be used if the injection rate is 50 L/s (Figure 4.7). However, it should be pointed out that our discussion is only based on stable injection conditions (i.e., constant injection rates). In real practices, where multiple temperature surveys are obtained for the same borehole, the injection rates as well as their respective injection duration, before these logs are obtained can be very different. For such situations, as both the flow rate and injection duration will affect the accuracy of the SFT estimates, it might be necessary to use several temperature logs to perform independent inversion procedures and make a cross-comparison of the results.

Herein, the inversion study was only performed on the instantaneous depth-temperature profiles in the borehole. In other words, we assumed that temperatures at all sampling depths were recorded simultaneously. As already mentioned in the Introduction section, the acquisition of this type of temperature logs can be achieved by using DTS. In contrast, conventional logging methods such as wireline logging often involve running a temperature sensor in or out along the borehole and recording the

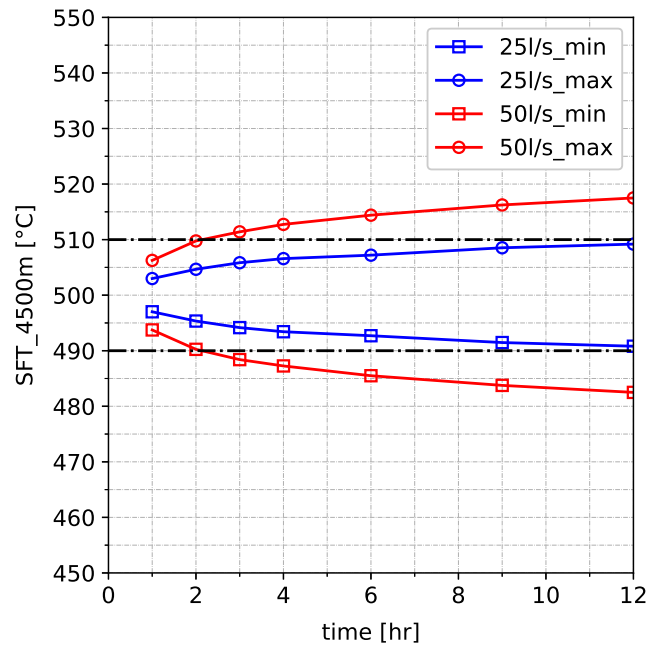


Figure 4.7: Maximum (circles) and minimum (squares) values of the estimated SFT at the bottom-hole using temperature logs obtained under injection rate 25 L/s (blue line) and 50 L/s (red line) after different injection durations (1, 2, 3, 4, 6, 9 and 12 hrs) considering $RMSE_{thres}=1.0\text{ }^{\circ}\text{C}$ (for the described model in Chapter 4.3.1.1).

temperature at each specified depth. Since the temperature sensor requires some time to reach thermal equilibrium with the measured fluid, the logging speed needs to be limited to attain a high accuracy of the temperature data (Sharma et al. 2021). Given a typical logging speed of 10–15 m/min (Prensky et al. 1992), the logging time for a well with a depth of 4500 m would be 5–7.5 hours. The present study indicates that such a time span can cause varying error in the SFT estimate for different locations as they have inconsistent exposure time to the thermal disturbance at the time of temperature sampling. Namely, the later the temperature is measured at a given depth, the higher the uncertainty in the SFT estimate at that depth (for a constant injection flow rate).

4.4.2 Impact of a flow loss zone

In the presence of flow loss along the borehole, results of the joint estimation of SFT and flow rate below the loss zone show a clear increase in the uncertainty of the SFT estimates as indicated both in Figure 4.4 and 4.6. The reason for this behavior can be explained by the coupled effects of the formation temperature and the flow rate

on the borehole temperature. Namely, an elevated borehole temperature due to a reduced flow rate (i.e., more sufficient time for the heat exchange with the surrounding formation) could be compensated by a cooler formation temperature. Conversely, a cooler borehole temperature caused by a higher injection rate can be compensated by a hotter formation temperature. As a result, borehole temperature logs simulated using different combinations of SFT and flow rate with a wide range of values may give similar good fits to the temperature-depth data. For instance in Figure 4.8, two temperature logs, referred to as L1 and L2, that lead to the same *RMSE* value of 1.0 °C in model F1A1 (Chapter 4.3.2) are presented. Each log corresponds to an acceptable but extreme solution of this synthetic case (see Figure 4.6). Compared with the real solutions of the SFT value at the bottom-hole (500 °C) and the remaining flow rate (25 L/s) after the loss zone at 3500 m, the applied values for the bottom-hole SFT (737.4 °C) and the flow rate (34.5 L/s) to simulate L1 are much higher. On the contrary, the other valid log L2 is simulated with a significantly lower bottom-hole SFT value (289 °C) and a smaller remaining flow rate (16.9 L/s). In fact, the issue with the aforementioned thermal compensating effect can always hinder the accuracy in the estimates as long as only the temperature data is used for the simultaneous prediction of flow rate and SFT.

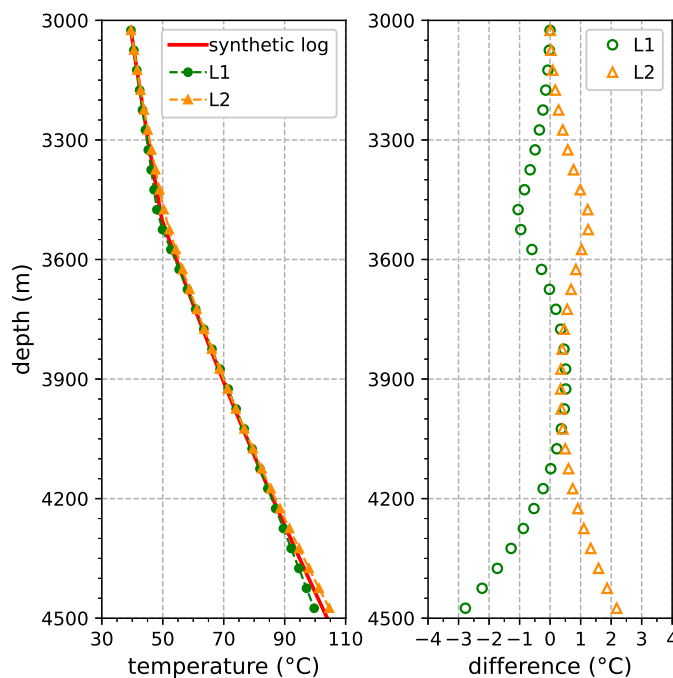


Figure 4.8: Left: borehole temperature logs (L1,L2) that both satisfy *RMSE* equals 1.0 °C in model F1A1, but are simulated with different values of SFT at the bottom-hole and flow rate below 3500 m. L1 (filled circles) is simulated with a bottom-hole SFT value of 298 °C and a flow rate of 16.9 L/s below 3500 m, and L2 (filled triangles) with a bottom-hole SFT value of 737.4 °C and a flow rate of 34.5 L/s below 3500 m. Right: temperature differences of L1 (hollow circles) and L2 (hollow triangles) with respect to the synthetic temperature log.

4.4.3 Impact of inversion constraints

4.4.3.1 The misfit function

So far, the decision function (Eq 4.7) has been defined based on the *RMSE* to take the measurement error into account. However, as observed in Figure 4.8, for the joint inversion of the SFT and the flow loss (model F1A1), the acceptable temperature logs can locally diverge from the true temperature log by up to 3 °C (especially near the loss zone and at the bottom depth), despite that $RMSE_{thres}$ equals 1 °C. Such an observation may not appear satisfactory but is inherent to the initially selected misfit function based on the L2-norm metric (hereafter referred to as M1). Given this, a different evaluation metric (referred to as M2), which is the maximum absolute difference between the predicted and the true borehole temperature ($\max(|T_{sim} - T_{measure}|_{1,2,\dots,n})$, n is the total number of the sampled logging data) can be adopted in the decision function. This new decision function is tested on model F1A1 to investigate its impact on the inversion solutions for the SFT and flow loss. The contour lines depicting the *RMSE* (F1A1-M1) and the $\max(|T_{sim} - T_{measure}|_{1,2,\dots,n})$ (F1A1-M2) both being equal to 1.0 °C are plotted in the model space (Figure 4.9). It is shown that the solution space of $\max(|T_{sim} - T_{measure}|_{1,2,\dots,n})$ being less than 1.0 °C is indeed more confined compared to that of *RMSE* being less than 1.0 °C. Furthermore, the two extreme solutions of model F1A1 when applying M1, as discussed in Figure 4.8, are removed from the solution space after using M2. However, it should be stressed that applying measurement-wise criterion would require a cautious evaluation of the data quality for each measurement. If, for instance, the error of a single measurement is higher than ± 1 °C, imposing the same type of criterion like M2 in the misfit function can lead to biased estimates.

4.4.3.2 Prior information for the model space

Prior information is another key factor that could contribute to uncertainty in the inversion results since it will decide how appropriately the presumed inversion model represents the unknown true model. In our context, knowledge about the variation of the geothermal gradient along depth needs to be provided for meaningful temperature log interpretations. In the present study, the possible change of the geothermal gradient has been assumed to be directly related to the layout of the geological layers. As such, the layer thickness, as well as the location of the layer boundaries, serve as constraints in the estimation of the geothermal gradient (i.e., SFT). The result of model F1A2

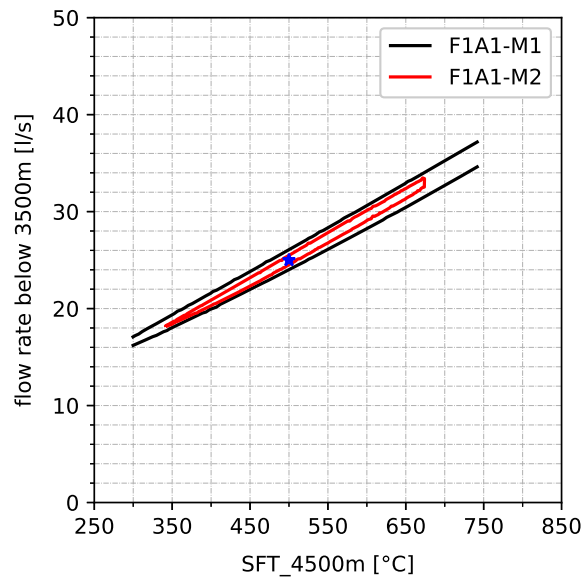


Figure 4.9: Contour lines in the parameter space (bottom-hole SFT and the flow rate below 3500 m) where the following criteria for model F1A1 are satisfied: (1) $RMSE_{thres} = 1.0$ °C (F1A1-M1, black line); (2) the maximum absolute difference between the simulated and the logged temperature for each measurement is 1.0 °C (F1A1-M2, red line). The blue star marks the true values for the SFT (500 °C) and the flow rate (25 L/s).

illustrates that a wrong assumption in the thickness of the geological layers introduces a bias that leads to shifting the acceptable model regions away from the true region. This can be evidenced when comparing the black and red contours of Figure 4.6 with regards to the blue star location. We additionally examined a different layer configuration F2 where the first layer extends to 4000 m (Figure 4.10). Again, the inversion modeling is performed assuming a single geothermal gradient below 2500 m. The solutions, as shown in Figure 4.11, move even further away from the true values of the SFT and the flow rate. It is also worth mentioning that, for a hydrothermal system, fluid advection or convection, or both, can cause variations in the geothermal gradient which cannot be predicted by the conductive model (Schilling et al. 2013). It would be therefore recommended that a comprehensive coupled thermal-hydro model should be studied to predict the temperature distribution of the target area, constrained by temperature measurements from boreholes (Athens and Caers 2019).

Finally, including different types of prior information into the inverse model might also be necessary to limit the boundaries of the model space, especially when dealing with large uncertainties in the joint estimation of the flow rate and the SFT. In practice, this can be done by combining the borehole temperature profiles with other types of borehole measurement data such as flowmeter logs (Molz et al. 1994) that provide information on the rate of flow along depth, or geophysical surveys such as

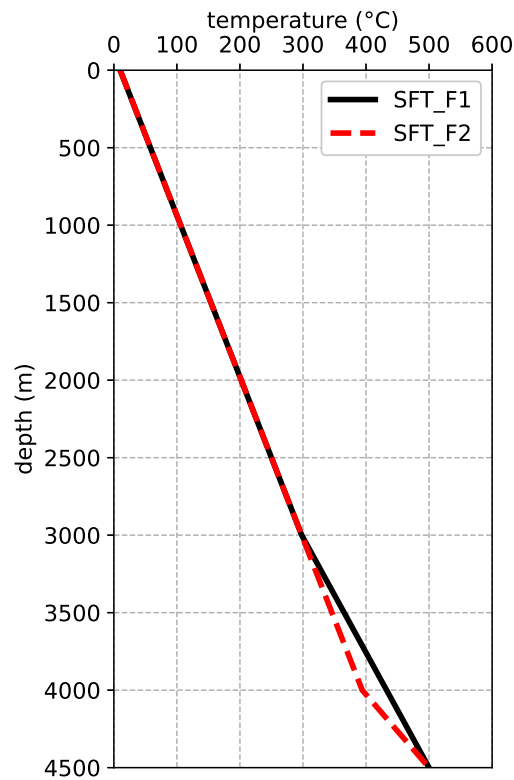


Figure 4.10: The true SFT profiles of formation F1 (black) and F2 (red).

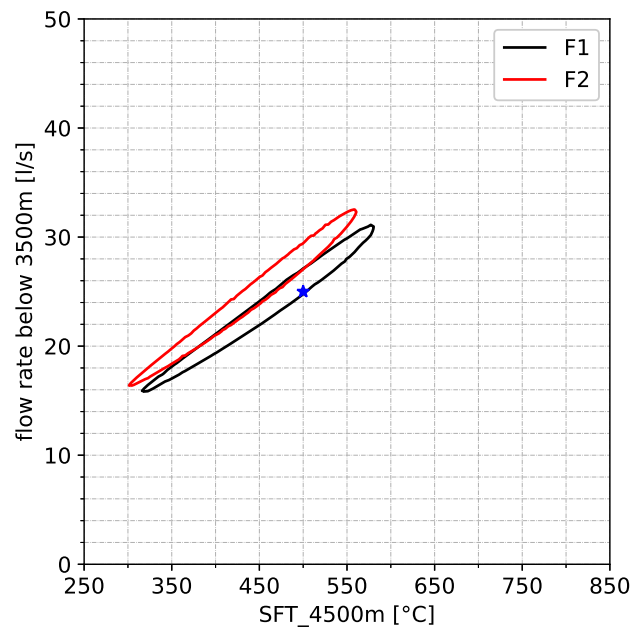


Figure 4.11: Contour lines for $RMSE$ equals $1.0\text{ }^{\circ}\text{C}$ for model F1 (black) and F2 (red) in the model space of SFT at the bottom-hole and the flow rate below 3500 m, when both assuming a constant geothermal gradient for the investigated depth interval between 2500 and 4500 m. The blue star marks the true values for the SFT ($500\text{ }^{\circ}\text{C}$) and the flow rate (25 L/s).

magnetotelluric, gravity, resistivity logs (Hokstad and Tanavasuu-Milkeviciene 2017) and geothermometry data (Ystroem et al. 2020) that can add additional constraints to the in-situ formation temperatures.

4.5 Conclusion

In this paper, a data-driven-based inversion method is performed to analyse the uncertainty of deriving static formation temperatures (SFT) from borehole temperature logs measured under injection conditions. Specifically, the inversion scheme groups the predicted temperature logs from the forward modeling step into two categories, “passing” and “failing”, based on a user-defined misfit tolerance (e.g., root mean squared error) between the predicted and the true temperature values. A k-nearest neighbor machine learning model is then trained as a “classifier” that proposes the most promising sampling points in the model space for each iteration until the optimal prediction of the boundary between the two categories is achieved. Compared with deterministic optimization methods that are used to find one optimal set of parameters, the herein applied method allows simultaneous inversion of all relevant model parameters that lead to model predictions matching equally the predefined quality of the data fitting.

Our study showcases the method’s application in the assessment of multiple factors that influence the accuracy of the solutions for the SFT. For example, the predicted bottom-hole SFT can deviate from the true value by $\pm 2.9\%$, i.e., ± 14.4 °C, when the interpreted temperature log is measured after six hours of injection at 50 L/s with a standard error of 1.0 °C. More generally, it is found that using temperature data acquired under relatively smaller injection rates, or after shorter injection durations, and unarguably, with higher accuracies would improve the quality of the prediction. Additional case studies indicate that the occurrence of flow loss along the well could add strong uncertainties in the determination of the SFT due to the thermal compensation effect between the formation temperature and the flow rate. Hence, integrating prior information, e.g., from other types of measurements such as flowmeter logs or geothermometers, into the inversion modeling would help to reduce such uncertainties. Another option is to consider applying tighter constraints to the misfit between the predictions and the measurements. However, like any misfit criteria, its choice should be justified for instance in regards to the quality of the acquired data.

The current study is based on the assumption that the SFT profile has a piecewise linear shape corresponding to the structure of geological layers, which is most suitable for conductive geothermal systems. Under such conditions, the results show that prior information about the thickness and location depth of the geological layers is necessary to estimate the SFT. If oversimplified assumptions are made due to a lack of such information, the search of the solutions in the model space may be strongly biased towards a wrong direction. On the other hand, for a hydrothermal convection system where conductive heat flow can be disturbed due to the movement of fluids in the formation, a piecewise linear-shape SFT may not be applicable. Nevertheless, a coupled thermal-hydro forward model can still be adapted to the current inversion scheme.

With this work, we demonstrate the promise of applying machine learning techniques for efficient borehole data inversion including uncertainty quantification. Besides the numerical setting of the problem, the performance of any inversion method also relies on the availability and quality of the input data. As discussed herein, the use of more sophisticated logging tools such as distributed temperature sensing to obtain spatially and temporally dense measurements is therefore encouraging. Future work may involve integrating other types of data into the inversion to help to reduce the uncertainty in the estimated parameters or to investigate different parameters in the context of other geophysical applications.

Acknowledgments

The study is partly carried out in the frame of the DEEPEGS “Deployment of Deep Enhanced Geothermal Systems for Sustainable Energy Business” Project within European Union’s Horizon 2020 research and innovation program under grant agreement No. 690771. This study is part of the subtopic “Geoenergy” in the program “MTET - Materials and Technologies for the Energy Transition” of the Helmholtz Association. We also thank the EnBW Energie Baden-Württemberg AG for supporting geothermal research at KIT. We acknowledge support by the KIT-Publication Fund of the Karlsruhe Institute of Technology.

Author contributions statement

JW: developed the workflow of inversion procedure, performed numerical modeling, analyzed the results and wrote the manuscript; FN: supervised and supported the design of the study, reviewed and edited the manuscript; EG: supervised and supported the design of the study, reviewed and edited the manuscript; TK: supervised the research and finalization of the manuscript. All authors read and approved the final manuscript.

Chapter 5

Surrogate-based inversion of borehole logs for formation temperature determination

This chapter is in preparation as Surrogate-based inversion of borehole logs for formation temperature determination, Jia W., Fabian N., Emmanuel G., Thomas K.

Abstract

Temperature logs provide valuable information about the formation temperature distribution, which forms the basis for evaluating the potential of a reservoir for geothermal exploration. This study focuses on inverting temperature logs obtained during fluid injections to determine the static formation temperature (SFT). The inversion scheme is based on the Bayesian inference approach—Markov Chain Monte Carlo (MCMC). To speed up the computational speed of each forward model, surrogate models are trained using artificial neural networks to replace the original high-fidelity numerical models. TMCMC simulations are then performed directly on surrogate models. The inversion workflow is first tested on three synthetic scenarios to validate the proposed method and investigate the effects of circulation loss and measurement noise on the prediction of SFT. Results show that the inversion procedure can reproduce the SFT of a formation with an arbitrary thermal gradient at each depth interval. The occurrence of flow loss zones can potentially lead to an increase in the errors of the SFT estimates at depths below the loss zone. Furthermore, noises in the measured data also have a big impact on the accuracy of predicted SFT. In the second part of the study, the

inversion approach is applied to temperature measurements from the RN-15/IDDP-2 well drilled in the Reykjanes geothermal field. Therein, the SFT around the well below 2500 m is estimated jointly with circulation losses at three loss zones. It is found that the losses can be well constrained from the temperature log, regardless of different assumptions about the distribution of the geothermal gradient. According to the results, the well was drilled under almost complete circulation losses ($> 90\%$) below 3.4 km. On the other hand, estimation of the SFT below 2500 m are subjected to large uncertainty because of the lack of prior information on the geothermal gradient distribution (i.e. uniform or varied in depth). According to the present study, the SFT at the 4500 m is mostly likely to be between $492\text{ }^{\circ}\text{C}$ and $551\text{ }^{\circ}\text{C}$, which is comparable to the published results of other relevant work using different approaches.

5.1 Introduction

Information about the distribution of the initial undisturbed temperature of the sub-surface (i.e., the static formation temperature, SFT) is one of the key aspects of geothermal exploration. The most efficient way to obtain such information is to conduct temperature survey from drilled boreholes. So far, most applied approaches to determine the SFT have focused on the interpretation of temperature data measured during the so-called shut-in periods, where the borehole is filled with a static fluid column. However, applying these methods can face several challenging aspects, such as the justification of thermal equilibrium condition between the formation and the fluid (Talalay et al. 2020), the necessity of temperatures corrections to account for thermal disturbances introduced from fluids to the surrounding formation (Bullard 1947; Andaverde et al. 2005; Bassam et al. 2010; Wong-Loya et al. 2012) and the interfere of the convective mixing of the fluid which can cause either over- or under-estimation of the SFT (Luheshi 1983; Wang et al. 2019). Due to the uncertainties inherent in the physical process, several studies have found significant estimation errors for the SFT when simplified analytical models were applied due to their unrealistic assumptions for the drilling phase and incorrect use of linear regression models (Espinoza-Ojeda and Santoyo 2016; Andaverde et al. 2005). Other challenges come from the economic, technical, and safety aspects of conducting temperature measurements during shut-in, especially for very hot and deep boreholes. For example, extra high cost for conducting measurements over a large time span of shut-in periods; the risk that the recovered temperatures exceed the limits of measuring devices which are mostly under $300\text{ }^{\circ}\text{C}$ and safety concerns about casing failures (Kruszewski and Wittig 2018).

On the other hand, multiple studies have been focused on using temperature logs measured under dynamic injection to assess borehole conditions. One important aspect is to use temperature measurements to infer flow conditions in the well. Examples for such kind of application are: Meyzonnat et al. (2018) used high-resolution temperature measurements to characterize borehole inflow intensities and provide information about the distribution of hydraulic properties with depth; Vidal et al. (2019) identified the occurrence and the positions of fracture zones in wellbores; Klepikova et al. (2011, 2014) applied numerical modeling method to determine the inflow rate at the location of the fractures. The success of these applications (mostly in the field of geo-hydrology) also encourages the use of temperature logging data to characterize the circulation loss, which is very commonly occurred during drilling in geothermal exploration wells (Xu et al. 2019; Allahvirdizadeh 2020).

In a previous work, Wang et al. (2021) performed a numerical study on the uncertainty in estimating the SFT from temperature measurements. The initiative for the study stems from the RN-15/IDDP-2 deep geothermal well drilled as part of the Icelandic Deep Drilling Project (IDDP) in search of supercritical resources at depth deeper than 4 km to increase power generation in the Reykjanes field. To evaluate the energy potential of the geothermal well, knowledge of the formation temperature is a prerequisite. Temperatures measured in the well (maximum 426 °C) confirm the extremely hot downhole environment but are expected to be still far from the thermal equilibrium state (SFT) because the well was under injection conditions during the logging to cool the casing and measuring equipment (Friðleifsson et al. 2020). During drilling, severe circulation losses occurred at several depths below 3 km, but the amount of these losses was unclear. Given the acquisition of shut-in temperature data is a difficult endeavor for such a hot geothermal well, Wang et al. (2021) proposed the analysis of temperature data measured from injection conditions for SFT determination. Therein, a deterministic method was employed to search all possible solutions in the parameter space that result in the same discrepancies between the model prediction and the true borehole fluid temperatures. These discrepancies are presumably associated with several uncertainty factors, such as different injection conditions (e.g., flow rate and injection duration), flow loss zones, measurement errors, lack of prior information, etc. However, a generic approach to reduce the uncertainty of the model parameters (i.e., SFT) by conditioning on temperature measurements is still missing. To bridge such a gap, a Bayesian probabilistic approach is applied in this study to solve the SFT by inverting injection temperature logs.

Over the past decades, the Bayesian inversion framework has gained great popularity

due to its advantages in the possibility of introducing prior knowledge into the analysis, better accuracy when facing noisy data, and the intuitiveness and straightforward interpretation of results (Makowski et al. 2019). This study focuses on the mainstream Bayesian inference approach-Markov chain Monte Carlo (MCMC) which has been widely used to solve hydrological (Smith and Marshall 2008; Raje and Krishnan 2012; Sun et al. 2013) and geophysical Hong and Sen (2009); Hansen and Cordua (2017); Grana and Della Rossa (2010); Spikes et al. (2007) inverse problems. However, a challenge often encountered when applying MCMC is the large number of model evaluations required, especially when the dimension of the model increases or when facing strongly nonlinear problems. In case a single forward model is already CPU intensive, then the computational cost of MCMC simulation will become prohibitive.

To alleviate the computational burden, one can take advantage of surrogate models. A surrogate model (also named reduced-order model, proxy model, low-fidelity model, etc.) can be viewed as a simple analytical model that mimics the input/output behavior of complex systems (Smith and Marshall 2008). Compared to the high-fidelity model, a surrogate model can obtain similar (while less accurate) model outputs at a much lower computational cost. In this study, the surrogate models are constructed using artificial neural networks (ANN) which has been widely used for system response prediction, classification, and function approximations in various fields of studies. Due to its high capability of solving non-linear and high-dimensional problems, ANN has also been extensively employed in the study of subsurface systems. For example, Zhou et al. (2019) predicted the production temperature of an enhanced geothermal system, Bassam et al. (2010) derived relationships between the SFT and the transient borehole temperatures during thermal recoveries using field temperature database, Pan et al. (2014) optimized the CO₂ storage in a saline aquifer and achieved satisfactory results compared with the solutions obtained by the computationally exhausted simulator.

The structure of this manuscript is organized as follows. First, the concept of artificial neural networks and the Bayesian inversion framework are introduced. Then the inversion workflow is performed on synthetic temperature logs that are generated with different assumptions about the accuracy of the logging data and the occurrence of circulation loss zones in the well. The influence of measurement error and flow loss on the estimation of SFT is then discussed accordingly. Next, the approach is applied to a real-world case where an injection temperature log was used to estimate the SFT along with the amount of loss at those flow loss zones below 3 km for the RN-15/IDDP-2 well. For this well in particular, the SFT below 2500 m is already known (Chapter 5.4.2). Without knowing how the SFT profile will continue to develop

below 2500 m, two different assumptions are made for the distribution of geothermal gradient at depth. One is that the temperature gradient is constant; the other is that the formation consists of multiple layers, where the thermal gradients are constant within each layer but may vary between the layers. Finally, some discussions and conclusions are provided in Chapter 5.5.

5.2 Method

The inversion scheme consists of two sequential steps, namely, surrogate modeling using ANN and the MCMC simulation. These two steps are performed using the open source code RAVEN, which supports different types of machine learning techniques developed internally and implemented via the external Python library–scikit-learn (Alfonsi et al. 2016). Each steps are described in detail below. All data set used to build the surrogate models are generated by running an in-house borehole simulator (the so-called high-fidelity model), developed based on a multiphysics simulation framework MOOSE (Gaston et al. 2009). Details of the simulator and the solved system equations can be found in Wang et al. (2019).

5.2.1 The artificial neural network

The first step of the inversion is to create a surrogate model using ANN. An ANN model can be considered as a mathematical model of an arbitrary mapping between two spaces. It consists of several layers with each layer containing a number of unit cells called neurons. Each layer is an intermediate step in successive transformations between the input and output space and has an associated transfer function, and each neuron has an associated bias. By optimizing the free parameters of the mathematical model, during a so-called training process, the mapping can be modified to represent the desired relation.

We adopt the most widely used ANN, the so-called multi-layer perceptron (MLP) which is a feed-forward neural network trained by the error back-propagation learning algorithm. Figure 5.1 shows an MLP that consists of input, hidden and output layers. The neurons of each layer are connected by three layers of free parameters (weights and bias) that are represented by lines. In our context, the ANN model is

trained to predict the temperature distribution of the borehole fluid at the time of the measurement. The neurons in the input layer represent the parameters that control the borehole temperatures, i.e., the SFT (or the geothermal thermal gradients) at depths and the flow rate(s) below the loss zone(s). The output layer contains N number of neurons representing the temperatures at different measuring depths. As such, the n-th borehole temperature T_n can be expressed as a function of both the input parameter x , the weight (w), and the bias (b) as follows:

$$T_n = g \left[\sum_k^K w_{kn}^{(3)} h_k^{(2)} + b_n^{(3)} \right], \quad (5.1)$$

where $g(\cdot)$ represents the so-called activation function for the output neurons. Common choices for the activation functions are the logistic and hyperbolic tangent functions. We use the latter in this work, because symmetric sigmoids, such as the hyperbolic tangent, often display better convergence properties during network training. $w_{kn}^{(3)}$ are the weights applied to the third layer. $h_k^{(2)}$ is the k-th component of the K neurons on the second hidden layer that can be derived by a series of matrix multiplication and transformation using the activation function $g(\cdot)$:

$$h_k^{(2)} = g \left[\sum_j^J w_{jk}^{(2)} g \left[\sum_i^I w_{ij}^{(1)} x_i + b_j^{(1)} \right] + b_k^{(2)} \right], \quad (5.2)$$

where $w_{ij}^{(1)}$ and $b_j^{(1)}$ are the weights and biases applied to the first hidden layer, and $w_{jk}^{(2)}$ and $b_k^{(2)}$ are the weights and biases applied to the second hidden layer, x_i is the i-th neuron of the input layer.

The number of neurons on the hidden layers can affect the performance of the ANN model. Several methods can be adopted to determine the appropriate number, such as trial-and-error, systematic hyperparameters tuning using grid search and random search (Pontes et al. 2016), or the empirical-formula approach (Bowden et al. 2005).

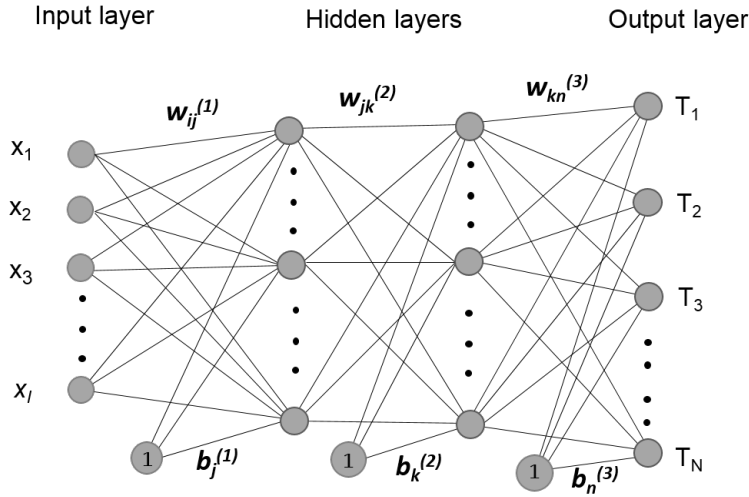


Figure 5.1: A three-layer feed-forward Multilayer Perceptron (MLP) model. I number input neurons are feed into the network. The two hidden layers which contain J and K number of neurons, respectively, perform nonlinear transformations of the inputs (i.e., by multiplying their associated weights, w) to the N number of outputs.

In surrogate modeling, the ANN model is first trained to have prediction capability using the training set and then tested on newly generated samples, called the test set. If the prediction accuracy is not within an acceptable range, then the training data or the surrogate model must be modified for training again until a satisfactory model is developed. The root mean square error (RMSE) is used to evaluate the accuracy of temperature prediction, which is calculated as follows:

$$RMSE_n = \sqrt{\frac{1}{M} \sum_{m=1}^M (T_{p,n}^m - T_{t,n}^m)^2}, \quad (5.3)$$

where $RMSE_n$ is the RMSE value for the temperature at the n-th measuring depth, M is the number of samples of the training or test data set, the subscripts p and t denote the predicted temperature by the surrogate model and the true temperature (i.e simulated by the borehole simulator), respectively.

5.2.2 MCMC method

Herein, the borehole thermal model can be expressed using the form:

$$\mathbf{T}_{obs} = TM(\mathbf{X}) + \boldsymbol{\varepsilon}, \quad (5.4)$$

where $TM(\cdot)$ denotes the high-fidelity thermal model that predicts the borehole temperatures given input parameters $\mathbf{X} \in \mathbb{R}^{I \times 1}$. Since a large number of evaluations of $TM(\mathbf{X})$ are needed in the MCMC simulation, $TM(\cdot)$ is replaced by the ANN surrogate model from the previous step. $\mathbf{T}_{obs} \in \mathbb{R}^{N \times 1}$ is a vector for the borehole temperature measurements with random error $\boldsymbol{\varepsilon} \in \mathbb{R}^{N \times 1}$. Our prior knowledge about \mathbf{X} is represented by $p(\mathbf{X})$. According to Bayes' theorem, such prior knowledge can be updated with the observed data, \mathbf{T}_{obs} , by considering the following:

$$p(\mathbf{X}|\mathbf{T}_{obs}) = \frac{p(\mathbf{X})p(\mathbf{T}_{obs}|\mathbf{X})}{\int p(\mathbf{T}_{obs}|\mathbf{X})p(\mathbf{X})d\mathbf{X}} \propto p(\mathbf{X}) \cdot \mathcal{L}(\mathbf{X}|\mathbf{T}_{obs}), \quad (5.5)$$

where $p(\mathbf{X}|\mathbf{T}_{obs})$ is the posterior distribution, $\mathcal{L}(\mathbf{X}|\mathbf{T}_{obs})$ is the likelihood function, and $\int p(\mathbf{T}_{obs}|\mathbf{X})p(\mathbf{X})d\mathbf{X}$ is a constant term which is referred to as marginal likelihood. Assume that the measurement errors are independent and follow normal distribution, i.e., $\boldsymbol{\varepsilon} \sim N(0, \boldsymbol{\sigma}^2)$, the log likelihood function can be given by:

$$\mathcal{L}_{log}(\mathbf{X}|\mathbf{T}_{obs}) = -\frac{N}{2} \log 2\pi - \sum_{i=1}^N \frac{(\mathbf{T}_{obs,i} - TM_i(\mathbf{X}))^2}{2\sigma_i^2} - \sum_{i=1}^N \log \sigma_i, \quad (5.6)$$

where i indicates the i -th component of the measurement. If the distributions of measurement errors are not known, the following form of the log likelihood function can be used (Vrugt 2016):

$$\mathcal{L}_{log}(\mathbf{X}|\mathbf{T}_{obs}) = -\frac{N}{2} \log \left\{ \sum_{i=1}^N |\mathbf{T}_{obs,i} - TM_i(\mathbf{X})|^2 \right\}, \quad (5.7)$$

For non-linear, high-dimensional problems, $p(\mathbf{X}|\mathbf{T}_{obs})$ can not be solved directly and is often approximated by numerical techniques, e.g. MCMC.

MCMC is a stochastic simulation method where samples are generated consecutively from a so-called proposal distribution and that the current sample depends only on the states of the previous samples. After a sufficient number of steps (burn-in period), the chain will have a unique stationary distribution, which is the demanded posterior distribution of model parameters. In the following, the implementation steps of MCMC using the Metropolis-Hastings algorithm is described:

1. Generate an initial model with \mathbf{X}_0 from th prior distribution $p(\mathbf{X})$.
2. Continue to generate samples such that each current sample, \mathbf{X}_{cr} , is drawn from a proposal distribution $q(\mathbf{X}_{cr}|\mathbf{X}_{pr})$ conditioned on the previous sample \mathbf{X}_{pr} .

3. The acceptance rate which determines the probability that we accept \mathbf{X}_{cr} is calculated as follows:

$$r = \min \left[1, \frac{p(\mathbf{X}_{cr} | \mathbf{T}_{obs})}{p(\mathbf{X}_{pr} | \mathbf{T}_{obs})} \right]. \quad (5.8)$$

4. Compare r with a random number, u , draw from uniform distribution, i.e. $u \sim U(0, 1)$. If $u < r$, \mathbf{X}_{cr} is accepted, otherwise, \mathbf{X}_{cr} is rejected.
5. Repeat steps 2-4 until the maximum iteration number is reached.

5.3 Analysis of synthetic scenarios

Firstly, synthetic numerical models are designed to test the capability of the proposed inversion method. In the general model setup (see Figure 5.2a), a 2-D domain consisting of a borehole with a radius of 0.11 m and a non-permeable formation with a vertical extension of 4500 m and lateral of 50 m is simulated. The formation is considered to have five layers with the same thickness (900 m). It should be noted that the layers are subdivided according to the geothermal gradient, hence they are referred to as "geothermal layers" in this study. The SFT is applied as both the initial condition and the Dirichlet boundary condition at the right edge of the formation. Each layer has an arbitrary geothermal gradient, α . Herein, we assume the five thermal gradients are equal (0.06 °C/m, Figure 5.2b).

Three scenarios are then designed to investigate the impacts of measurement noises and the presence of flow loss zones on the estimation of SFT. In the reference case, no flow loss occurs in the borehole and the temperature log is measured without any error. In case 1, no flow loss occurs and the temperature measurements have random errors that follow a normal distribution (i.e. $\sim N(0, 1)$ °C), and in case 2, 20% of the flow is lost from the well to the formation at 3500 m and the temperature log is measured with no error. For each scenario, a synthetic temperature log is simulated with an injection flow rate of 50 L/s at the well-head after an injection duration of three hours. Forty data points are sampled for each log, these logs are presented in Figure 5.2c. Next, the inversion procedure is performed to estimate the relevant parameters, i.e., the five thermal gradients for all cases and the flow rate below the loss zone for case 2.

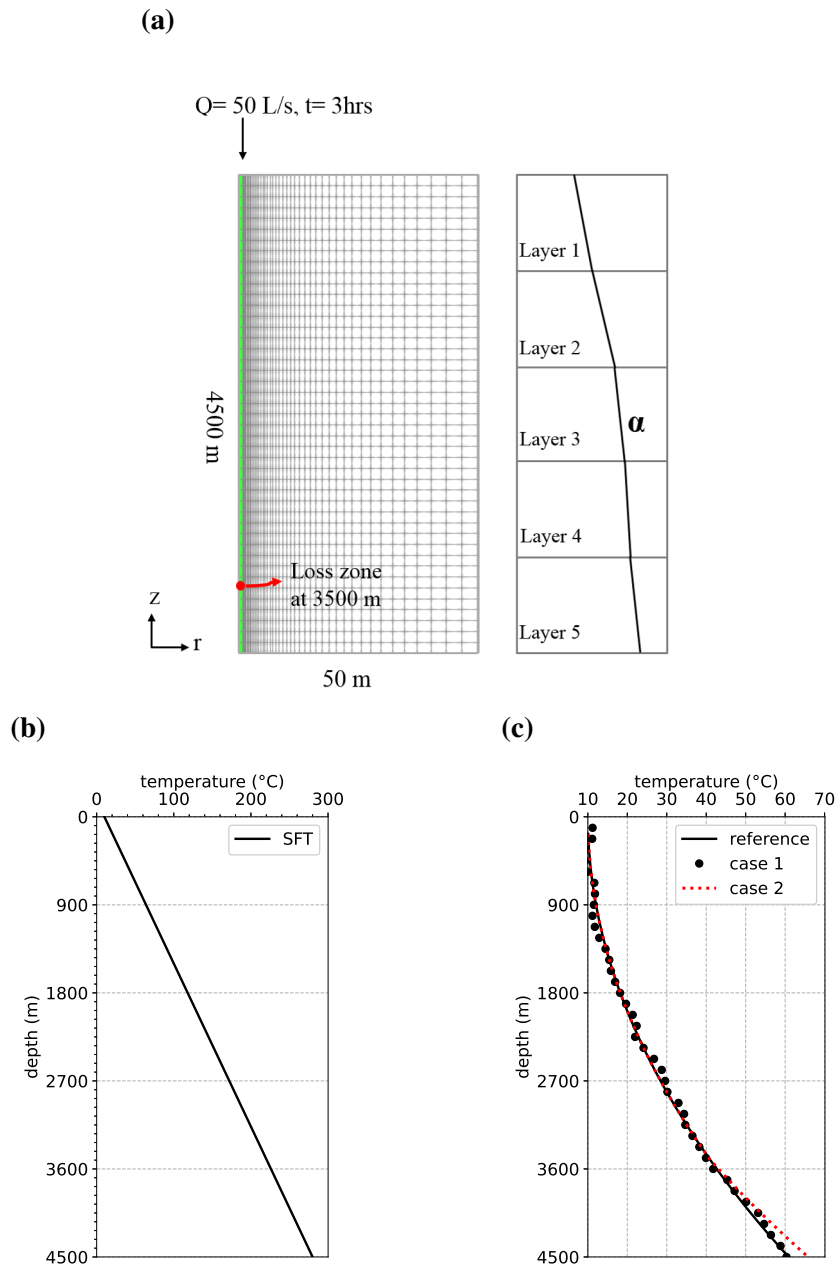


Figure 5.2: (a) Schematic of the simulation set-up with the boundary and initial conditions. Depends on the scenario, a flow loss of 20% may occur at 3500 m. (b) The SFT profile when assuming the five layers have the same thermal gradient. (c) Synthetic temperature logs for different scenarios: no flow loss occurs and the temperature log is measured with no error (reference, solid line), no flow loss occurs and temperature measurements have random error of $\sim N(0, 1) \text{ }^{\circ}\text{C}$ (case 1, black dot line), 20% flow is lost into the formation and the temperature log is measured with no error (case 2, red dash line).

5.3.1 Surrogate models

Two surrogate models are trained for the three scenarios described above. In one model (S1), the input layer of the ANN consists of the five neurons which represent the thermal gradients. In another model (S2), one additional parameter – the remaining flow rate ratio below 3500 m – is added to the input layer. To generate training data for the surrogate models, the borehole simulator is run repeatedly to predict the borehole temperatures from different combinations of input parameters (five thermal gradients and the remaining flow below 3500 m) using the Latin Hypercube sampling (LHS) technique, which is more efficient and less time consuming to achieve sufficient model accuracy compared to the conventional Monte Carlo sampling (Atangana 2017). The same procedure is repeated for generating the test data, only that the size of the test data is 1/4 of the training data.

As the accuracy of a surrogate model can be affected by the size of the training sample and the number of inputs, a sensitivity analysis of the variation of the RMSE is performed. The maximum RMSE for the temperature predictions at different depths in the test set is plotted against the size of the training sample on a semi-logarithmic grid (Figure 5.3). The minimum training sample size is 100. Not surprisingly, the accuracy of each surrogate model increases with increasing sample size. S1 is a simpler model to train, as the maximum RMSE is already quite low (0.08 °C) using training 100 samples. Therefore, it is decided that no further analysis needs to be done for S1. To achieve the same accuracy as S1, 700 training samples are required for S2. This indicates that the change of flow rate along the borehole (i.e., due to drilling loss) could cause much more difficulties when predicting the temperature response in the borehole using a simpler (compared to the high-fidelity model) mathematical model. In this study, the finally determined training sample size for S1 and S2 are 100 and 700, respectively. After tuning the hyperparameters, two hidden layers with each layer having the same number of neurons are adopted for both models, and the number of neurons on each hidden layer are 20 for S1 and 30 for S2.

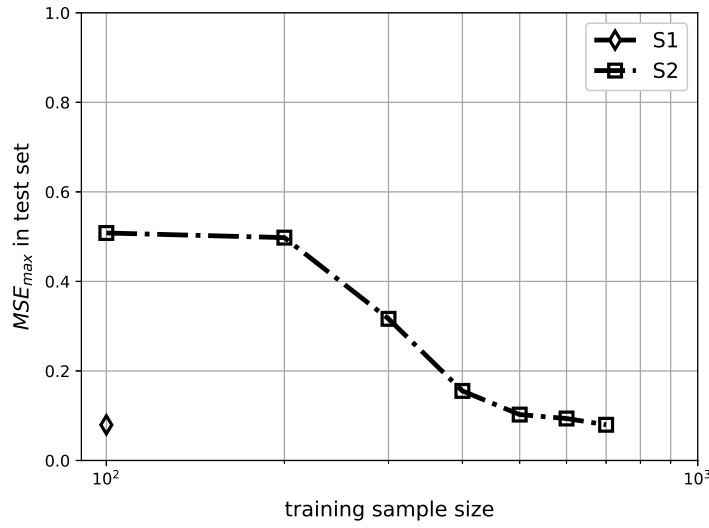


Figure 5.3: Sensitivity of the maximum approximation error ($RMSE_{max}$) in the test set to the training sample size for model S1 and S2.

5.3.2 Inversions of temperature logs

The SFT profile for each designed case is then estimated by performing MCMC on its corresponding surrogate model. In fact, it is the thermal gradients for the five layers to be predicted. For the MCMC process, normal distributions (whose standard deviation can control the closeness of adjacent samples) are assumed for the proposal probabilities of the unknown parameters. The standard deviation of these proposal probability functions are selected to ensure that the acceptance rates range between 25–45% to achieve good convergence rates for the parameters (Albert 2009; Bedard 2008). Convergence is considered to be reached when the resulting posterior distribution would not modify when adding more samples. In the end, 5e5 samples are drawn from the chain with the first 1e5 samples being discarded (burn-in length). The marginal posterior probability distributions (PPDFs) of the five thermal gradients are transformed to the marginal PPDFs of the equivalent SFT values at the bases of the five layers.

Results for the reference case are displayed in Figure 5.4. It can be seen, when the inverted temperature data are accurate and the flow rate is constant along depth (i.e., no loss occurs), the 95% confidence interval of the PPDF of each SFT estimate captures the ground truth (real SFT value). The maximum prediction error (i.e., the deviation of the left and right bound with respect to the true SFT) is found to be less than 0.3 °C, which is below the typical errors of temperature measurement devices

($> 0.5\text{ }^{\circ}\text{C}$) (Cao et al. 1988; Förster 2001). However, once temperature data with random noises are used to invert the SFT (case 1), the 95% confidence zone becomes much wider for all the SFT estimates than those in the reference case (figure 5.5). The quality of the prediction in each layer can also be different. The uncertainty range of the confidence interval varies between about 29 ° and $57\text{ }^{\circ}\text{C}$. For the SFT estimate at each layer base, the maximum estimation error ranges from 16.6 ° to $47.2\text{ }^{\circ}\text{C}$ and the minimum error from about 0 ° to $16\text{ }^{\circ}\text{C}$. In addition, bias in each estimate can be found as the maximum PPDF solution (optimum estimation) deviates from the true solution (the deviations are between $6\text{ }^{\circ}\text{C}$ and $33\text{ }^{\circ}\text{C}$). Furthermore, the noises lead to different biases in the best estimated SFT values (highest posterior probability) for different depths. This suggests that a deterministic approach such as least squares fitting should be used with caution when inverting temperature measurement data, since the SFT profile leading to the least fitting error may be very different from the truth. For example, the best estimated SFT profile has a maximum local prediction error of $39.4\text{ }^{\circ}\text{C}$ (percent error: 14%) which occurs at the bottom-hole depth in case 1.

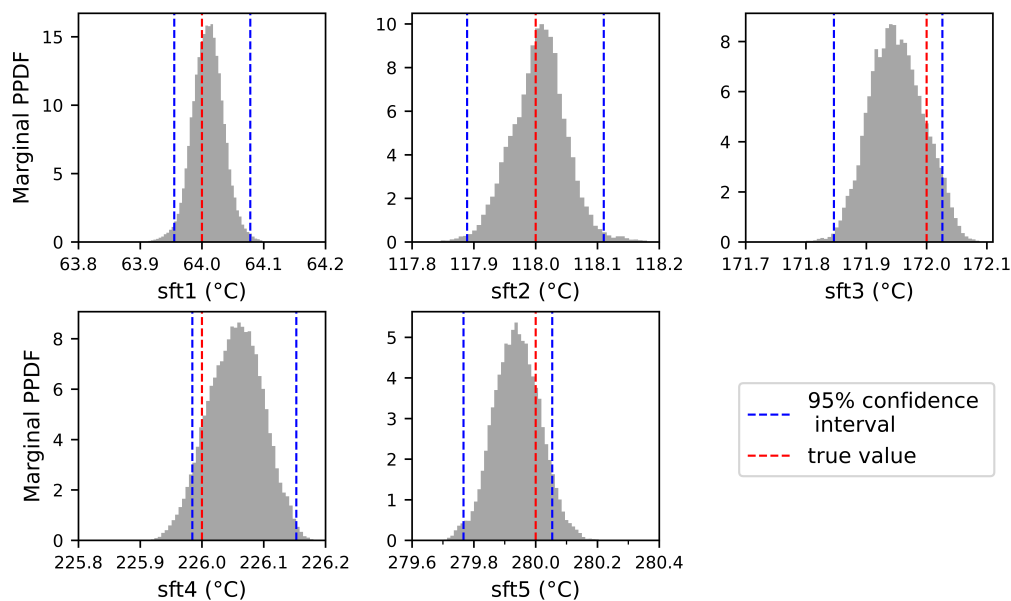


Figure 5.4: Marginal PPDF for the SFT (sft1–sft5) at the base of each layer in the reference case. The true value and the 95% confidence interval are marked with the black and green dash line, respectively.

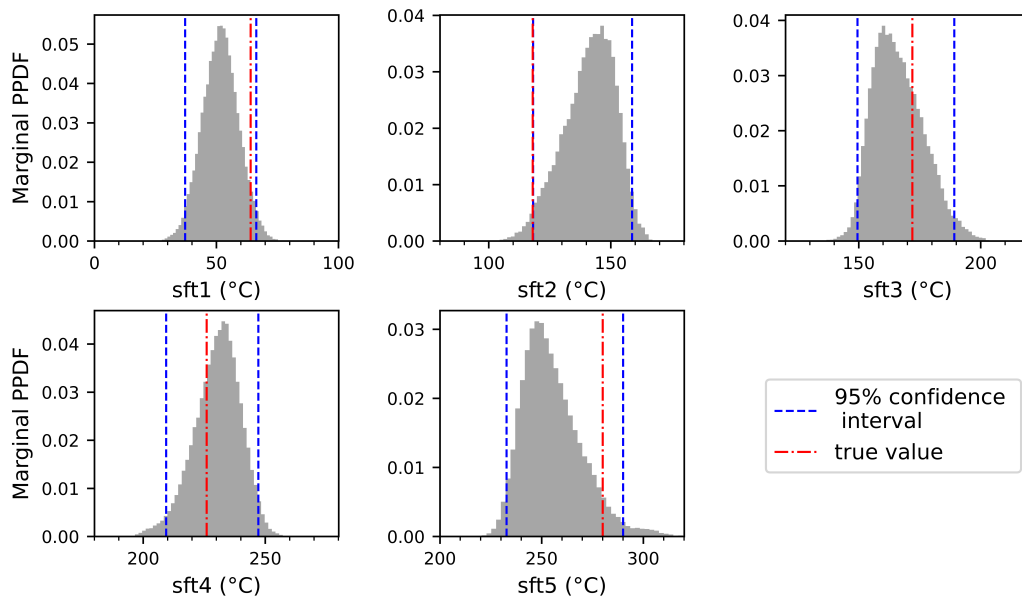


Figure 5.5: Case 1: marginal PPDF for the SFT at the base of each layer.

Since case 2 has one more estimation parameter (the remaining flow rate below 3500 m) compared to the other two cases, the inversion procedure is performed using S2. Figure 5.6 displays the marginal PPDF of each parameter. Compared to the reference case, the 95% confidence interval for the SFT value at the bottom depth of each layer are generally wider, especially for the last two layers. Nevertheless, the accuracy of the estimates at the base of each layer is still satisfactory. For the upper three layers, the prediction errors are within $0.5\text{ }^{\circ}\text{C}$. Uncertainties in the SFTs of the last two layers are slightly larger: the maximum prediction error of the 95% confidence interval is about 1.0 and $2\text{ }^{\circ}\text{C}$ for the SFT at the base of the fourth and fifth layer, respectively. Finally, the remaining flow rate below the loss zone is also accurately estimated: the maximum error in the confidence interval is only 0.2 L/s (0.5%). Considering that the two surrogate models, S1 and S2, have almost the same accuracy, the differences in the four estimates between the case 2 and the reference case are probably not due to the approximation error of the surrogate models, but are related to the presence of the flow loss zone, which locates within in the fourth layer. Because both flow rate and formation temperature will affect the borehole temperature, but their impacts can be compensated. Namely, an increased borehole temperature can be caused by either a reduced flow rate (i.e. more time for heat exchange with the surrounding formation) or an increased formation temperature. Conversely, a decreased well temperature due to an increased injection rate may be offset by a decreased formation temperature. As a result, a wider range for the combinations of flow rate and SFT can provide very close fitting accuracy of the logging data. Therefore, for depths below the loss zone, larger uncertainties in the SFT estimates are expected. Indeed, according to Figure

5.6, the marginal PPDFs for the last two layers are wider than those for the upper three layers.

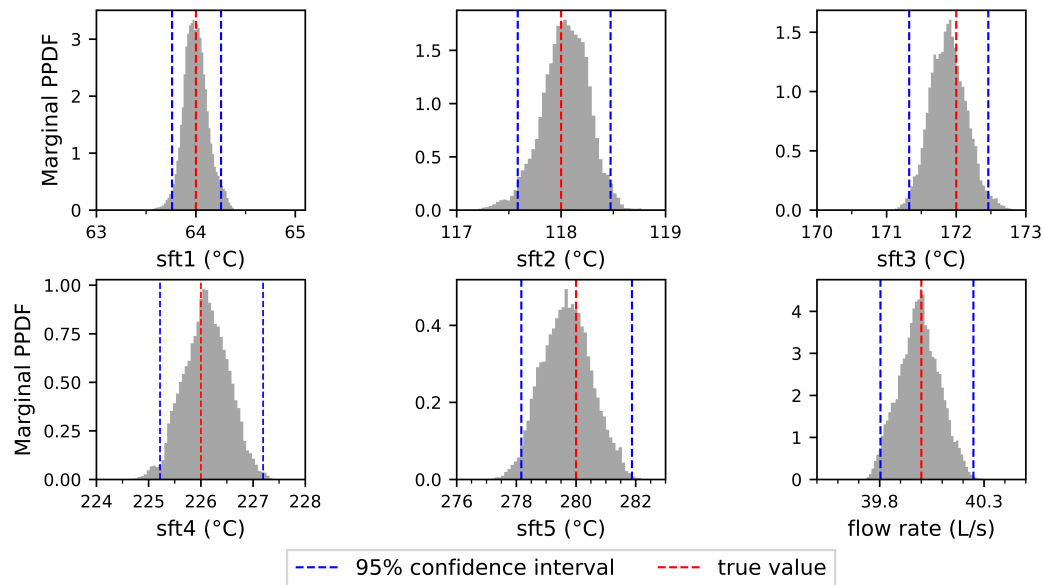


Figure 5.6: Case 2: marginal PPDF for the SFT at the base of each layer and the remaining flow rate after the loss zone at 3500 m.

5.4 Application to the temperature log from the RN-15/IDDP-2 well

5.4.1 The RN-15/IDDP-2 well

In this section, the inversion workflow is applied to a real-world case where the SFT is to be estimated for the exploration well RN-15/IDDP-2 located in the Reykjanes, Iceland. The Reykjanes geothermal system is characterized by convective heat transport in the reservoir down to a depth of about 2500 m, apart from heat conduction at some shallower depths (Franzson et al. 2002; Friðleifsson et al. 2020). This is seen from temperature profiles of several wells measured under the steady state of thermal recoveries. Figure 5.7a (red line) shows the SFT profile for the old RN-15 well derived from direct temperature measurements during a maintenance stop in 2010 (Jónsson et al. 2010). Evidently there is a large section of the formation in which convection exists, lifting high-temperature fluids close to the surface and influencing

the near-surface gradient. For example, the formation temperature increases rapidly to 270 °C at 1 km depth. However, it increases by only 17 °C at 2500 m depth.

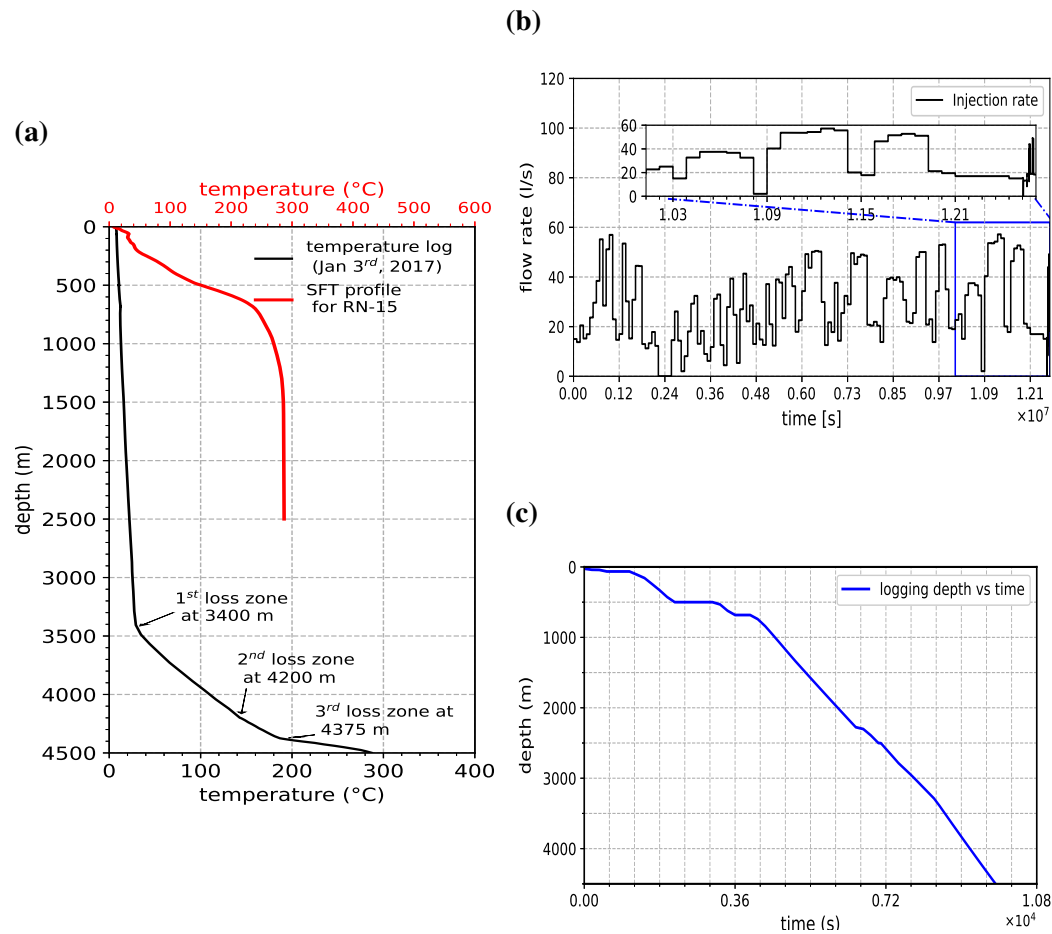


Figure 5.7: (a) The SFT profile in the upper 2500 m around the RN-15 (red line); and temperature log of RN-15/IDDP-2 measured on January 3rd, 2017 (black line) with circulation loss zones indicated. (b) The flow history at the well-head from the start of drilling to the end of the temperature logging. The upper zoom plot shows the flow history on the day of the logging. (c) The change of the temperature measuring depth with time (0 equals when the logging starts) during the downward trip of logging device.

The drilling phase (from August 11th, 2016 to January 25th, 2017) of the RN-15/IDDP-2 involves deepening the RN15 (2500 m deep) into a new well - IDDP-2 - with a final depth of 4659 m. The first temperature log that ran almost to the bottom-hole depth was conducted on January 3rd, 2017 (on workday 146). The highest temperature measured was 426 °C at the bottom of the well at a fluid pressure of 340 bar, indicating supercritical reservoir conditions. However, it is unlikely that these measurements reflect the true formation temperature because they were obtained under injection conditions and the formation temperature was perturbed from the initial condition. Several loss zones (kick-off points) were detected from this temperature log, the

largest loss zone was located at around 3400 m and several minor loss zones were found at 4200 m, 4375 m, and 4500 m (Weisenberger et al. 2017). In the case study, this temperature log was inverted for estimating the SFT around the RN-15/IDDP-2 until 4500 m (Figure 5.7a, black line). The thermal modeling of this log takes into account the well geometry and completion which are given in Table 5.1. The highly fluctuated injection flow rate at the well-head was averaged daily for working days 1-145 and every ten minutes on the day of logging (Figure 5.7b). Unlike the instantaneous recording at all depths for the synthetic temperature logs in Chapter 5.3, the measuring of this log lasted about three hours because of the tripping of the logging device. Therefore, the simulation also incorporated the spatial-temporal function for the temperature recording (Figure 5.7c).

Depth (m)	Casing	Diameter (")
84.4	Surface casing	22 1/2
292.8	Anchor casing	18 5/8
793.8	Production casing 1	13 3/8
2932.4	Production casing 2	9 5/8
4563	Perforated liner	7

Table 5.1: Geometry and completion of the RN-15/IDDP-2 well (referenced to the ground surface)

5.4.2 Estimation of the SFT below 2.5 km and fluid losses

In the following, the SFT between 2500–4500 m as well as the amount of the circulation loss (in percentage) at three depths (3400 m, 4200 m, 4375 m) are jointly estimated. Since there is no prior knowledge about the shape of the SFT below 2500 m, two different hypotheses about the SFT profile are made and the inversion results are then compared to investigate the impact of different model assumptions. In one hypothesis, the thermal gradient is constant. In another, the formation consists of multiple layers where the thermal gradient of these layers can be different from each other. For simplicity, the layers are considered to have equal thickness and the number of these layers is assumed to be five in the present investigation.

5.4.2.1 Surrogate models

As confirmed from the previous synthetic study, the accuracy of the surrogate model depends both on the complexity of the problem (number of input parameters) and the number of samples used to train the model. To reduce the computational cost of obtaining a sufficient number of training samples, it makes sense to remove those unrealistic ranges of parameter values during the sampling phase and make the prior more informative. According to Wang et al. (2019), the magnitude of change in the thermal gradient downstream of a zone with flow loss can be very sensitive to the relative loss ratio, defined as the ratio between the amount of flow lost at the loss zone and the amount of flow above the loss zone. Therefore, pre-selection of plausible ranges for the amount of flow loss can be made relatively easily by visual inspection of thermal gradients from temperature measurements. As an example, 200 prior model realizations are generated using LHS. The distribution of the simulated borehole temperatures suggests that the prior range of the relative loss at 3400 m can be set between 80% and 100% (Figure 5.8). Referring to the reported geothermal thermal gradient values in Iceland (Flóvenz and Saemundsson 1993; Kranz 2006), the prior distribution of geothermal gradient of each layer is assumed to be between 0 and 200 °C/km.

Because of the different hypotheses we have about the distribution of the thermal gradient with depth, two groups of forward simulations, one with four parameters and the other with eight parameters, are generated to train two surrogate models, M1 and M2, respectively. For both surrogate models, the input layer contains three neurons representing the three relative loss ratios at 3400 m, 4200 m, and 4375 m. In addition, the input layer of M1 has one more neuron representing the thermal gradient between 2500 and 4500 m. M2 has five additional neurons, representing the thermal gradients of the assumed five layers, in its input layer. The output layer in both models contains forty-four neurons which are the measured borehole temperatures at forty-four different depths.

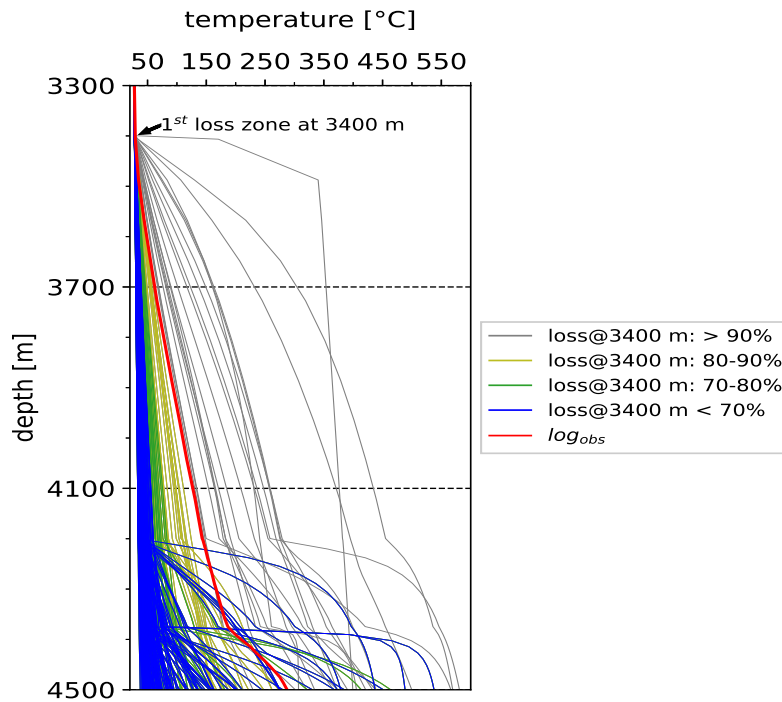


Figure 5.8: 200 prior realizations of borehole temperature profiles and the observation temperature log (log_{obs} , red line). The profiles are shown in different colors corresponding to four different ranges of the relative flow loss at the first loss zone (3400 m): > 90%, 80-90%, 70-80%, < 70%.

Again, a sensitivity analysis is performed to determine the number of training samples that can be used to achieve sufficient accuracy of the surrogate model. The minimum number of samples tested to train M1 and M2 are both 1000. According to Figure 5.9, M1 is more accurate than M2 when the number of training examples is less than 4000. This is to be expected because M2 has twice as many input variables as M1, so it is more difficult to predict the system response for M2 compared to M1. However, the difference in model accuracy seems to be the most significant when the sample size is smaller than 2000 (the maximum difference is around 1.3 °C). As the training sample size increases, such difference decreases until it becomes very small when the training samples exceed 4000. This suggests that the difficulties in predicting temperatures at different depths for the surrogate model caused by temperature gradients varying with depth would decrease as the size of the training sample increases.

M1 and M2 are trained until the RMSE of the temperature prediction for each measuring depth drops below 0.5 °C. The reason for choosing 0.5 °C as the threshold value is that it is smaller than the typical errors of the temperature measuring devices (Förster 2001). To obtain an RMSE less than 0.5 °C, M1 and M2 need to use at least 8000 training samples, which are significantly larger than those required to train S1 and S2,

which are less than 100 (see Figure 5.4). Such observation seems to contradict the fact that S1 and S2 have more input variables (i.e., input neurons) than M1. This could be due to that the training data for M1 and M2 are provided by the RN-15/IDDP-2 thermal model, which is more complex than the synthetic thermal model introduced in Chapter 5.3 (i.e., due to the varying injection flow rates and different measuring times for temperature at different depths, a higher number of flow loss zones, etc). In particular, the three flow loss variables in M1 and M2 may cause the cost of training a relatively accurate model to increase significantly compared to S1 and S2. This can be inferred from the previous finding that S2 requires approximately seven times the size of the training sample to achieve the same accuracy as S1 due to the presence of only one additional flow loss variable. The maximum values of RMSE for temperature prediction are $0.49\text{ }^{\circ}\text{C}$ for M1 and $0.50\text{ }^{\circ}\text{C}$ for M2, whereas RMSE values for most depths are less than $0.1\text{ }^{\circ}\text{C}$. Two hidden layers are used for both M1 and M2. After tuning using grid search, the final number of neurons per hidden layer was set to 60 and 70 for M1 and M2, respectively.

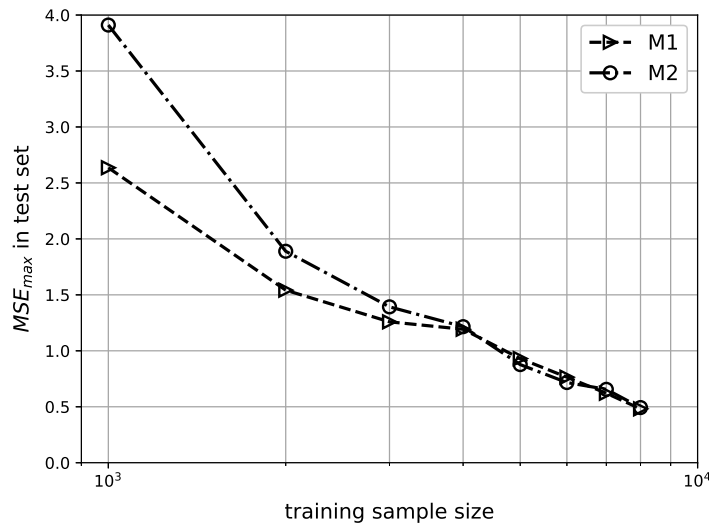


Figure 5.9: Sensitivity of the maximum approximation error ($RMSE_{max}$) in the test set to the training sample size for model M1 and M2.

5.4.2.2 Results of the SFT and flow loss estimates

In the MCMC simulation, the prior distributions of the estimated parameters are uniform and consistent with their prior distributions in the surrogate modeling step (Chapter 5.4.2.1). A total of $8e5$ samples are generated with the first $2e5$ samples being discarded in the MCMC simulation for both models. Gaussian-type proposal distribution functions are adopted and a final acceptance rate of 34% is achieved

for both MCMC simulations. It should be noted that, measurement errors in the temperature log are not considered in the inversion procedure.

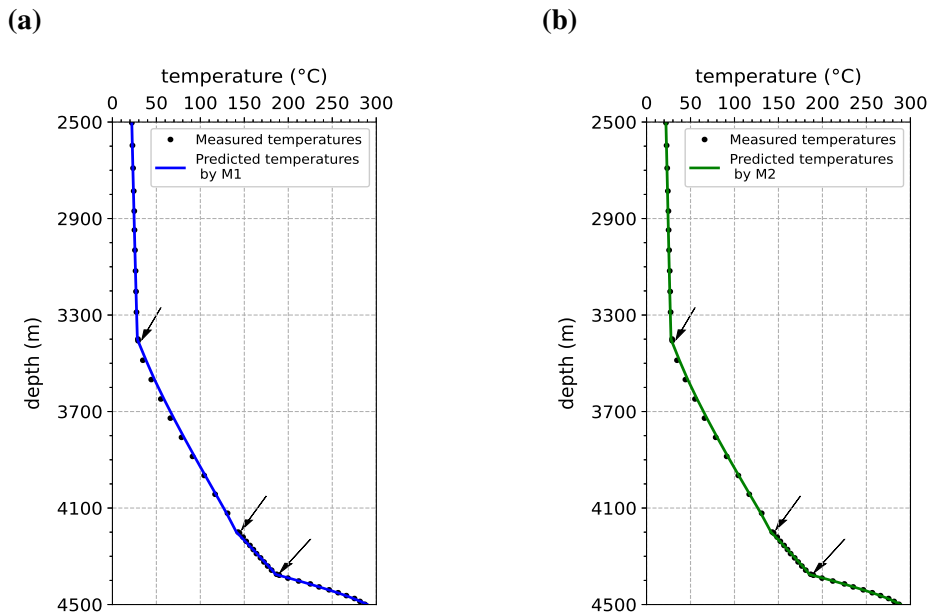


Figure 5.10: The best-fit temperature log predicted by the surrogate model M1 based on the single-layer assumption ((a), blue line) and the surrogate model M2 based on the five-layer assumption ((b), green line). The black dots and the arrows in (a) and (b) represent the measured temperatures and the location of three circulation loss zones, respectively.

The final PPDFs for the two models can be found in Appendix (Figure A.1 and Figure A.2). For the sake of an easier interpretation of the results, the inversion parameters (geothermal gradients and the relative flow losses) are converted to the corresponding SFT value at the base of each thermal layer and the accumulated loss (ALS) at each loss zone. In addition, the mean and the 95% confidence interval as well as the optimal estimate (maximum likelihood) for each parameter are summarized in Table 5.2. The temperature logs predicted by M1 and M2 using the optimal parameter values at depths between 2500 m and 4500 m are also shown in Figure 5.10 (blue line for M1 and green line for M2). The RMSE values for these two logs are 1.53 °C (M1) and 1.14 °C (M2) compared to the measured log (black dots); the RMSE values are 0.12 °C (M1) and 0.07 °C (M2) compared to their corresponding temperature logs simulated by the high-fidelity numerical model.

As shown in Table 5.2, the 95% confidence intervals of the estimates for the three accumulated losses in both models are quite narrow: the width of the confidence interval for each flow loss is less than 1%. Also, the difference in the upper and lower bound of the interval for each flow loss is within 0.4%. These indicate that the three flow losses can be well constrained by temperature measurement despite different

assumptions for the geothermal layers. After averaging the results of the two models, the optimal estimates for ALS1, ALS2, ALS3 are about 90.7%, 94%, and 98.6% respectively. On the other hand, the uncertainty in the SFT estimate for both models can be significant and vary at different depth (Figure 5.11). For example, the width of the 95% confidence interval of the SFT in the single-layer model increases linearly with depth. This could be due to an artificial effect caused by the strong assumption that the SFT profile is linear. However, in the five-layer model, the width of the 95% confidence interval become narrower after the second layer. This could be linked to the presence of the first loss zone (at 3400 m) that locates in the third layer. Since the flow rate decreases significantly after 3400 m (more than 90% has been lost into the formation), the impact of the high-rate injection on the borehole temperature becomes much less dominant. Meanwhile, the borehole temperature becomes more sensitive to the formation temperature and therefore can better constrain the SFT. According to the best-fit SFT profile, the convective zone with a near-zero geothermal gradient in the upper 2500 m is likely to extend within the first layer. From 2900 m to 4100 m (from the top of the second layer until to the bottom of the fourth layer), the thermal gradient becomes 0.13-0.19 °C/m. Below 4100 m, the gradient decreases almost to zero.

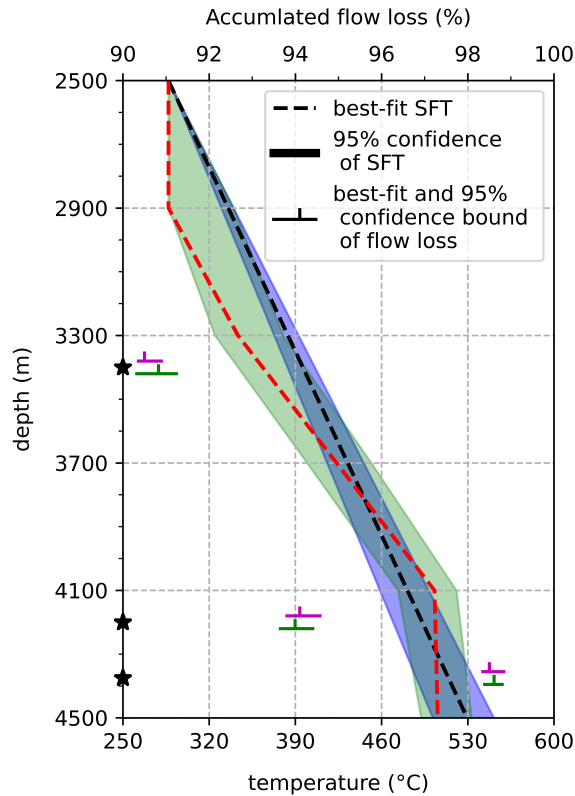


Figure 5.11: Prediction results of the two models: the optimal SFT profile (single-layer model: black dash line; five-layer model: red dash line); 95% confidence interval of SFT (single-layer model: blue shaded; five-layer model: green shaded); 95% confidence interval of the accumulated flow loss ratio (%) at 3400 m, 4200 m and 4375 m with the optimal estimate marked using a vertical tick (single-layer model: magenta horizontal line; five-layer model: green horizontal line). For better readability, the lines are shifted vertically away from the exact depths (marked with black stars) of the loss zones.

It should be mentioned that the assumptions about the distribution of the geothermal gradient underlying the single- and five-layer model are not verified because no such prior information is available for the investigated geothermal site. In fact, they are only adopted to test the effects of different prior information on the result of the SFT prediction. According to the present study, the maximum difference in the 95% confidence interval of the SFT estimate between the two models is about 70 °C and occurs at 3300 m (Figure 5.11); the SFT at 4500 m is most likely to be between around 492 °C and 551 °C. The temperature field around the RN-15/IDDP-2 has also been investigated by others using different approaches. Hokstad and Tanavasuu-Milkeviciene (2017) adopted Bayesian inversion using the multi-geophysical data collected during the drilling and their results suggest that the formation temperature at 4500 m is 535 °C (± 50 °C). Tulinius (2017) applied an analytical method (i.e., the so-called Horner-plot) to correct the disturbed temperature measurement for determining the SFT, their estimation for the in situ formation temperature at 4565 m is in the

range 536–549 °C. These results also appear to be comparable to those of the current study.

Models	Parameter	Mean (°C or %)	95% confidence interval (°C or %)	Optimal
single-layer	sft_bh	524.4	501.5 – 551.2	529.5
	ALS1	90.6	90.3 – 90.9	90.5
	ALS2	94.2	93.8 – 94.6	94.1
	ALS3	98.6	98.3 – 98.9	98.5
five-layer	sft1	304.1	287.0 – 340.0	289.6
	sft2	352.4	324.7 – 380.1	344.6
	sft3	425.3	399.5 – 451.7	423.8
	sft4	498.2	473.2 – 520.8	503.6
	sft5	511.7	492.1 – 533.1	504.9
	ALS1	90.8	90.3 – 91.3	90.8
	ALS2	94.0	93.6 – 94.4	94.0
	ALS3	98.6	98.4 – 98.9	98.6

sft_bh is the SFT at bottom-hole depth in the single-layer model, sft1-sft5 are the SFT estimates at the base of the five layers in the five-layer model. ALS1-ALS3 are the three accumulated flow losses (in %) at 3400 m, 4200 m, and 4375 m, respectively.

Table 5.2: Summary of the mean, 95% confidence range as well as the optimal estimation of each parameter in the single-layer and five-layer model.

5.5 Discussion and Conclusion

In the inversion scheme used in this study, the MCMC simulations are performed with surrogate models trained with an artificial neural network instead of numerical thermal models. In this way, the computation time for each MCMC simulation can be significantly reduced. For example, a forward calculation performed by the borehole simulator takes 105~188s on a local computer with four cores, while the surrogate models take only 0.08~0.1s. Compared to inversion modeling using numerical models, the surrogate-based approach is expected to improve the computation efficiency by 1300~1800 times. Moreover, the power of surrogate modeling can be much more significant in solving large-scale, highly nonlinear multiphysics problems, such as those often encountered in geoscience and reservoir engineering. This is mainly because the

efficiency of high-precision numerical models is still severely limited by memory and storage requirements (e.g., number of time steps and mesh refinement), the robustness of solution algorithms (e.g., convergence rate and discretization requirements), and complexity of the problem under study (dimensionality and nonlinearity). In contrast, surrogate models, once trained, can evaluate low-fidelity functions on the fly at any point of the model space. Therefore, they are more advantageous in terms of both speed and memory efficiency.

A cumbersome challenge with any surrogate modeling approach is the presence of surrogate approximation error (i.e., the difference between the high-fidelity and the surrogate model output), which can later introduce some intrinsic bias into the MCMC inversion step. In this study, the errors of the surrogate models are all below $0.5\text{ }^{\circ}\text{C}$ and less than the standard errors of temperature measurement instruments. Therefore, we neglect the intrinsic errors of the surrogate models in the MCMC modeling step. However, the achieved accuracy of a surrogate model may sometimes be limited, e.g., due to insufficient data available for training. In such cases, it can be necessary to take into account the approximation error of the surrogate model. Several methods have been proposed to address this problem. For example, Laloy et al. (2013) proposed a so-called two-stage MCMC simulation (i.e., in the first stage, the parameter space was sufficiently explored with the surrogate model, and in the second stage, the high-fidelity model was evaluated for correction). Another rather simple approach is to incorporate the surrogate approximation error (i.e., RMSE) directly into the error covariance matrix of the likelihood function in Eq.5.6 (Xu et al. 2017; Zhang, Zheng, Chen, Wu and Zeng 2020).

The proposed inversion method is applied to evaluate formation temperature in a thermal equilibrium condition (SFT) by inverting borehole temperature measurements obtained specifically under injection or cooling conditions, since these measurements are more readily available than under thermal recovery (shut-in) conditions. In synthetic test cases, results show that the method is very successful in predicting SFT profiles, provided that both the borehole temperature data and the surrogate model are accurate. If there is a flow loss zone in the borehole, the SFT estimation error at depths below the loss zone is likely to increase. In addition, noises in the measurement data can significantly affect the quality of the SFT estimates. In a test scenario where measurements have Gaussian noises, the maximum possible error of the predicted SFT at depth is between $16.6\text{ }^{\circ}\text{C}$ and $47.2\text{ }^{\circ}\text{C}$ in the 95% confidence interval. Therefore, high-quality temperature data should be used to obtain more reliable estimation results.

In a real-world example, the SFT is jointly estimated with three flow losses for depths

greater than 2500 m for the RN-15/IDDP-2 well in Reykjanes (Iceland). As mentioned in Friðleifsson et al. (2020), the Reykjanes geothermal system exhibits both conductive and convective heat transport behavior in the formation at depths shallower than 2500 m. Without knowing how the SFT profile develops below 2500 m, two different assumptions are made in this study. In one hypothesis, the geothermal gradient is constant. In the other hypothesis, the formation consists of multiple layers, and each layer may have different geothermal gradients. The inversion results indicate that the drilling losses can be well constrained from the temperature log: The predicted fluid losses are almost the same despite two different assumptions are used (the differences is than 0.3%). In addition, according to these results, almost complete fluid losses below 3400 m (> 90%) are encountered during the drilling of the RN-15/IDDP-2 well. In contrast, the SFT estimates are subjected to large uncertainties due to the lack of prior information about the distribution of the geothermal gradient. Nevertheless, the probable values for the SFT at 4500 m, ranging from 492 °C to 551 °C, are comparable with the results of two other relevant studies, one applying a correction method to down-hole temperature measurements and the other using an inversion approach based on multi-geophysical data.

5.6 Acknowledgments

The study is initiated during the DEEPEGS “Deployment of Deep Enhanced Geothermal Systems for Sustainable Energy Business” Project of the European Union’s Horizon 2020 research and innovation program. Accordingly, it received fund from this project (Grant Agreement No. 690771). The support from both the Helmholtz portfolio project “Geoenergy” and the program “Renewable Energies”, under the topic “Geothermal Energy Systems”, is also gratefully acknowledged. We also thank the EnBW Energie Baden-Württemberg AG for supporting geothermal research at KIT.

5.7 Author contributions statement

JW: developed the workflow of inversion procedure, performed numerical modeling, analyzed the results and wrote the manuscript; FN: supervised and supported the

design of the study, reviewed and edited the manuscript; EG: supervised and supported the design of the study, reviewed and edited the manuscript; TK: supervised the research and finalization of the manuscript. All authors read and approved the final manuscript.

Chapter 6

Conclusions and future work

Geothermal energy can provide an important contribution to the base-load energy supply because it is available everywhere and withdrawals are continuously replenished. Heat mining using EGS technology is considered the most important future use of geothermal resources due to the great energy potential of high-enthalpy deep boreholes. A special type of geothermal resource is geothermal fluids in supercritical conditions with temperatures higher than 374 °C. As supercritical fluids have a much higher power generation potential compared to subcritical fluids used in conventional geothermal power plants. However, the development of supercritical geothermal systems faces several challenges from different prospects, such as exploration methods, measurement, and logging technologies that can access the harsh downhole conditions. On the other hand, research efforts on effective approaches to interpreting the sparse and valuable data are urgently needed to compensate for the current difficulties in obtaining extensive geophysical data.

In this work, I focus on the numerical simulation and interpretation of temperature logs from high-enthalpy geothermal wells where cold water is continuously injected during drilling operations. The primary goal is to use measurements obtained from subcritical borehole conditions to assess the thermal equilibrium state of the formation, which could be supercritical before the drilling disturbance. The temperature of the undisturbed formation (SFT) is an important parameter for geothermal exploration that determines the energy potential of the reservoir, the installed capacity of geothermal plants and eventually the economics of a geothermal project. All the conventional methods to obtain SFT would require the thermal recovery data measured after drilling stops (Chapter 2). However, such a requirement can become a difficult endeavor for real practices in high-enthalpy boreholes due to commercial, safety, and regulatory aspects of the borehole operation as well as limitations from the temperature measurement device (e.g., maximum temperature range). As such, I investigate in this

dissertation a new concept of using injection temperature data to assess the SFT for high-enthalpy boreholes.

The incentive for the problems studied arises from the particular challenge of the high-enthalpy well, RN-15/IDDP-2, which is drilled under permanent cooling with multiple flow loss zones encountered at greater depths (Chapter 1). Numerical codes are first developed to simulate the complex drilling conditions to fulfill the prediction of the borehole temperature (Chapter 3). I then developed workflows to rigorously quantify uncertainty in SFT determination, subjected to the presence of flow loss zones, data noises, and insufficient prior information (Chapter 4), and finally solved the SFT in a statistical framework (Chapter 5), both by employing machine learning techniques. Three studies were carried out progressively to address several aspects, such as the key controlling factors for temperature distribution in a borehole during and after injection; the appropriate choice of data and methods for SFT determination for high-enthalpy wells; impact factors for the accurateness of the SFT estimates; the probabilistic distribution of the SFT and flow losses constrained on the measurement data. The main results of these studies (Chapter 3-5) are summarized in the following section.

6.1 Major findings of the research

The first study (Chapter 3) was conducted to first examine the key factors that control the thermal response of a high-enthalpy borehole drilled with circulation loss, both during injection and shut-in operations. For the shut-in period, free convective heat transfer can play a very important role in the temperature evolution during the early transient stage. Whereas for the injection phase, the temperature distribution in the well can be very sensitive to the flow loss, i.e., the flow loss leads to an increase in the local temperature gradient. The gradient rise has been shown to depend on several factors, such as the flow rate, the percentage of fluid loss as well as the lateral heat transfer between the formation and the fluid. When the fluid loss is relatively small (less than 30%) or when the injection rate is quite high, the fluid loss can be well characterized by a monotonic relationship with the temperature gradient increment. This highlights that the change in temperature gradient on a flowing temperature log can potentially be a very good indicator for quantifying flow losses.

The well-known Horner-plot method (HM) has been widely used to determine the SFT because of its simplicity. Herein, the accuracy of prediction with HM is investigated

for temperature data measured both during normal shut-in and during injection of very small flow rates at the wellhead, with flow lost to the formation in the deeper part of the well. The latter case is intended to mimic cooling in wells in a high-temperature environment, even during a thermal recovery period, to avoid damage to casing and logging instrumentation. Results indicate that SFT tends to be greatly underestimated during early shut-in times (less than 24 hours). The accuracy of the estimate depends on both the strength of the heat transfer and the measurement time of the temperature data. However, if temperatures measured after long shut-in times (at least more than two days) are used, the SFT can be determined accurately. When applying the HM to injection temperature logs, the estimation results can be inauspicious even if the temperatures are measured under low injection rates, which indicates the strong impact of any cooling source presented in the borehole.

It can therefore be demonstrated that the use of the HM type of temperature correction method to derive the SFT in high-enthalpy wells may encounter significant limitations. On the one hand, the long shut-in time required to make an accurate estimate can result in high temperatures in the borehole that exceed the operating limit of most measuring devices. In addition, a long pause during drilling to conduct these measurements will dramatically increase the drilling cost. On the other hand, the thermal recovery phase in high-enthalpy boreholes requires a lower injection rate into the wellbore to cool the casing and instruments. However, the cooling source, depending on its magnitude, can potentially lead to enormous errors in the estimates.

Based on the findings of the initial study, the focus of this research is directed to the inversion of temperature logs measured under injection conditions for SFT determination, as the application of HM has previously been challenging. The synthetic case studies in Chapter 4 provide insight into the effects of injection and drilling conditions, data quality, and aspects of inverse modeling, such as prior information, on the estimation accuracy of the SFT. Results therein suggest that, given data of the same quality, temperature log measured under relatively low flow rates or after shorter injection times should be preferred. Higher accuracy data need to be used, as this study shows that the error in the SFT prediction has an almost linear dependence on the standard error of the measured borehole temperatures. Downhole drilling can also play a role in a way that the difficulty of obtaining an accurate estimate of the SFT can increase dramatically if the drilling encounters an unknown circulation loss. Therefore, information about the amount of the loss, e.g., from flowmeter logs, or additional constraints on the range of the SFT, e.g., from geothermometers, would help improve prediction accuracy. Moreover, linear or piecewise linear shapes were assumed for the SFT, which means that the depths at which the thermal gradient starts

to change must be known before the inversion procedure. As the study showed, this would help to prevent bias in inversion results.

It is well recognized that geophysical data inversions very often face the problem of inherent non-uniqueness and, therefore, the difficulty to accept or reject the model or the values of the estimation parameters using deductive reasoning. Thus, in the second inversion study (Chapter 5), I intend to apply a more robust approach that can fully solve the SFT in a statistical framework by constructing the posterior probability density function using the Markov chain Monte Carlo (MCMC) algorithm. The inversion workflow was first tested with great success on synthetic temperature logs and then applied to temperature data from well RN-15/IDDP-2 to resolve SFT below 2500 m and unknown flow losses at three loss zones below 3400 m. Informed by the study in Chapter 4 that gradient change with depth is necessary prior information to avoid introducing bias into the inversion results, I introduced one model with a single geothermal layer and another with multiple geothermal layers. The two models were found to have very similar estimates for the three flow losses (differences less than 0.4%). Moreover, the losses seem to be well constrained by temperature measurements since the width of the 95% confidence interval for each loss is below 1%. The almost complete loss of circulation in the RN-15/IDDP-2 well is confirmed by this study, as the total loss rate in the three loss zones is most likely between 90.3% and 98.9%. In contrast, the maximum difference between the 95% confidence interval of the SFT estimate of the two models can be about 70 °C, which occurs above the first loss zone when the flow rate in the well is high. According to the present study, the undisturbed formation temperature at 4500 m is mostly likely to be between 492–551 °C. Such a result is still in agreement with other studies on this well which have focused on different types of data, e.g., geochemistry and geophysical logs (Chapter 1.2).

The research presented in this thesis is motivated by a key but challenging aspect of drilling for thermal deep geothermal exploration, namely the development of advanced data interpretation methods to overcome the current difficulties in obtaining sufficient data and the potentially large computational burden of the data interpretation process. To this end, I focused on the analysis of injection temperature logs which are technically easier to access and also more economical (e.g., waived from long measuring period compared to shu-in logs). I also adopted modern computational techniques such as data-driven approaches in the temperature data inversion procedure. Chapter 4 used surrogate models trained with a simple machine learning algorithm to suggest the most promising solution regions, resulting in high sampling efficiency. Another distinctive advantage of the applied approach is that it finds solutions to all

combinations of relevant model parameters that yield model predictions having the same fitting accuracy to the observation. By visualizing the results on a contour map, the uncertainties of the individual estimation parameters can be easily quantified. In Chapter 5, to reduce the computational cost of the MCMC approach, which requires a large number of forward evaluations, inverse modeling is performed using surrogate models created with artificial neural networks. These models run more than a thousand times faster than the original thermal modeling code. In this respect, this dissertation also represents a step forward towards more sophisticated techniques for predicting the undisturbed formation temperature, as most published work on this topic is still largely based on simple analytical methods (Chapter 2.3).

6.2 Future work

Borehole temperature is a complex response to various factors, in the most common cases, including the wellbore layout, the flow conditions, the heat transfer mechanism, measurement device, etc. Yet, in a wellbore during the drilling phase, the scenario can be much more complex and may require to account additionally for the history of injection, drilling schedule, the logging method (e.g. wire-line logging or distributed temperature sensing), and so on (Appendix B.1). The numerical study presented in this dissertation needs further improvements to model the borehole physics using realistic thermo-physical properties of the fluid as they will also affect the prediction of the borehole temperature (Abdollah Pour 2011; Nusiaputra 2017; Nitschke et al. 2020). Although this study assumes that cooling conditions prevail in the borehole, which makes the assumption of constant fluid properties acceptable to a certain extent, fluid properties can change dramatically, e.g. during the early injection or thermal recovery phase (e.g. when the flow rate is significantly reduced or injection is stopped), especially in the deeper part of the borehole when supercritical conditions exist in the reservoir. While the modeling of the equation of state for fluids in high temperature and high pressure regions still struggles with problems such as convergence difficulties of the solution around the critical point (Gernert et al. 2014), generally slow computational speeds (Brikowski 2001) and extrapolation errors in the phase diagram (Tirone 2015), some research studies, which can be referenced, have been carried out to simulate extreme reservoir conditions due to the global interest in developing deeper and hotter geothermal resources (Gunnarsson et al. 2011; Magnusdottir and Finsterle 2015).

In addition, there is an open question that I would have liked to investigate further, but due to time constraints, it will have to be left to future work. In the inversion study in Chapter 5, the formation has been divided into layers for SFT estimation. The division of these layers is only associated with the change of geothermal gradient with depth, hence called "geothermal layers". A question has remained for real-world applications such as the RN-15/IDDP-2 well: How many layers should be considered for the inversion problem? In a conductive geothermal system, the number of layers is usually determined according to the lithostratigraphic units. However, in convection dominated systems, the natural geothermal gradient is disturbed due to the movement of fluids in the formation and loses its connection to the geological units. In the case of RN-15/IDDP-2, high circulation loss in the lower part of the well seems to indicate that the formation has sufficient permeability for fluid movement, but this will not be known before a production test of the well. In fact, one important issue in solving inversion problems is the model selection problem which deals with the selection of the number of free parameters or unknowns. In terms of model parameterization, assuming too few parameters (e.g., layers) often lead to inadequate data fit and biased parameter estimates, while adopting too many parameters yield non-uniqueness solutions with excessive variance Hong and Sen (2009). To tackle such an issue, researchers have proposed to directly treat the number of unknowns itself as an unknown, which makes the inversion transdimensional (Sambridge et al. 2006; Guo et al. 2011). Typically, this approach uses a trade-off parameter that controls the balance between fit residuals and model smoothness (i.e., between model variance and resolution). The advantage of such an approach is that the uncertainty in the number of layers can be included in the model uncertainty estimates. However, since the number of layers must also be treated as an unknown when training the neural network to build surrogate models, this may add up to the overall computational cost.

Appendix A

Marginal PPDFs of the SFT and flow losses for the RN-15/IDDP-2 well

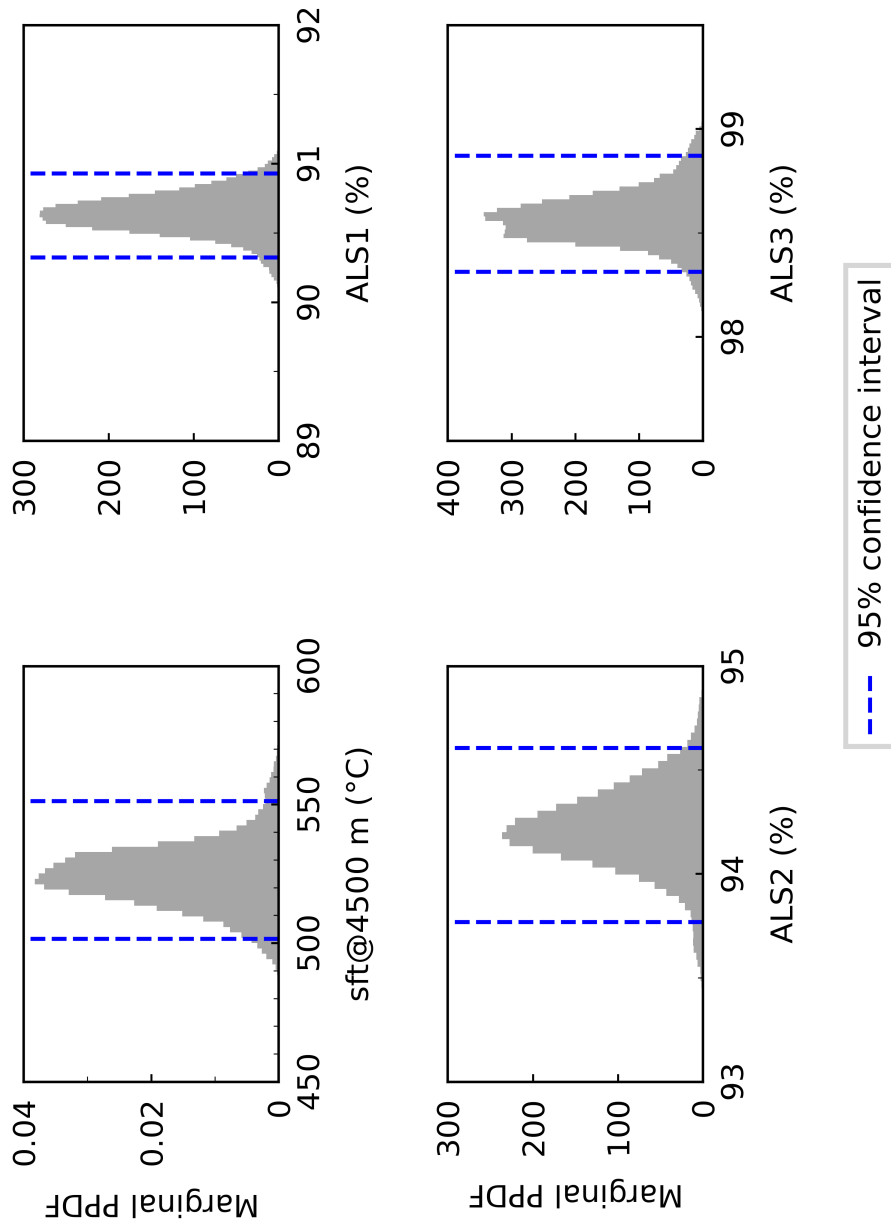


Figure A.1: Marginal PPDFs of the estimation parameters (SFT at the 4500 m and the three accumulated flow losses, ALS1-ALS3) for the single-layer model. The blue dash lines mark the 95% confidence interval of each parameter.

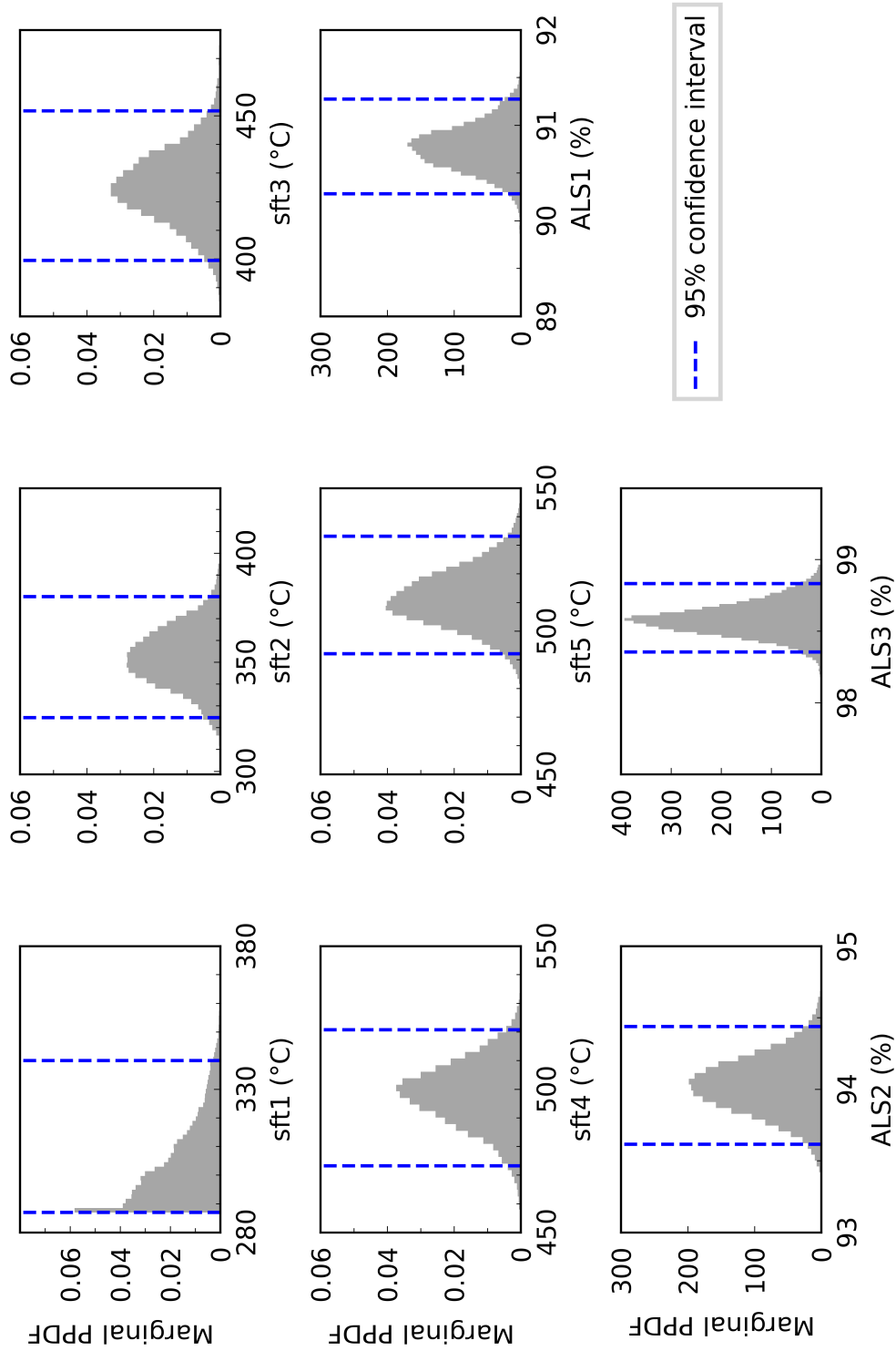


Figure A.2: Marginal PPDFs of SFT at the base of each layer (sft1-sft5) and the three accumulated flow losses (ALS1-ALS3) for the five-layer model.

Appendix B

Simulation of temperature log for the RN-15/IDDP-2 well

B.1 Introduction

In the framework of the DEEPEGS (Deployment of Deep Enhanced Geothermal Systems for Sustainable Energy Business) Horizon 2020 research project, Reykjanes was selected as one of the test sites for demonstrating the feasibility of delivering energy using renewable resources. Prior to this project, the Icelandic geothermal field has already been exploited by a long-term project for high-temperature hydrothermal systems –the Iceland Deep Drilling Project (IDDP). The target of the IDDP is to drill into supercritical zones with temperatures ranging from 450 to 600 °C where the power production of a single well is expected to increase tenfold compared to a conventional sub-critical geothermal well (Fridleifsson and Elders 2005). Consequently, this requires the drilling of significantly deeper boreholes (> 4 km) than conventional ones.

The Reykjanes geothermal field is located at the tip of the volcanic peninsula in the southwest of Iceland. It is on the extension of the Mid-Atlantic Ridge, which lies on the diverging plate boundary of the American and the Eurasian plates. Since the late '90 s, over thirty wells down to less than three-kilometer deep have been drilled in Reykjanes. Collected data from drill cores, flow testing, chemical measurements as well as temperature and pressure logging from these wells have provided constraints on the geological and geo-physical conditions at the field. Based on the gained knowledge, the IDDP2 well was drilled by deepening an existing vertical production well – RN15 that situates near a main hydrothermal up-welling zone where the permeability at deeper depth is controlled by fracture system (Friðleifsson et al. 2020). The maximum temperature that was measured was 426 °C at the well bottom with fluid pressure reaching 340 bars, which reveals the successful drilling into supercritical conditions.

The simulation of a single temperature log for the RN15-IDDP2 well can be complex due to the highly dynamic drilling conditions that involve the variation of flow rate during long-term injection, the deepening of the well, the presence of circulation loss, the temporal change of measurement depth of temperature during the tripping of the logging tool, etc. As a supplementary material to Chapter 5, the presented simulations herein consist of the preliminary investigations on the key aspects that need to take into account to achieve success in the temperature prediction for the RN15-IDDP2 well using numerical models.

B.2 Drilling and temperature logging data of the RN-15/IDDP-2 well

The details of drilling the RN-15/IDDP-2 well have been described in numerous contributions (Friðleifsson et al. 2014; Friðleifsson and Elders 2017; Friðleifsson et al. 2017). Drilling was started with the old RN-15 well at 2.5 km depth and took 168 days before the well reached a final measured depth of 4659 m on January 25th, 2017. During the drilling, several loss zones were encountered, with a major one located below the production casing shoe at around 3.2 km depth. Only rocks samples from deeper than 3100 m were available and were recovered with a limited total amount of less than 30 m. As a result, detailed information on the physical properties of rocks is still missing. However, previous studies (Friðleifsson et al. 2014) showed that the subsurface lithology of the Reykjanes geothermal field until 2.5 km is a characteristic of basaltic formations at depth beneath 1.4~1.5 km. From there up to ca. 400 m is a phreatic environment with tuffs and marine sediments. Then at the shallower part, the stratigraphic unit mainly consists of subglacial/submarine hyaloclastite formations which are often highly porous and permeable. In this study, constant physical properties of basaltic rock type are assumed, except that the thermal conductivity was calibrated along the depth using available temperature measurements and static formation temperature data around the well that are already presented in Chapter 5 (Figure 5.7).

B.3 Sensitivity analysis of the key factors

B.3.1 Impact of the flow averaging scheme

Injection flow at the wellhead was measured at a five-second interval, which is too small a time step size for modeling the selected temperature log, which must account for an injection period of 145 days. Therefore, the flow rate data needs to be averaged properly to reduce both the computational effort and the impact of averaging on the system behavior. As such, an analysis of the sensitivity of the borehole temperature to the applied flow-time function was performed and comprised three different cases:

- *FL1*, the mean flow rate over 145 days' period.
- *FL2*, daily average flow rates.
- *FL3*, daily average flow rates, except for the four weeks before the logging: every-ten-minutes averaged flow rates.

Since the SFT below 2.5 km as well as the amount of flow loss at each loss zone is not known yet, the sensitivity analysis was performed based on synthetic data. It was assumed that the accumulated flow loss at 3400 m and 4200 m were 90% and 95% respectively, and the SFT below 2500 m increased linearly to 500 °C at 4500 m. These data were designed to reflect the large drilling circulation loss and the high-temperature environment of the RN-15/IDDP-2 well, as mentioned in the drilling report. Temperature logs were simulated using the three different flow averaging schemes and their comparison is shown in Figure B.2. Note that the temperature log simulated with FL3 was considered as a reference log, due to its small-time-interval (ten minutes) data input over a long period (four weeks) before the log was calculated (i.e., reasonably accurate input data). It can be seen that FL2 is a good proxy of FL3 since the maximum difference in the temperature logs was only 0.07 °C. However, the maximum difference is about 25 °C in the temperature logs simulated with FL1 and FL3, which means that FL1 is not a reasonable scheme for flow averaging. It is also noticeable that for both comparisons, the impact of choosing different flow-time functions on the borehole temperature is much stronger at depths below the flow loss zones than at depths above the loss zones. This could be due to the fact that temperature is more sensitive to the flow variation in lower flow rate regime.

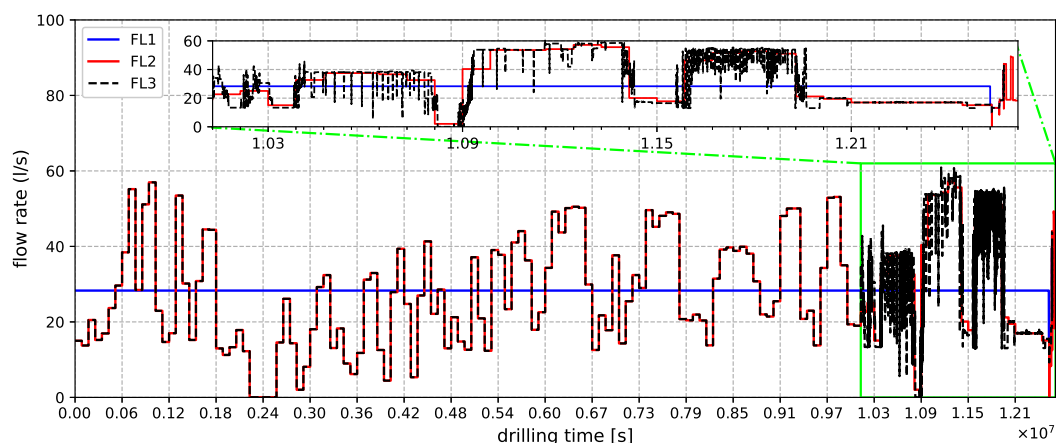


Figure B.1: Three different flow-time functions applied at the wellhead over 145 days. FL1: The average flow over a period of 145 days. FL2: Daily average flow rates. FL3: Daily average flow rates, except that flow rate is averaged every ten minutes for the four weeks prior to logging.

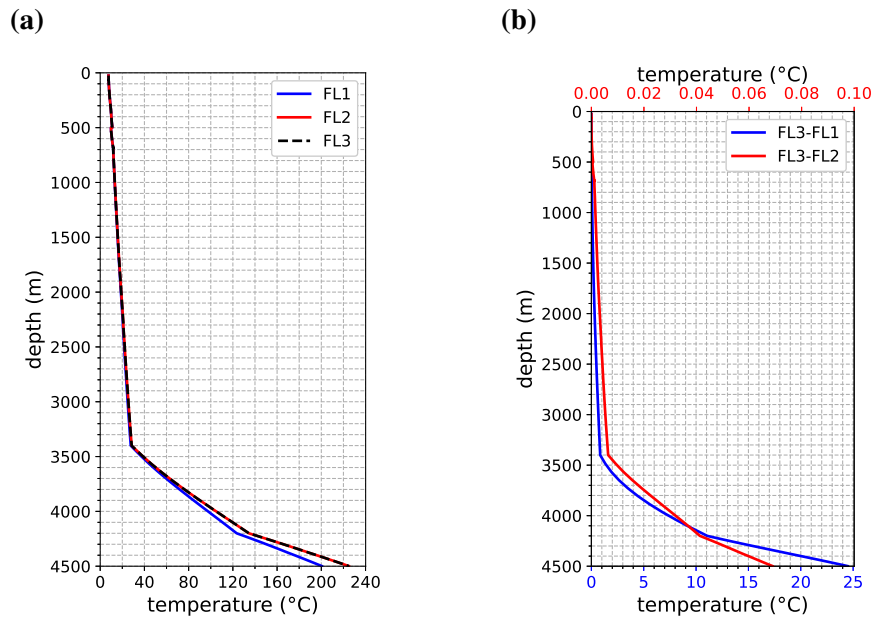


Figure B.2: (a) Temperature logs simulated with the three different flow average scheme FL1–FL3. (b) Temperature difference along depth between the logs simulated with FL1 and FL3 (blue), and the logs simulated with FL2 and FL3 (red).

B.3.2 Impact of the deepening of the well

The change in the well length could play an important role in predicting the borehole temperatures under drilling conditions. The cooling times of the drilling mud at different well sections are not the same in reality. Therefore, it is necessary to consider the drilling schedule (Figure B.3a) (i.e., the change in the well length with time) in the numerical modeling to avoid over- or under-prediction of borehole temperature at the local depth. In this study, this was accomplished by considering the flow rate along the well as a function of time and well depth, i.e., the flow rate at any depth is zero before the drill rig reaches that depth and becomes the injection rate at the wellhead or the remaining flow after flow is lost into the formation at the loss zones. Figure B.3b shows, as an example, the change in borehole temperature with time at different depths (3400 m, 4200 m and 4375 m) with varying flow. For each depth, the temperature perturbation caused by drilling starts at a different time, with the shallower depth starting earlier. This temperature log was compared with the log simulated assuming a pre-existing full-length borehole prior to fluid injection. According to Figure B.4, neglecting the borehole development process leads to an underestimation of the borehole temperature at depths below the first loss zone, but

has no obvious effect on the temperature prediction above the first loss zone. The error in the prediction increases with depth and is about $17\text{ }^{\circ}\text{C}$ at the bottom of the borehole. The reason for this is that with increasing depth, the time of local fluid circulation is overestimated, and consequently, the temperature at this depth is underestimated. However, the impact of deepening the well is expected to diminish if the temperature is predicted long enough after the depth of the well is fully developed. In addition, the higher the injection rate, the faster such impact would disappear.

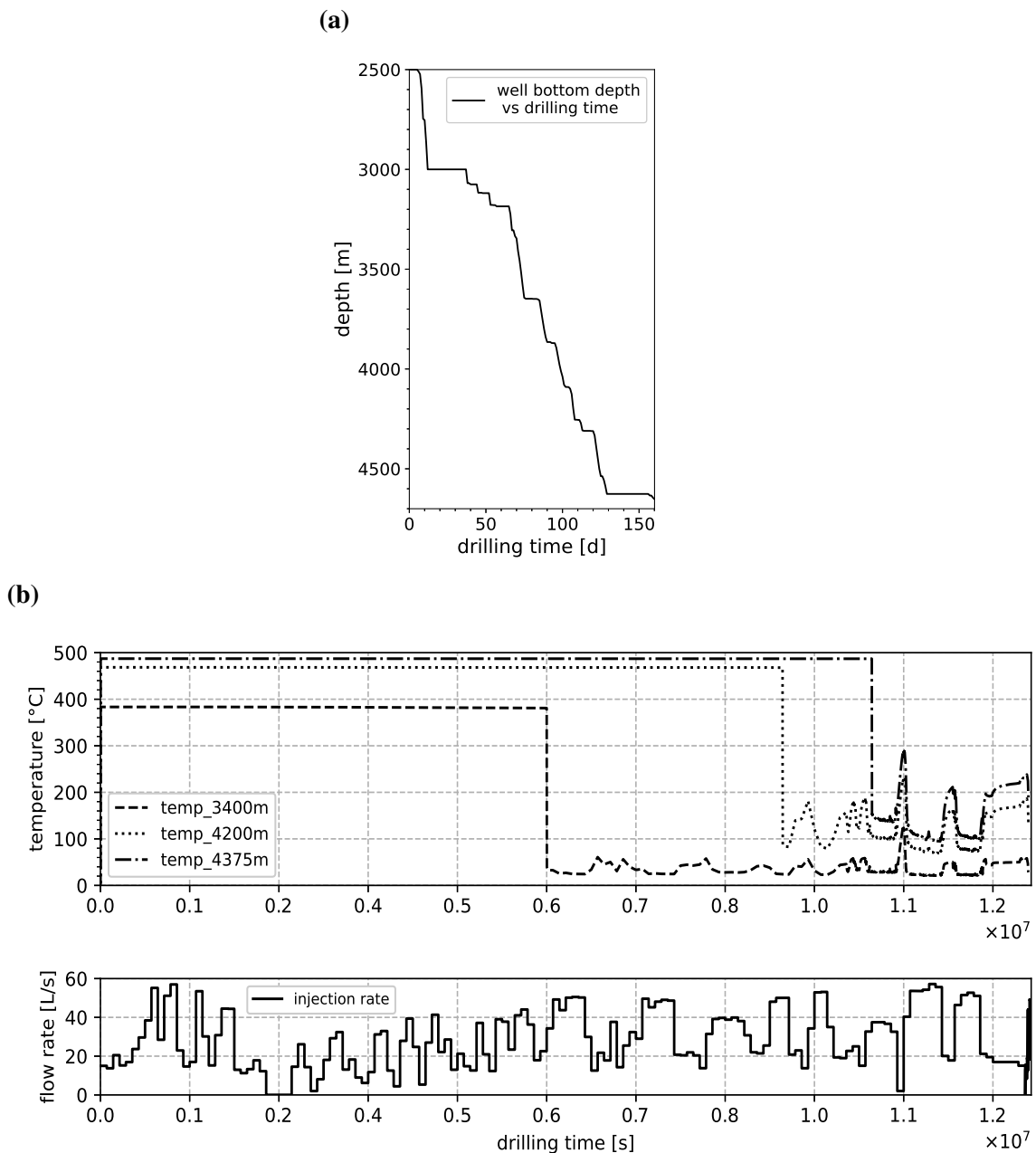


Figure B.3: (a) Drilling schedule. (b) Upper panel: Change in well temperature at 3400 m, 4200 m and 4375 m as a function of drilling time. Lower panel: Variation of injection flow rate at the wellhead with time.

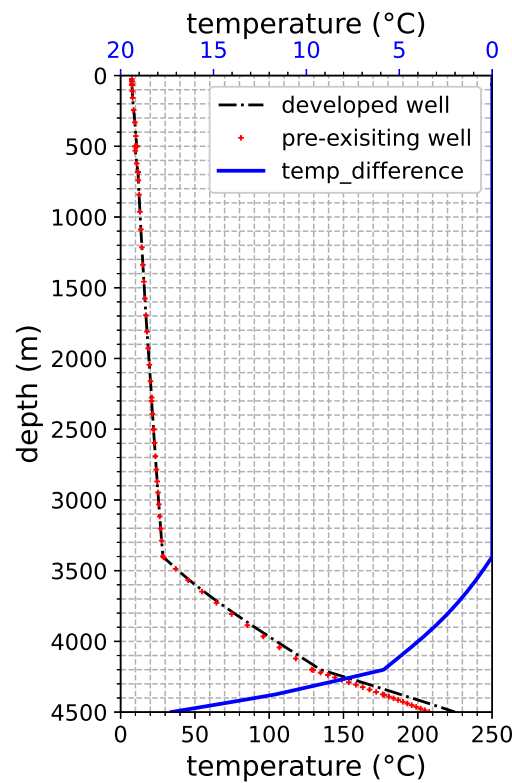


Figure B.4: Simulated temperature logs when assuming a pre-existed well before the injection (red cross) and when considering the drilling schedule (black dashed line), and the difference between the two logs (blue solid line).

B.3.3 Impact of the movement of the logging tool

In conventional downhole logging, such as wireline logging, temperature sensor (probes) are moved in or out along the borehole and record the temperature at each specified depth. Therefore, the temperature is measured at a different time for each depth. Considering the tripping time of a logging tool can be hours, the borehole temperature can change very quickly, especially if the injection flow rate fluctuates in the meantime. Therefore, it would be unrealistic or incorrect to consider a 'snapshot' for the temperature profile at any point in time as the actual logging profile. In this example, the variation of the injection rate and the movement speed of the logging tool (Figure B.5) are integrated into the modeling. The simulated temperature log and the instantaneous temperature profiles at the beginning and end of the logging are plotted in Figure B.6. It can be seen that temperatures below 500 m have dramatically changed since logging began, but the temperature appears to be stabilizing very quickly, as indicated by the slight difference between the actual log and the instantaneous

temperature profile at the end of the logging. This is likely due to the increase in flow rate when the logging tool reached 500 m (Figure B.5) so that the borehole temperature can quickly reach "steady-state" at a high flow rate.

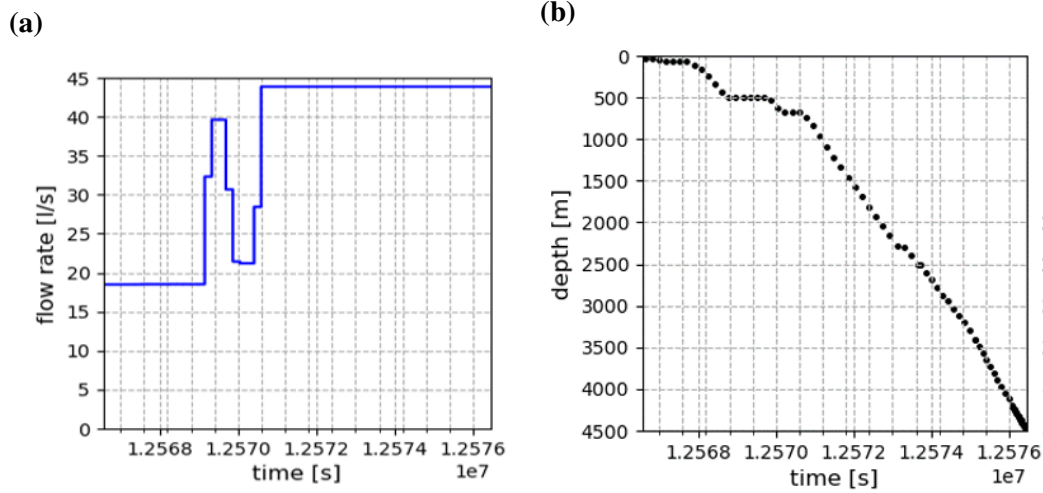


Figure B.5: (a) Flow rate variation with time during logging. (b) Change in the depth location of the logging tool with time.

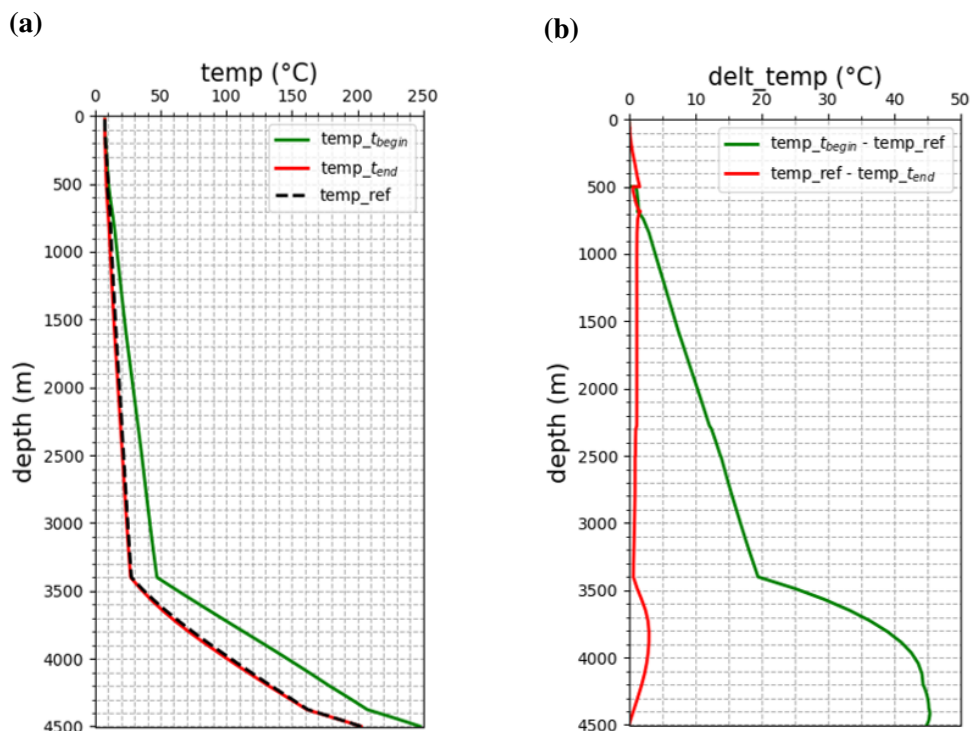


Figure B.6: (a) Snapshots of the temperature profile along the borehole at the beginning ($temp_{t_{begin}}$) and end of logging as well as the measured profile ($temp_{t_{end}}$). (b) Difference between the log and the temperature profile of the borehole at the beginning of the logging (green line) and between the profile of the log and the temperature profile of the borehole at the end of the logging (red line).

B.4 Calibration of the effective thermal conductivity of the formation

As mentioned earlier, the upper 2.5 km of the Reykjanes geothermal field is a hydrothermal system in which thermal conduction and advection occur at different depths. Therefore, a so-called effective thermal conductivity (Witte 2001) should be used in the numerical model, which, in addition to pure heat conduction, also takes into account the advective heat transport mechanism. The value of the formation thermal conductivity was calibrated using the borehole temperature measurements in the upper 2.5 km and the prior known SFT profile (Figure 5.7a). Using the thermal properties of materials of the casing, cement, formation and drilling mud listed in Table B.1, the following distribution of effective thermal conductivity of the formation was determined by trial and error: the thermal conductivity is 10.0 W/K/m from surface to 300 m, 4.0 W/K/m between 300 m and 800 m, and 2.0 W/K/m below 800 m. The result of the data fitting is given in Figure B.7. The layering of the formation evident from these thermal conductivity values agree relatively well with the description from Friðleifsson et al. (2014) about the stratigraphy of the Reykjanes field (section B.2). The high effective thermal conductivity in the upper layers could be due to the enhancement of heat transport by groundwater flow in the near-surface aquifers and precipitation infiltration through highly permeable rocks. Furthermore, the thermal conductivity of 2.0 W/K/m at depth below 800 m appears to be a reasonable estimate for typical Icelandic basaltic rocks (Ruether 2011). Due to a lack of data, this study uses the same value for thermal conductivity (2.0 W/K/m) for the formation below 2.5 km.

Material	ρ (kg/m^3)	c_p ($J/kg/K$)	λ ($W/K/m$)
Steel	8000	500	50
Cement	1830	1900	0.99
Formation	2650	900	(?)
Drilling fluid	4194	998	0.6

Table B.1: Material properties of the casing, cementing program and the formation

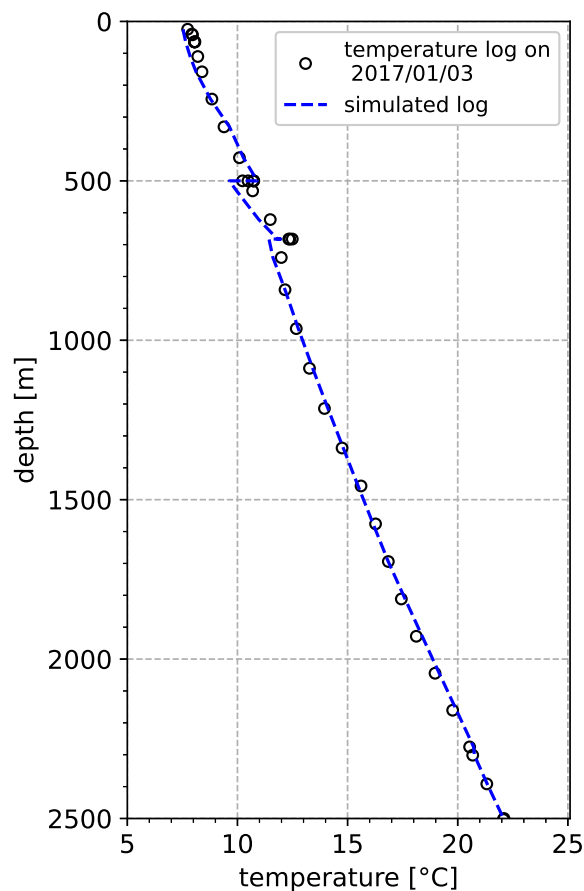


Figure B.7: The measured temperature log (black circles) and calibrated temperature logs for the upper 2500 m (blue dash line).

B.5 Summary

This case study presents the simulation of a single temperature log obtained from the drilling of the well, RN-15/IDDP-2. The simulation takes into account several factors such as long-term flow variations, well depth evolution, and temporal and spatial variation in temperature sampling due to the movement of the logging device. It can be shown that for long-term transient flow injections, a proper flow averaging scheme is required to compensate between the high-resolution data input and the accuracy of the model prediction. If the well is under development, the prediction of the borehole temperature can theoretically be much more complex since the specific cooling time at each depth investigated must be taken into account. Assuming a pre-existing well in the modeling may underestimate the temperature because cooling at the later drilled depth tends to be overestimated. According to the current study, the impact of well

deepening can be reduced if the predictions are made for a relatively long time after the well has reached its full depth. Furthermore, the injection flow rate can also play a role. When the well is under strong cooling at a high injection rate, the influence of the well deepening decreases more quickly. Finally, the numerical model needs to take the method of logging into consideration. For conventional logging methods like wire-line, the difference in the temperature measurement time at different depths can be several hours. Due to temperature evolution over such a long period of time, the logging profile can be different from an instantaneous temperature profile in the well, especially if the flow rate highly fluctuates or the flow rate is so low that it takes a long time for the temperature to reach a steady state. The above factors are found to have a greater effect on the temperature prediction for the depths below the loss zone than for the depths above the loss zone.

Bibliography

- Aabø, T.M., & Hermanrud, C. (2019), 'Toward a global model for correction of bottomhole temperature data: Progress and limitations', *AAPG Bulletin* 103, 139–155.
- Abdollah Pour, R. (2011), Development and application of a 3D equation-of-state compositional fluid-flow simulator in cylindrical coordinates for near-wellbore phenomena, PhD thesis, The University of Texas at Austin.
- Agemar, T., Schellschmidt, R., & Schulz, R. (2012), 'Subsurface temperature distribution in Germany', *Geothermics* 44, 65–77.
- Al Saedi, A., Flori, R.E., & Kabir, C. (2019), 'Estimating the initial-formation temperature and flowing-temperature gradient with transient-temperature analysis: applications in gas reservoirs', *Journal of Natural Gas Science and Engineering* 66, 126–137.
- Albert, J. (2009), *Bayesian computation with R*, Springer Science & Business Media.
- Alfonsi, A., Rabiti, C., Mandelli, D., Cogliati, J.J., Wang, C., Maljovec, D.P., Talbot, P.W., & Smith, C.L. (2016), Raven theory manual, Technical report, Idaho National Lab.(INL), Idaho Falls, ID (United States).
- Allahvirdizadeh, P. (2020), 'A review on geothermal wells: Well integrity issues', *Journal of Cleaner Production* p. 124009.
- Andaverde, J., Verma, S.P., & Santoyo, E. (2005), 'Uncertainty estimates of static formation temperatures in boreholes and evaluation of regression models', *Geophysical Journal International* 160, 1112–1122.
- Andersen, C., & Weis, P. (2020), 'Heat transfer from convecting magma reservoirs to hydrothermal fluid flow systems constrained by coupled numerical modeling', *Geophysical Research Letters* 47, e2020GL089463.
- Arnórsson, S. (1995), 'Geothermal systems in Iceland: structure and conceptual models—I. High-temperature areas', *Geothermics* 24, 561–602.

- Asanuma, H., Muraoka, H., Tsuchiya, N., & Ito, H. (2012), 'The concept of the Japan Beyond-Brittle Project (JBBP) to develop EGS reservoirs in ductile zones', *GRC Transactions* 36, 359–364.
- Ascencio, F., García, A., Rivera, J., & Arellano, V. (1994), 'Estimation of undisturbed formation temperatures under spherical-radial heat flow conditions', *Geothermics* 23, 317–326.
- Ascencio, F., Rivera, J., & Samaniego, F. (1997), On the practical aspects of determination of the true reservoir temperature under spherical heat flow conditions, in 'Proc. 21st Workshop on Geothermal Reservoir Engineering, Stanford University, Stanford, Cal., January', pp. 27–29.
- Ascencio, F., Samaniego, F., & Rivera, J. (2006), 'Application of a spherical-radial heat transfer model to calculate geothermal gradients from measurements in deep boreholes', *Geothermics* 35, 70–78.
- Ásmundsson, R., Pezard, P., Sanjuan, B., Hennings, J., Deltombe, J.L., Halladay, N., Lebert, F., Gadalia, A., Millot, R., Gibert, B. et al. (2014), 'High temperature instruments and methods developed for supercritical geothermal reservoir characterisation and exploitation—The HiTI project', *Geothermics* 49, 90–98.
- Atangana, A. (2017), *Fractional operators with constant and variable order with application to geo-hydrology*, Academic Press.
- Athens, N.D., & Caers, J.K. (2019), 'A Monte Carlo-based framework for assessing the value of information and development risk in geothermal exploration', *Applied Energy* 256, 113932.
- Bahlburg, H., & Breitzkreuz, C. (2018), *Grundlagen der Geologie*, Springer-Verlag.
- Bahonar, M., Azaiez, J., & Chen, Z. (2011), 'Two issues in wellbore heat flow modelling along with the prediction of casing temperature in the steam injection wells', *Journal of Canadian Petroleum Technology* 50, 43–63.
- Baird, T., Fields, T., Drummond, R., Mathison, D., & Langseth, B. (1998), 'High-pressure, high-temperature well logging, perforating and testing', *Oilfield review* 10, 50–67.
- Barton, C.A., Zoback, M.D., & Moos, D. (1995), 'Fluid flow along potentially active faults in crystalline rock', *Geology* 23, 683–686.

- Bassam, A., Santoyo, E., Andaverde, J., Hernández, J., & Espinoza-Ojeda, O. (2010), 'Estimation of static formation temperatures in geothermal wells by using an artificial neural network approach', *Computers & Geosciences* 36, 1191–1199.
- Bear, J. (2018), *Modeling phenomena of flow and transport in porous media*, Vol. 1, Springer.
- Bedard, M. (2008), 'Optimal acceptance rates for Metropolis algorithms: Moving beyond 0.234', *Stochastic Processes and their Applications* 118, 2198–2222.
- Bense, V., Read, T., Bour, O., Le Borgne, T., Coleman, T., Krause, S., Chalari, A., Mondanos, M., Ciocca, F., & Selker, J. (2016), 'Distributed Temperature Sensing as a downhole tool in hydrogeology', *Water Resources Research* 52, 9259–9273.
- Bertani, R., Büsing, H., Buske, S., Dini, A., Hjelstuen, M., Luchini, M., Manzella, A., Nybo, R., Rabbel, W., Serniotti, L. et al. (2018), The first results of the Descramble project, in '43rd Workshop on Geothermal Reservoir Engineering', pp. 1–16.
- Berthold, S. (2010), 'Synthetic convection log—characterization of vertical transport processes in fluid-filled boreholes', *Journal of Applied Geophysics* 72, 20–27.
- Berthold, S., & Börner, F. (2008), 'Detection of free vertical convection and double-diffusion in groundwater monitoring wells with geophysical borehole measurements', *Environmental geology* 54, 1547–1566.
- Bignall, G. (2010), 'Hotter and deeper: New Zealand's research programme to harness its deep geothermal resources', *Proc. World. Geoth. Cong.*
- Bobok, Z.S.E., & Szarka, Z. (2012), 'Determination of the temperature distribution in the circulating drilling fluid', *Geosci Eng* 1, 37–47.
- Bowden, G.J., Dandy, G.C., & Maier, H.R. (2005), 'Input determination for neural network models in water resources applications. Part 1—background and methodology', *Journal of Hydrology* 301, 75–92.
- Breede, K., Dzebisashvili, K., & Falcone, G. (2015), 'Overcoming challenges in the classification of deep geothermal potential', *Geothermal Energy Science* 3, 19–39.
- Brikowski, T.H. (2001), Modeling supercritical systems with TOUGH2: preliminary results using the EOS1SC equation of state module, in 'Proceedings, 26-th Workshop on Geothermal Reservoir Engineering', pp. 208–215.
- Bu, X., Ma, W., & Li, H. (2012), 'Geothermal energy production utilizing abandoned oil and gas wells', *Renewable energy* 41, 80–85.

- Bullard, E. (1947), 'The time necessary for a bore hole to attain temperature equilibrium', *Geophysical Journal International* 5, 127–130.
- Buntebarth, G. (2012), *Geothermics: an introduction*, Springer Science & Business Media.
- Cacace, M., Kaiser, B.O., Lewerenz, B., & Scheck-Wenderoth, M. (2010), 'Geothermal energy in sedimentary basins: What we can learn from regional numerical models', *Geochemistry* 70, 33–46.
- Cao, S., Lerche, I., & Hermanrud, C. (1988), 'Formation temperature estimation by inversion of borehole measurements', *Geophysics* 53, 979–988.
- Cathles, L. (1977), 'An analysis of the cooling of intrusives by ground-water convection which includes boiling', *Economic Geology* 72, 804–826.
- Cermak, V., Bodri, L., Rybach, L., & Buntebarth, G. (1990), 'Relationship between seismic velocity and heat production: comparison of two sets of data and test of validity', *Earth and Planetary Science Letters* 99, 48–57.
- Chamorro, C.R., Mondéjar, M.E., Ramos, R., Segovia, J.J., Martín, M.C., & Villamañán, M.A. (2012), 'World geothermal power production status: Energy, environmental and economic study of high enthalpy technologies', *Energy* 42, 10–18.
- Chen, M., Izady, A., & Abdalla, O.A. (2017), 'An efficient surrogate-based simulation-optimization method for calibrating a regional MODFLOW model', *Journal of hydrology* 544, 591–603.
- Clauser, C. (2006), 'Geothermal energy Landolt-Börnstein, Group VIII: Advanced Materials and Technologies, Vol. 3: Energy Technologies, Subvol. C: Renewable Energies ed K Heinloth'.
- Clow, G.D. (2008), *USGS polar temperature logging system, description and measurement uncertainties*, US Department of the Interior, US Geological Survey.
- Clow, G.D. (2015), 'A Green's function approach for assessing the thermal disturbance caused by drilling deep boreholes in rock or ice', *Geophysical Journal International* 203, 1877–1895.
- Coleman, T.I., Parker, B.L., Maldaner, C.H., & Mondanos, M.J. (2015), 'Groundwater flow characterization in a fractured bedrock aquifer using active DTS tests in sealed boreholes', *Journal of Hydrology* 528, 449–462.

- Colgan, W., MacGregor, J.A., Mankoff, K.D., Haagensohn, R., Rajaram, H., Martos, Y.M., Morlighem, M., Fahnestock, M.A., & Kjeldsen, K.K. (2021), 'Topographic correction of geothermal heat flux in Greenland and Antarctica', *Journal of Geophysical Research: Earth Surface* 126, e2020JF005598.
- Cooper, J., & Dooley, R. (2007), 'Revised release on the IAPWS industrial formulation 1997 for the thermodynamic properties of water and steam', *The International Association for the Properties of Water and Steam* 1, 48.
- Danielsen, P.E. (2008), High temperature geothermal logging for temperature and pressure, in 'Conference, ARGeo C-2, Entebbe, Uganda'.
- Deming, D. (1989), 'Application of bottom-hole temperature corrections in geothermal studies', *Geothermics* 18, 775–786.
- Diersch, H.J., Bauer, D., Heidemann, W., Rühaak, W., & Schätzl, P. (2011), 'Finite element modeling of borehole heat exchanger systems: Part 1. Fundamentals', *Computers & Geosciences* 37, 1122–1135.
- Diment, W.H. (1967), 'Thermal regime of a large diameter borehole: instability of the water column and comparison of air-and water-filled conditions', *Geophysics* 32, 720–726.
- Diment, W.H., & Urban, T.C. (1983), SIMPLE METHOD FOR DETECTING ANOMALOUS FLUID MOTIONS IN BOREHOLES FROM CONTINUOUS TEMPERATURE LOGS., in 'Geothermal Resources: Energy on Tap! Geothermal Resources Council 1983 Annual Meeting.', Vol. 7, pp. 485–490.
- Dittus, F., & Boelter, L. (1985), 'Heat transfer in automobile radiators of the tubular type', *International communications in heat and mass transfer* 12, 3–22.
- Dowdle, W., Cobb, W. et al. (1975), 'Static formation temperature from well logs-an empirical method', *Journal of Petroleum Technology* 27, 1–326.
- Drakeley, B.K., Johansen, E.S., Zisk, E., Bostick III, T. et al. (2006), In-well Optical Sensing-State Of The Art Applications And Future Direction For Increasing Value in Production Optimization Systems, in 'Intelligent Energy Conference and Exhibition', Society of Petroleum Engineers.
- Driesner, T., & Heinrich, C.A. (2007), 'The system H₂O–NaCl. Part I: Correlation formulae for phase relations in temperature–pressure–composition space from 0 to 1000 C, 0 to 5000 bar, and 0 to 1 XNaCl', *Geochimica et Cosmochimica Acta* 71, 4880–4901.

- Drury, M. (1984), 'On a possible source of error in extracting equilibrium formation temperatures from borehole BHT data', *Geothermics* 13, 175–180.
- Espinosa-Paredes, G., & Garcia-Gutierrez, A. (2003), 'Estimation of static formation temperatures in geothermal wells', *Energy conversion and management* 44, 1343–1355.
- Espinosa-Paredes, G., Garcia, A., Santoyo, E., & Hernandez, I. (2001), 'TEMLOPI/V. 2: a computer program for estimation of fully transient temperatures in geothermal wells during circulation and shut-in', *Computers & geosciences* 27, 327–344.
- Espinosa-Paredes, G., Morales-Díaz, A., Olea-González, U., & Ambriz-Garcia, J. (2009), 'Application of a proportional-integral control for the estimation of static formation temperatures in oil wells', *Marine and Petroleum Geology* 26, 259–268.
- Espinoza-Ojeda, O., & Santoyo, E. (2016), 'A new empirical method based on log-transformation regressions for the estimation of static formation temperatures of geothermal, petroleum and permafrost boreholes', *Journal of Geophysics and Engineering* 13, 559–596.
- Espinoza-Ojeda, O., Santoyo, E., & Andaverde, J. (2011), 'A new look at the statistical assessment of approximate and rigorous methods for the estimation of stabilized formation temperatures in geothermal and petroleum wells', *Journal of Geophysics and Engineering* 8, 233–258.
- Fenta, M.C., Potter, D.K., & Szanyi, J. (2021), 'Fibre optic methods of prospecting: A comprehensive and modern branch of geophysics', *Surveys in Geophysics* 42, 551–584.
- Fernández, M., Eguía, P., Granada, E., & Febrero, L. (2017), 'Sensitivity analysis of a vertical geothermal heat exchanger dynamic simulation: Calibration and error determination', *Geothermics* 70, 249–259.
- Flóvenz, Ó.G., & Saemundsson, K. (1993), 'Heat flow and geothermal processes in Iceland', *Tectonophysics* 225, 123–138.
- Fontanilla, J.P. (1980), A Mathematical model for the prediction of wellbore heat loss and pressure drop in steam injection wells, Master's thesis, Engineering.
- Förster, A. (2001), 'Analysis of borehole temperature data in the Northeast German Basin: continuous logs versus bottom-hole temperatures', *Petroleum Geoscience* 7, 241–254.

- Förster, A., Förster, H.J., & Krentz, O. (2018), 'Exploration of the enhanced geothermal system (EGS) potential of crystalline rocks for district heating (Elbe Zone, Saxony, Germany)', *International Journal of Earth Sciences* 107, 89–101.
- Forster, C., & Smith, L. (1989), 'The influence of groundwater flow on thermal regimes in mountainous terrain: A model study', *Journal of Geophysical Research: Solid Earth* 94, 9439–9451.
- Fournier, R.O. (1999), 'Hydrothermal processes related to movement of fluid from plastic into brittle rock in the magmatic-epithermal environment', *Economic Geology* 94, 1193–1211.
- Franzson, H., Thordarson, S., Björnsson, G., Gudlaugsson, S.T., Richter, B., Fridleifsson, G.O., & Thorhallsson, S. (2002), Reykjanes high-temperature field, SW-Iceland. Geology and hydrothermal alteration of well RN-10, in 'Workshop on Geothermal Reservoir Engineering', Vol. 27, pp. 233–240.
- Freymark, J., Sippel, J., Scheck-Wenderoth, M., Bär, K., Stiller, M., Fritsche, J.G., & Kracht, M. (2017), 'The deep thermal field of the Upper Rhine Graben', *Tectonophysics* 694, 114–129.
- Fridleifsson, G., Bogason, S., Ingolfsson, H., Vergnes, P., Thorbjörnsson, I., Peter-Borie, M., Kohl, T., Gaucher, E., Edelmann, T., Bertani, R. et al. (2016), Deployment of deep enhanced geothermal systems for sustainable energy business, in 'Proceedings of the Conference: European Geothermal Congress', p. 8.
- Fridleifsson, G.O., & Elders, W.A. (2005), 'The Iceland Deep Drilling Project: a search for deep unconventional geothermal resources', *Geothermics* 34, 269–285.
- Fridriksson, T., Stefánsson, A., Óskarsson, F., Eyjólfsdóttir, E., & Sigurdsson, Ó. (2015), Fluid chemistry scenarios anticipated for IDDP-2 to be drilled in Reykjanes, Iceland, in 'Proceedings World Geothermal Congress', Melbourne, Australia.
- Friðleifsson, G., Albertsson, A., Elders, W., Sigurdsson, Ó., Karlsdóttir, R., & Pálsson, B. (2011), 'The Iceland Deep Drilling Project (IDDP): planning for the second deep well at Reykjanes', *Geotherm. Resour. Counc. Trans* 35, 347–354.
- Friðleifsson, G., Sigurdsson, Ó., Þorbjörnsson, D., Karlsdóttir, R., Gíslason, Þ., Albertsson, A., & Elders, W. (2014), 'Preparation for drilling well IDDP-2 at Reykjanes', *Geothermics* 49, 119–126.
- Friðleifsson, G. et al. (2018), 'The Iceland Deep Drilling Project at Reykjanes: drilling into the root zone of an analog of a black smoker', *J. Volc. Geotherm. Res.* .

- Friðleifsson, G.Ó., & Elders, W.A. (2017), 'Successful drilling for supercritical geothermal resources at Reykjanes in SW Iceland', *Trans Geotherm Resour Council* 41, 1095–106.
- Friðleifsson, G.Ó., Elders, W.A., Zierenberg, R.A., Fowler, A.P., Weisenberger, T.B., Mesfin, K.G., Sigurðsson, Ó., Níelsson, S., Einarsson, G., Óskarsson, F. et al. (2020), 'The Iceland Deep Drilling Project at Reykjanes: Drilling into the root zone of a black smoker analog', *Journal of Volcanology and Geothermal Research* 391, 106435.
- Friðleifsson, G.Ó., Elders, W.A., Zierenberg, R.A., Stefánsson, A., Fowler, A.P., Weisenberger, T.B., Harðarson, B.S., & Mesfin, K.G. (2017), 'The Iceland Deep Drilling Project 4.5 km deep well, IDDP-2, in the seawater-recharged Reykjanes geothermal field in SW Iceland has successfully reached its supercritical target', *Scientific Drilling* 23, 1–12.
- Fuchs, S., & Balling, N. (2016), 'Improving the temperature predictions of subsurface thermal models by using high-quality input data. Part 1: Uncertainty analysis of the thermal-conductivity parameterization', *Geothermics* 64, 42–54.
- García, A., Santoyo, E., Espinosa, G., Hernández, I., & Gutierrez, H. (1998), 'Estimation of temperatures in geothermal wells during circulation and shut-in in the presence of lost circulation', *Transport in Porous Media* 33, 103–127.
- Gaston, D., Newman, C., Hansen, G., & Lebrun-Grandie, D. (2009), 'MOOSE: A parallel computational framework for coupled systems of nonlinear equations', *Nuclear Engineering and Design* 239, 1768–1778.
- Gaston, D., Permann, C., Andrs, D., & Peterson, J. (2013), Massive hybrid parallelism for fully implicit multiphysics, in 'Proceedings of the 2013 International Conference on Mathematics and Computational Methods Applied to Nuclear Science and Engineering-M and C 2013'.
- Genter, A., Evans, K., Cuenot, N., Fritsch, D., & Sanjuan, B. (2010), 'Contribution of the exploration of deep crystalline fractured reservoir of Soultz to the knowledge of enhanced geothermal systems (EGS)', *Comptes Rendus Geoscience* 342, 502–516.
- Gernert, J., Jäger, A., & Span, R. (2014), 'Calculation of phase equilibria for multi-component mixtures using highly accurate Helmholtz energy equations of state', *Fluid Phase Equilibria* 375, 209–218.

- Gholamrezaie, E., Scheck-Wenderoth, M., Sippel, J., & Strecker, M.R. (2018), 'Variability of the geothermal gradient across two differently aged magma-rich continental rifted margins of the Atlantic Ocean: the Southwest African and the Norwegian margins', *Solid Earth* 9, 139–158.
- Gnielinski, V. (2013), 'On heat transfer in tubes', *International Journal of Heat and Mass Transfer* 63, 134–140.
- Golovanova, I., Sal'manova, R.Y., & Tagirova, C.D. (2014), 'Method for deep temperature estimation with regard to the paleoclimate influence on heat flow', *Russian Geology and Geophysics* 55, 1130–1137.
- Goutorbe, B., Lucazeau, F., & Bonneville, A. (2007), 'Comparison of several BHT correction methods: a case study on an Australian data set', *Geophysical Journal International* 170, 913–922.
- Grana, D., & Della Rossa, E. (2010), 'Probabilistic petrophysical-properties estimation integrating statistical rock physics with seismic inversion', *Geophysics* 75, O21–O37.
- Gretener, P.E. (1967), 'On the thermal instability of large diameter wells—an observational report', *Geophysics* 32, 727–738.
- Großwig, S., Hurtig, E., & Kühn, K. (1996), 'Fibre optic temperature sensing: A new tool for temperature measurements in boreholes', *Geophysics* 61, 1065–1067.
- Guillou-Frottier, L., Carré, C., Bourguin, B., Bouchot, V., & Genter, A. (2013), 'Structure of hydrothermal convection in the Upper Rhine Graben as inferred from corrected temperature data and basin-scale numerical models', *Journal of Volcanology and Geothermal Research* 256, 29–49.
- Gunnarsson, G., Arnaldsson, A., & Oddsdóttir, A.L. (2011), 'Model simulations of the Hengill area, Southwestern Iceland', *Transport in porous media* 90, 3–22.
- Guo, R., Dosso, S.E., Liu, J., Dettmer, J., & Tong, X. (2011), 'Non-linearity in Bayesian 1-D magnetotelluric inversion', *Geophysical Journal International* 185, 663–675.
- Haenel, R., Stegena, L., & Rybach, L. (2012), *Handbook of terrestrial heat-flow density determination: with guidelines and recommendations of the International Heat Flow Commission*, Vol. 4, Springer Science & Business Media.

- Hansen, T.M., & Cordua, K.S. (2017), 'Efficient Monte Carlo sampling of inverse problems using a neural network-based forward—Applied to GPR crosshole travel-time inversion', *Geophysical Journal International* 211, 1524–1533.
- Hardardóttir, V., Hannington, M., Hedenquist, J., Kjarsgaard, I., & Hoal, K. (2010), 'Cu-rich scales in the Reykjanes geothermal system, Iceland', *Economic Geology* 105, 1143–1155.
- Hartmann, A., & Rath, V. (2005), 'Uncertainties and shortcomings of ground surface temperature histories derived from inversion of temperature logs', *Journal of Geophysics and Engineering* 2, 299–311.
- Hasan, A., & Kabir, C. (1994), 'Static reservoir temperature determination from transient data after mud circulation', *SPE Drilling and Completion (Society of Petroleum Engineers);(United States)* 9.
- Hasan, A., Kabir, C. et al. (1994), 'Determination of static reservoir temperature from transient data following mud circulation', *SPE Drilling & Completion* 9, 17–24.
- Hellstrom, G. (1992), 'Ground heat storage: Thermal analyses of duct storage systems. I. Theory.'
- Hillis, R., Hand, M., Mildren, S., Reid, P., Reynolds, S., & Nelson, E. (2004), 'Hot dry rock geothermal exploration in Australia', *ASEG Extended Abstracts* 2004, 1–4.
- Hokstad, K., & Tanavasuu-Milkeviciene, K. (2017), 'Temperature prediction by multigeophysical inversion: application to the IDDP-2 well at Reykjanes, Iceland', *Geotherm Resource Council* 41, 1141–52.
- Hokstad, K., Tašárová, Z.A., Clark, S.A., Kyrkjebø, R., Duffaut, K., Fichler, C., & Wiik, T. (2017), 'Radiogenic heat production in the crust from inversion of gravity and magnetic data', *Norwegian Journal of Geology* 97, 241–254.
- Hong, T., & Sen, M.K. (2009), 'A new MCMC algorithm for seismic waveform inversion and corresponding uncertainty analysis', *Geophysical Journal International* 177, 14–32.
- Horner, D.R. (1951), Pressure build-up in wells, in '3rd world petroleum congress', OnePetro.
- Hossain, M.E. (2015), 'Drilling Costs Estimation for Hydrocarbon Wells', *Journal of Sustainable Energy Engineering* 3, 3–32.

- Ikeuchi, K., Doi, N., Sakagawa, Y., Kamenosono, H., & Uchida, T. (1998), 'High-temperature measurements in well WD-1a and the thermal structure of the Kakkonda geothermal system, Japan', *Geothermics* 27, 591–607.
- Jaeger, J.C., & Carslaw, H.S. (1959), *Conduction of heat in solids*, Clarendon P.
- Jha, S.K., & Puppala, H. (2017), 'Assessment of subsurface temperature distribution from the gauged wells of Puga Valley, Ladakh', *Geothermal Energy* 5, 1–15.
- Jhong, B.C., Wang, J.H., & Lin, G.F. (2017), 'An integrated two-stage support vector machine approach to forecast inundation maps during typhoons', *Journal of Hydrology* 547, 236–252.
- Johnson, J.W., Oelkers, E.H., & Helgeson, H.C. (1992), 'SUPCRT92: A software package for calculating the standard molal thermodynamic properties of minerals, gases, aqueous species, and reactions from 1 to 5000 bar and 0 to 1000 C', *Computers & Geosciences* 18, 899–947.
- Jónsson, S., Sigurgeirsson, M., Sigurðsson, Ó., & Ingólfsson, H. (2010), 'Reykjanes–Holla RN-15, 3. phase: Drilling of the production part from 804 m to 2507 m', *ÍSOR Report* 50, 69.
- Kabir, C., Izgec, B., Hasan, A., & Wang, X. (2012), 'Computing flow profiles and total flow rate with temperature surveys in gas wells', *Journal of Natural Gas Science and Engineering* 4, 1–7.
- Klepikova, M.V., Le Borgne, T., Bour, O., & Davy, P. (2011), 'A methodology for using borehole temperature-depth profiles under ambient, single and cross-borehole pumping conditions to estimate fracture hydraulic properties', *Journal of Hydrology* 407, 145–152.
- Klepikova, M.V., Le Borgne, T., Bour, O., Gallagher, K., Hochreutener, R., & Lavenant, N. (2014), 'Passive temperature tomography experiments to characterize transmissivity and connectivity of preferential flow paths in fractured media', *Journal of Hydrology* 512, 549–562.
- Klepikova, M.V., Roques, C., Loew, S., & Selker, J. (2018), 'Improved characterization of groundwater flow in heterogeneous aquifers using granular polyacrylamide (PAM) gel as temporary grout', *Water Resources Research* 54, 1410–1419.
- Kohl, T. (1998), 'Palaeoclimatic temperature signals—can they be washed out?', *Tectonophysics* 291, 225–234.

- Kohl, T., Bächler, D., & Rybach, L. (2000), Steps towards a comprehensive thermo-hydraulic analysis of the HDR test site Soultz-sous-Forêts, in 'Proceedings World Geothermal Congress', Kyushu-Tohoku, Japan, pp. 2671–2676.
- Kohl, T., Brenni, R., & Eugster, W. (2002), 'System performance of a deep borehole heat exchanger', *Geothermics* 31, 687–708.
- Konrad, F., Savvatis, A., Wellmann, F., & Zosseder, K. (2019), 'Hydraulic behavior of fault zones in pump tests of geothermal wells: a parametric analysis using numerical simulations for the Upper Jurassic aquifer of the North Alpine Foreland Basin', *Geothermal Energy* 7, 1–28.
- Korenaga, J. (2011), 'Clairvoyant geoneutrinos', *Nature Geoscience* 4, 581–582.
- Korzani, M.G., Nitschke, F., Held, S., & Kohl, T. (2019), 'The development of a fully coupled wellbore-reservoir simulator for geothermal application', *GRC Transactions* 43.
- Kranz, K. (2006), 'Geothermal energy in Iceland', *Technische Universität Bergakademie Freiberg* pp. 1–15.
- Kruszewski, M., & Wittig, V. (2018), 'Review of failure modes in supercritical geothermal drilling projects', *Geothermal Energy* 6, 1–29.
- Kubik, M. (2006), The future of geothermal energy, Technical report, Massachusetts Inst. of Technology (MIT), Cambridge, MA (United States).
- Kutasov, I. (1987), 'Dimensionless temperature, cumulative heat flow and heat flow rate for a well with a constant bore-face temperature', *Geothermics* 16, 467–472.
- Kutasov, I. (2003), 'Dimensionless temperature at the wall of an infinite long cylindrical source with a constant heat flow rate', *Geothermics* 32, 63–68.
- Kutasov, I., & Devyatkin, V. (1973), 'Effect of Free Heat Convection and Casing on the Temperature Field in Boreholes', *Heat Flows from the Crust and Upper Mantle of the Earth* pp. 99–106.
- Kutasov, I., & Eppelbaum, L. (2005), 'Determination of formation temperature from bottom-hole temperature logs—a generalized Horner method', *Journal of Geophysics and Engineering* 2, 90–96.
- Kutasov, I., & Eppelbaum, L. (2010), 'A new method for determining the formation temperature from bottom-hole temperature logs', *Journal of Petroleum and Gas Engineering* 1, 1–8.

- Kutasov, I.M., & Eppelbaum, L.V. (2018), 'Utilization of the Horner plot for determining the temperature of frozen formations—a novel approach', *Geothermics* 71, 259–263.
- Kutun, K., Tureyen, O., & Satman, A. (2015), Analysis of wellhead production temperature derivatives, *in* 'Proceedings, 40th Workshop'.
- Kutun, K., Tureyen, O.I., & Satman, A. (2014), Temperature behavior of geothermal wells during production, injection and shut-in operations, *in* 'proceedings, 39th workshop on geothermal reservoir engineering, Stanford University, Stanford, California'.
- Laarossi, I., Quintela-Incera, M.Á., & López-Higuera, J.M. (2019), 'Comparative experimental study of a high-temperature raman-based distributed optical fiber sensor with different special fibers', *Sensors* 19, 574.
- Laloy, E., Rogiers, B., Vrugt, J.A., Mallants, D., & Jacques, D. (2013), 'Efficient posterior exploration of a high-dimensional groundwater model from two-stage Markov chain Monte Carlo simulation and polynomial chaos expansion', *Water Resources Research* 49, 2664–2682.
- Leblanc, Y., Pascoe, L., & Jones, F. (1981), 'The temperature stabilization of a borehole', *Geophysics* 46, 1301–1303.
- Lee, K. (1996), Classification of geothermal resources-an engineering approach, Technical report, Geothermal Institute, The University of Auckland, Auckland, NZ.
- Lee, T.C. (1982), 'Estimation of formation temperature and thermal property from dissipation of heat generated by drilling', *Geophysics* 47, 1577–1584.
- Lee, T.J. (2019), 'High Pressure-High Temperature Well Logging and Measurements as an Emerging Technology for Geothermal Development', *Journal of the Geothermal Research Society of Japan* 41, 45–51.
- Lipsey, L., Pluymaekers, M., Goldberg, T., van Oversteeg, K., Ghazaryan, L., Cloetingh, S., & van Wees, J.D. (2016), 'Numerical modelling of thermal convection in the Luttelgeest carbonate platform, the Netherlands', *Geothermics* 64, 135–151.
- Liu, H., Giroux, B., Harris, L.B., Quenette, S.M., & Mansour, J. (2018), 'Numerical analysis of the role of radiogenic basement on temperature distribution in the St. Lawrence Lowlands, Québec', *Geothermal Energy* 6, 1–26.

- Liu, J., Li, B., Tian, W., & Wu, X. (2018), 'Investigating and predicting permeability variation in thermally cracked dry rocks', *International Journal of Rock Mechanics and Mining Sciences* 103, 77–88.
- Looney, B. (2020), 'Statistical Review of World Energy, 2020', *Bp* 69, 66.
- Lu, S.M. (2018), 'A global review of enhanced geothermal system (EGS)', *Renewable and Sustainable Energy Reviews* 81, 2902–2921.
- Luheshi, M. (1983), 'Estimation of formation temperature from borehole measurements', *Geophysical Journal International* 74, 747–776.
- Lund, J.W., Bjelm, L., Bloomquist, G., & Mortensen, A.K. (2008), 'Characteristics, development and utilization of geothermal resources-a Nordic perspective', *Episodes* 31, 140–147.
- Magnenet, V., Fond, C., Genter, A., & Schmittbuhl, J. (2014), 'Two-dimensional THM modelling of the large scale natural hydrothermal circulation at Soultz-sous-Forêts', *Geothermal Energy* 2, 1–21.
- Magnusdottir, L., & Finsterle, S. (2015), 'An iTOUGH2 equation-of-state module for modeling supercritical conditions in geothermal reservoirs', *Geothermics* 57, 8–17.
- Makowski, D., Ben-Shachar, M.S., Chen, S., & Lüdecke, D. (2019), 'Indices of effect existence and significance in the Bayesian framework', *Frontiers in psychology* 10, 2767.
- Mandelli, D., Alfonsi, A., Smith, C., & Rabiti, C. (2015), 'Generation and Use of Reduced Order Models for Safety Applications Using RAVEN', *Transactions* 113, 779–782.
- Mareschal, J.C., & Jaupart, C. (2013), 'Radiogenic heat production, thermal regime and evolution of continental crust', *Tectonophysics* 609, 524–534.
- Maryadi, M., & Mizunaga, H. (2021), 'Subsurface temperature estimation in a geothermal field based on audio-frequency magnetotelluric data', *Exploration Geophysics* pp. 1–14.
- Mattern, E., Matas, J., Ricard, Y., & Bass, J. (2005), 'Lower mantle composition and temperature from mineral physics and thermodynamic modelling', *Geophysical Journal International* 160, 973–990.
- McLatchie, A., Hemstock, R., & Young, J. (1958), 'The effective compressibility of reservoir rock and its effects on permeability', *Journal of Petroleum Technology* 10, 49–51.

- Meixner, A., Kirkby, A., & Horspool, N. (2014), 'Using constrained gravity inversions to identify high-heat-producing granites beneath thick sedimentary cover in the Cooper Basin region of central Australia', *Geothermics* 51, 483–495.
- Meixner, T., & Holgate, F. (2009), 'In search of hot buried granites: a 3D map of sub-sediment Granitic Bodies in the Cooper Basin Region of Australia, Generated from Inversions of Gravity Data.', *ASEG Extended Abstracts* 2009, 1–11.
- Meyer, T. (2012), 'Root Mean Square Error Compared to, and Contrasted with, Standard Deviation.', *Surveying & Land Information Science* 72.
- Meyzonnat, G., Barbecot, F., Corcho-Alvarado, J.A., Tognelli, A., Zeyen, H., Mattei, A., & McCormack, R. (2018), 'High-resolution wellbore temperature logging combined with a borehole-scale heat budget: conceptual and analytical approaches to characterize hydraulically active fractures and groundwater origin', *Geofluids* 2018.
- Middleton, M. (1979), 'A model for bottom-hole temperature stabilization', *Geophysics* 44, 1458–1462.
- Midttoemme, K. (1997), 'Thermal conductivity of sedimentary rocks-selected methodological, mineralogical and textural studies'.
- Mirghani, B.Y., Zechman, E.M., Ranjithan, R.S., & Mahinthakumar, G. (2012), 'Enhanced simulation-optimization approach using surrogate modeling for solving inverse problems', *Environmental Forensics* 13, 348–363.
- Mo, S., Shi, X., Lu, D., Ye, M., & Wu, J. (2019), 'An adaptive Kriging surrogate method for efficient uncertainty quantification with an application to geological carbon sequestration modeling', *Computers & Geosciences* 125, 69–77.
- Molz, F., Boman, G., Young, S., & Waldrop, W. (1994), 'Borehole flowmeters: Field application and data analysis', *Journal of Hydrology* 163, 347–371.
- Mooney, W.D. (2003), Continental Crust, in R. A. Meyers, ed., 'Encyclopedia of Physical Science and Technology (Third Edition)', third edition edn, Academic Press, New York, pp. 635–647.
- Murthy, V.R. (2007), *Radioactive Isotopes, Their Decay in Mantle and Core*, Springer Netherlands, Dordrecht, pp. 854–856.
- Nian, Y.L., & Cheng, W.L. (2018), 'Insights into geothermal utilization of abandoned oil and gas wells', *Renewable and Sustainable Energy Reviews* 87, 44–60.

- Nian, Y.L., Cheng, W.L., Han, B.B., Li, Y.Q., & Yu, W.J. (2015), 'A novel method for predicting gas/oil flow rate from temperature log data', *Journal of Petroleum Science and Engineering* 133, 801–809.
- Niederer, J., Wellmann, J.F., & Börsing, N. (2019), 'Analyzing the influence of correlation length in permeability on convective systems in heterogeneous aquifers using entropy production', *Geothermal Energy* 7, 1–27.
- Nitschke, F., Gholami Korzani, M., Held, S., & Kohl, T. (2020), A Fully-Coupled Implicit Transient Two-Phase Wellbore Simulator, in 'World Geothermal Congress 2020'.
- Norden, B., Förster, A., Förster, H.J., & Fuchs, S. (2020), 'Temperature and pressure corrections applied to rock thermal conductivity: impact on subsurface temperature prognosis and heat-flow determination in geothermal exploration', *Geothermal Energy* 8, 1–19.
- Norton, D., & Knight, J. (1977), 'Transport phenomena in hydrothermal systems: cooling plutons', *Am. J. Sci.:(United States)* 277.
- Nowak, T. (1953), 'The estimation of water injection profiles from temperature surveys', *Journal of Petroleum Technology* 5, 203–212.
- Nusiaputra, Y.Y. (2017), Coupled Hydraulic, Thermal and Chemical Simulations for Geothermal Installations, PhD thesis, Karlsruher Institut für Technologie (KIT).
- Okamoto, K., Asanuma, H., Ishibashi, T., Yamaya, Y., Saishu, H., Yanagisawa, N., Mogi, T., Tsuchiya, N., Okamoto, A., Naganawa, S. et al. (2019), 'Geological and engineering features of developing ultra-high-temperature geothermal systems in the world', *Geothermics* 82, 267–281.
- Oladyshkin, S., Class, H., Helmig, R., & Nowak, W. (2011), 'An integrative approach to robust design and probabilistic risk assessment for CO₂ storage in geological formations', *Computational Geosciences* 15, 565–577.
- O'Sullivan, M., & O'Sullivan, J. (2016), Reservoir modeling and simulation for geothermal resource characterization and evaluation, in 'Geothermal power generation', Elsevier, pp. 165–199.
- Pan, I., Babaei, M., Korre, A., & Durucan, S. (2014), 'Artificial Neural Network based surrogate modelling for multi-objective optimisation of geological CO₂ storage operations', *Energy Procedia* 63, 3483–3491.

- Pan, L., & Oldenburg, C.M. (2014), 'T2Well—an integrated wellbore–reservoir simulator', *Computers & Geosciences* 65, 46–55.
- Pasquale, V., Chiozzi, P., & Verdoya, M. (2013), 'Evidence for thermal convection in the deep carbonate aquifer of the eastern sector of the Po Plain, Italy', *Tectonophysics* 594, 1–12.
- Patterson, J.R., Cardiff, M., Coleman, T., Wang, H., Feigl, K.L., Akerley, J., & Spielman, P. (2017), 'Geothermal reservoir characterization using distributed temperature sensing at Brady Geothermal Field, Nevada', *The Leading Edge* 36, 1024a1–1024a7.
- Pedregosa, F., Varoquaux, G., Gramfort, A., Michel, V., Thirion, B., Grisel, O., Blondel, M., Prettenhofer, P., Weiss, R., Dubourg, V. et al. (2011), 'Scikit-learn: Machine learning in Python', *the Journal of machine Learning research* 12, 2825–2830.
- Pehme, P., Parker, B., Cherry, J., & Greenhouse, J. (2010), 'Improved resolution of ambient flow through fractured rock with temperature logs', *Groundwater* 48, 191–205.
- Peter-Borie, M., Loschetter, A., Merciu, I., Kampfer, G., & Sigurdsson, O. (2018), 'Borehole damaging under thermo-mechanical loading in the RN-15/IDDP-2 deep well: towards validation of numerical modeling using logging images', *Geothermal Energy* 6, 1–33.
- Pfister, M., & Rybach, L. (1995), 'High-resolution digital temperature logging in areas with significant convective heat transfer', *Geothermics* 24, 95–100.
- Pontes, F.J., Amorim, G., Balestrassi, P.P., Paiva, A., & Ferreira, J.R. (2016), 'Design of experiments and focused grid search for neural network parameter optimization', *Neurocomputing* 186, 22–34.
- Potter, J.M. (1978), Experimental permeability studies at elevated temperature and pressure of granitic rocks, Technical report, Los Alamos Scientific Lab., N. Mex.(USA).
- Prensky, S. et al. (1992), 'Temperature measurements in boreholes-An overview of engineering and scientific applications', *The Log Analyst* 33, 313–333.
- Przybycin, A.M., Scheck-Wenderoth, M., & Schneider, M. (2015), 'The 3D conductive thermal field of the North Alpine Foreland Basin: influence of the deep structure and the adjacent European Alps', *Geothermal energy* 3, 1–29.

- Raje, D., & Krishnan, R. (2012), 'Bayesian parameter uncertainty modeling in a macroscale hydrologic model and its impact on Indian river basin hydrology under climate change', *Water Resources Research* 48.
- Ramey, H.J., & Sanyal, S. (1981), *Reservoir Engineering Assessment of Geothermal Systems: HJ Ramey, Jr., Editor; Contributors, SK Sanyal...[et Al.]*, Department of Petroleum Engineering, School of Earth Sciences, Stanford
- Ramey Jr, H.J. et al. (1962), 'Wellbore heat transmission', *Journal of petroleum Technology* 14, 427–435.
- Raymond, J., Therrien, R., & Gosselin, L. (2011), 'Borehole temperature evolution during thermal response tests', *Geothermics* 40, 69–78.
- Read, T., Bense, V., Hochreutener, R., Bour, O., Borgne, T.L., Lavenant, N., & Selker, J. (2015), 'Thermal-plume fibre optic tracking (T-POT) test for flow velocity measurement in groundwater boreholes', *Geoscientific Instrumentation, Methods and Data Systems* 4, 197–202.
- Read, T., Bour, O., Bense, V., Le Borgne, T., Goderniaux, P., Klepikova, M., Hochreutener, R., Lavenant, N., & Boschero, V. (2013), 'Characterizing groundwater flow and heat transport in fractured rock using fiber-optic distributed temperature sensing', *Geophysical Research Letters* 40, 2055–2059.
- Reges, J.E., Salazar, A.O., Maitelli, C.W., Carvalho, L.G., & Britto, U.J. (2016), 'Flow rates measurement and uncertainty analysis in multiple-zone water-injection wells from fluid temperature profiles', *Sensors* 16, 1077.
- Reinsch, T., Dobson, P., Asanuma, H., Huenges, E., Poletto, F., & Sanjuan, B. (2017), 'Utilizing supercritical geothermal systems: a review of past ventures and ongoing research activities', *Geothermal Energy* 5, 1–25.
- Reinsch, T., Hennings, J., & Ásmundsson, R. (2013), 'Thermal, mechanical and chemical influences on the performance of optical fibres for distributed temperature sensing in a hot geothermal well', *Environmental earth sciences* 70, 3465–3480.
- Roux, B., Sanyal, S.K., & Brown, S.L. (1980), An improved approach to estimating true reservoir temperature from transient temperature data, in 'SPE California Regional meeting', OnePetro.
- Ruether, J. (2011), The validation of the lmc device: Analysis of icelandic basaltic rocks, Master's thesis, University of Iceland.

- Rühaak, W., Bär, K., & Sass, I. (2014), 'Combining numerical modeling with geostatistical interpolation for an improved reservoir exploration', *Energy Procedia* 59, 315–322.
- Runarsson, T.P. (2004), Constrained evolutionary optimization by approximate ranking and surrogate models, *in* 'International conference on parallel problem solving from nature', Springer, pp. 401–410.
- Russell, S., & Norvig, P. (2002), 'Artificial intelligence: a modern approach'.
- Sambridge, M., Gallagher, K., Jackson, A., & Rickwood, P. (2006), 'Trans-dimensional inverse problems, model comparison and the evidence', *Geophysical Journal International* 167, 528–542.
- Sass, I., & Lehr, C. (2011), Improvements on the thermal response test evaluation applying the cylinder source theory, *in* 'Proceedings of the 36th Workshop on Geothermal Reservoir Engineering'.
- Schilling, O., Sheldon, H.A., Reid, L.B., & Corbel, S. (2013), 'Hydrothermal models of the Perth metropolitan area, Western Australia: implications for geothermal energy', *Hydrogeology Journal* 21, 605–621.
- Schintgen, T., Förster, A., Förster, H.J., & Norden, B. (2015), 'Surface heat flow and lithosphere thermal structure of the Rhenohercynian Zone in the greater Luxembourg region', *Geothermics* 56, 93–109.
- Schloessin, H., & Dvorak, Z. (1972), 'Anisotropic lattice thermal conductivity in enstatite as a function of pressure and temperature', *Geophysical Journal International* 27, 499–516.
- Schön, J.H. (2015), *Physical properties of rocks: Fundamentals and principles of petrophysics*, Elsevier.
- Schulte, D.O., Arnold, D., Geiger, S., Demyanov, V., & Sass, I. (2020), 'Multi-objective optimization under uncertainty of geothermal reservoirs using experimental design-based proxy models', *Geothermics* 86, 101792.
- Schulz, R., Jung, R., Pester, S., & Schellschmidt, R. (2007), Quantification of exploration risks for hydrogeothermal wells, *in* 'Proceedings European Geothermal Congress'.
- Scott, S., Driesner, T., & Weis, P. (2016), 'The thermal structure and temporal evolution of high-enthalpy geothermal systems', *Geothermics* 62, 33–47.

- Sekine, K., Bignall, G., & Tsuchiya, N. (2004), 'Application of synthetic fluid inclusions to simultaneous temperature–pressure logging in high-temperature (sub-to supercritical) geothermal systems', *Geothermics* 33, 775–793.
- Sharma, J., Adnyana, G., Barnes, D., Mims, D., & Behrens, R. (2021), 'Temperature logging guidelines and factors that affect measurement accuracy in steamfloods', *Journal of Petroleum Science and Engineering* 196, 107727.
- Shen, P., & Beck, A. (1986), 'Stabilization of bottom hole temperature with finite circulation time and fluid flow', *Geophysical Journal International* 86, 63–90.
- Shmonov, V.M., Vitovtova, V.M., & Zarubina, I.V. (1994), Permeability of rocks at elevated temperatures and pressures, in 'Fluids in the crust', Springer, pp. 285–313.
- Silva, W.L., Lima, V.S., Fonseca, D.A., Salazar, A.O., Maitelli, C.W., Echaiz E, G.A. et al. (2019), 'Study of Flow Rate Measurements Derived from Temperature Profiles of an Emulated Well by a Laboratory Prototype', *Sensors* 19, 1498.
- Slagstad, T., Midttømme, K., Ramstad, R.K., & Slagstad, D. (2008), 'Factors influencing shallow (< 1000 m depth) temperatures and their significance for extraction of ground-source heat', *Geology for society. Spec. Publ* 11, 99–109.
- Smith, T.J., & Marshall, L.A. (2008), 'Bayesian methods in hydrologic modeling: A study of recent advancements in Markov chain Monte Carlo techniques', *Water Resources Research* 44.
- Spikes, K., Mukerji, T., Dvorkin, J., & Mavko, G. (2007), 'Probabilistic seismic inversion based on rock-physics models', *Geophysics* 72, R87–R97.
- Stefánsson, A., Driesner, T., & Bénézech, P. (2018), *Thermodynamics of geothermal fluids*, Vol. 76, Walter de Gruyter GmbH & Co KG.
- Steingrímsson, B. (2013), 'Geothermal well logging: Temperature and pressure logs', *Tutorial-Geothermal Training Programme* .
- Stober, I., & Bucher, K. (2013), 'Geothermal energy', *Germany: Springer-Verlag Berlin Heidelberg*. doi 10, 978–3.
- Štulc, P. (1995), 'Return to thermal equilibrium of an intermittently drilled hole: theory and experiment', *Tectonophysics* 241, 35–45.
- Sudakov, O., Koroteev, D., Belozarov, B., & Burnaev, E. (2019), Artificial neural network surrogate modeling of oil reservoir: a case study, in 'International Symposium on Neural Networks', Springer, pp. 232–241.

- Sun, Y., Hou, Z., Huang, M., Tian, F., & Ruby Leung, L. (2013), 'Inverse modeling of hydrologic parameters using surface flux and runoff observations in the Community Land Model', *Hydrology and Earth System Sciences* 17, 4995–5011.
- Talalay, P., Li, Y., Augustin, L., Clow, G.D., Hong, J., Lefebvre, E., Markov, A., Motoyama, H., & Ritz, C. (2020), 'Geothermal heat flux from measured temperature profiles in deep ice boreholes in Antarctica', *The Cryosphere* 14, 4021–4037.
- Tirone, M. (2015), 'On the use of thermal equations of state and the extrapolation at high temperature and pressure for geophysical and petrological applications', *Geophysical Journal International* 202, 1483–1494.
- Tomac, I., & Sauter, M. (2018), 'A review on challenges in the assessment of geomechanical rock performance for deep geothermal reservoir development', *Renewable and Sustainable Energy Reviews* 82, 3972–3980.
- Tulinius, H. (2017), 'Estimation of Formation Temperature below 4000 m Depth in Well IDDP-2 Using Horner Plots', *Prepared for DEEPEGS, Short report ÍSOR-17069*.
- Turcotte, D.L., & Schubert, G. (2002), *Geodynamics*, Cambridge university press.
- Vaclav, S. (2017), 'Energy transitions: Global and national perspectives', *BP Statistical Review of World Energy*.
- van der Veen, C.J., Leftwich, T., Von Frese, R., Csatho, B.M., & Li, J. (2007), 'Subglacial topography and geothermal heat flux: Potential interactions with drainage of the Greenland ice sheet', *Geophysical research letters* 34.
- Vedum, J., Røed, M.H., Kolberg, S., Hjelstuen, M., Liverud, A.E., & Stamnes, Ø.N. (2017), Development of a Novel Logging Tool for 450 °C Geothermal Wells, in 'Additional Conferences (Device Packaging, HiTEC, HiTEN, & CICMT)', Vol. 2017, International Microelectronics Assembly and Packaging Society, pp. 000011–000019.
- Verma, S.P., Andaverde, J., & Santoyo, E. (2006a), 'Application of the error propagation theory in estimates of static formation temperatures in geothermal and petroleum boreholes', *Energy Conversion and Management* 47, 3659–3671.
- Verma, S.P., Andaverde, J., & Santoyo, E. (2006b), 'Statistical evaluation of methods for the calculation of static formation temperatures in geothermal and oil wells using an extension of the error propagation theory', *Journal of Geochemical Exploration* 89, 398–404.

- Vidal, J., Hehn, R., Glaas, C., & Genter, A. (2019), 'How can temperature logs help identify permeable fractures and define a conceptual model of fluid circulation? An example from deep geothermal wells in the Upper Rhine Graben', *Geofluids* 2019.
- Vrugt, J.A. (2016), 'Markov chain Monte Carlo simulation using the DREAM software package: Theory, concepts, and MATLAB implementation', *Environmental Modelling & Software* 75, 273–316.
- Wagner, R., & Clauser, C. (2005), 'Evaluating thermal response tests using parameter estimation for thermal conductivity and thermal capacity', *Journal of geophysics and engineering* 2, 349–356.
- Wagner, W., & Pruß, A. (2002), 'The IAPWS formulation 1995 for the thermodynamic properties of ordinary water substance for general and scientific use', *Journal of physical and chemical reference data* 31, 387–535.
- Wang, J., Nitschke, F., Gaucher, E., & Kohl, T. (2021), 'Uncertainty analysis of numerical inversions of temperature logs from boreholes under injection conditions', *Journal of Geophysics and Engineering* 18, 1022–1034.
- Wang, J., Nitschke, F., Korzani, M.G., & Kohl, T. (2019), 'Temperature log simulations in high-enthalpy boreholes', *Geothermal Energy* 7, 1–21.
- Wang, X., Bussear, T.R., Hasan, A.R. et al. (2010), Technique to improve flow profiling using distributed-temperature sensors, in 'SPE Latin American and Caribbean Petroleum Engineering Conference', Society of Petroleum Engineers.
- Watanabe, N., Egawa, M., Sakaguchi, K., Ishibashi, T., & Tsuchiya, N. (2017), 'Hydraulic fracturing and permeability enhancement in granite from subcritical/brittle to supercritical/ductile conditions', *Geophysical Research Letters* 44, 5468–5475.
- Watanabe, N., Numakura, T., Sakaguchi, K., Saishu, H., Okamoto, A., Ingebritsen, S.E., & Tsuchiya, N. (2017), 'Potentially exploitable supercritical geothermal resources in the ductile crust', *Nature Geoscience* 10, 140–144.
- Weisenberger, T., Harðarson, B., Kästner, F., Gunnarsdóttir, S., Tulinius, H., Guðmundsdóttir, V., Einarsson, G., Pétursson, F., Vilhjálmsson, S., Stefánsson, H. et al. (2017), 'Well Report–RN-15/IDDP-2', *Drilling in Reykjanes–Phase 4*.
- White, D.E. (1957), 'Thermal waters of volcanic origin', *Geological Society of America Bulletin* 68, 1637–1658.

- Witte, H. (2001), 'Geothermal response test with heat extraction and heat injection: examples of application in research and design of geothermal heat exchangers', *Worskhop Europeen sur Test de Reponse Geothermique, Lausanne* .
- Witterholt, E., Tixier, M. et al. (1972), Temperature logging in injection wells, in 'Fall Meeting of the Society of Petroleum Engineers of AIME', Society of Petroleum Engineers.
- Wong-Loya, J., Andaverde, J., & Santoyo, E. (2012), 'A new practical method for the determination of static formation temperatures in geothermal and petroleum wells using a numerical method based on rational polynomial functions', *Journal of Geophysics and Engineering* 9, 711–728.
- Wu, Y.S., & Pruess, K. (1990), 'An analytical solution for wellbore heat transmission in layered formations (includes associated papers 23410 and 23411)', *SPE Reservoir Engineering* 5, 531–538.
- Xu, C., Yan, X., Kang, Y., You, L., You, Z., Zhang, H., & Zhang, J. (2019), 'Friction coefficient: A significant parameter for lost circulation control and material selection in naturally fractured reservoir', *Energy* 174, 1012–1025.
- Xu, T., Valocchi, A.J., Ye, M., & Liang, F. (2017), 'Quantifying model structural error: Efficient Bayesian calibration of a regional groundwater flow model using surrogates and a data-driven error model', *Water Resources Research* 53, 4084–4105.
- Yang, M., Li, X., Deng, J., Meng, Y., & Li, G. (2015), 'Prediction of wellbore and formation temperatures during circulation and shut-in stages under kick conditions', *Energy* 91, 1018–1029.
- Yang, M., Meng, Y., Li, G., Li, Y., Chen, Y., Zhao, X., & Li, H. (2013), 'Estimation of wellbore and formation temperatures during the drilling process under lost circulation conditions', *Mathematical Problems in Engineering* 2013.
- Ystroem, L.H., Nitschke, F., Held, S., & Kohl, T. (2020), 'A multicomponent geothermometer for high-temperature basalt settings', *Geothermal Energy* 8, 1–21.
- Zhang, C., Hu, S., Zhang, S., Li, S., Zhang, L., Kong, Y., Zuo, Y., Song, R., Jiang, G., & Wang, Z. (2020), 'Radiogenic heat production variations in the Gonghe basin, northeastern Tibetan Plateau: Implications for the origin of high-temperature geothermal resources', *Renewable Energy* 148, 284–297.

- Zhang, J., Zheng, Q., Chen, D., Wu, L., & Zeng, L. (2020), 'Surrogate-based Bayesian inverse modeling of the hydrological system: An adaptive approach considering surrogate approximation error', *Water Resources Research* 56, e2019WR025721.
- Zhou, F. (2013), Research on heat transfer in geothermal wellbore and surroundings, PhD thesis, Technische Universität Berlin.
- Zhou, L., Zhang, Y., Hu, Z., Yu, Z., Luo, Y., Lei, Y., Lei, H., Lei, Z., & Ma, Y. (2019), 'Analysis of influencing factors of the production performance of an enhanced geothermal system (EGS) with numerical simulation and artificial neural network (ANN)', *Energy and Buildings* 200, 31–46.
- Zierenberg, R.A., Fowler, A.P., Friðleifsson, G.Ó., Elders, W.A., & Weisenberger, T.B. (2017), 'Preliminary description of rocks and alteration in IDDP-2 drill core samples recovered from the Reykjanes geothermal system, Iceland'.